A mamma e papà...

Contents

Abstract

Natural rivers are self-formed features whose shapes are the result of interaction between erosion, deposition and transport of sediments. The study of their morphodynamics and the characterization of related sedimentary processes are of great interest not only to environmental engineers but also to hydrologist and geologist, contributing to the interpretation of stratigraphic records. In particular, this thesis deals with the morphodynamics and the long term behaviour of meandering rivers, a very common pattern in nature. This class of dynamical systems, which occurs at the spatial scale of the channel width, are driven by the coexistence of various intrinsically nonlinear mechanisms which determine the possible occurrence of two different morphodynamic regimes: the sub-resonant and the super-resonant regime. On the short term time scale, the formation of meandering patterns can be suitably explained as an instability process, driven by bank erosion (bend instability). The planar development of the river is described by a non-linear integro-differential bend evolution equation, complemented with a suitable model for flow and bed topography in sinuous channels with cohesionless bed. On the long-term timescale, a further highly non-linear process must be accounted for, namely channel shortening via cutoff processes. Depending on the description adopted for the flow field, various mathematical models allowing the description of the temporal evolution of the channel axis can be developed. Here, we develop a simulation model for river meandering employing two physics-based linear models characterized by a different degree of approximation. The fully nonlinear computational approach permits exploration of the long term dynamics of meandering rivers. Investigating the full range of morphodynamic conditions, we objectively compare the morphologic characteristics exhibited by synthetically generated and

observed planimetric patterns. The analysis is carried out examining, through principal component analysis, a suitable set of morphological variables. We show that, even in the presence of the strong filtering action exerted by cutoff processes, a closer, although not yet complete, similarity with natural meandering planforms can be achieved only by adopting a flow field model which accounts for the full range of morphodynamic regimes. We also introduce a new morphodynamic length scale $\mathcal{L}_m$, associated with spatially oscillating disturbances. Once normalized with this length scale, the relevant morphologic features of the simulated long-term patterns (e.g., the pdf of local curvature and the geometric characteristics of oxbow lakes) tend to collapse on two distinct behaviours, depending on the dominant morphologic regime. Finally, the signatures of possibly chaotic dynamics or self-organized criticality triggered by repeated cutoff events are investigated. To these aims, some robust nonlinearity tests are applied to both the spatial series of local curvatures and the time series of long term tortuosity. Temporal distribution of cutoff inter-arrivals are also investigated. The results are coherent and show that no evidence of chaotic determinism or self-organized criticality are detectable in meandering dynamics.

Sommario

La descrizione dei processi che caratterizzano gli ambienti sedimentari fluviali costituisce una tematica di grande interesse non solo in ambito ingegneristico ambientale, ma anche in quello idrogeologico. Gli alvei naturali presentano un'estrema eterogeneità e la loro forma va necessariamente vista come il risultato dell'azione combinata dei processi di erosione, trasporto e deposito dei sedimenti. Le cause che inducono un alveo ad assumere naturalmente una determinata configurazione vanno quindi ricercate nell'interazione esistente tra i flussi dacqua e di sedimenti in ingresso al bacino di drenaggio e tutti quei fattori che concorrono alla formazione del paesaggio, ovvero: la topografia e le caratteristiche idrogeologiche della piana alluvionale, il tipo di sedimenti al fondo, il materiale che costituisce le sponde ed il tipo di vegetazione che su di esse cresce. Nella presente tesi focalizzeremo la nostra attenzione sugli alvei ad andamento meandriforme il cui sviluppo planimetrico è strettamente associato all'erodibilità delle sponde e alle caratteristiche del campo di moto. In particolare, verrà sviluppato un modello numerico in grado di simulare lo sviluppo planimetrico di tali corsi d'acqua, le cui caratteristiche morfologiche sono strettamente legate al carattere sub o super-risonante del regime morfodinamico dominante. Obiettivo del presente lavoro è quello di valutare, sul lungo periodo, le caratteristiche morfologiche degli alvei meandriformi determinate dalla struttura non lineare dell'equazione integro-differenziale che descrive levoluzione planimetrica dell'asse del canale e dalla natura fortemente non lineare del fenomeno del cosiddetto taglio di meandro (comunemente noto in letteratura come cutoff). La corrispondenza tra le caratteristiche morfologiche delle configurazioni planimetriche calcolate numericamente utilizzando due diversi modelli idrodinamici linearizzati e quelle osservate in natura viene analizzata uti-

lizzando un'analisi delle componenti proncipali (PCA). Mostreremo come il contributo dinamico delle forti non linearità indotte dai processi di cutoff non sia tale da eliminare completamente le caratteristiche morfologiche associate alla struttura del campo di moto. In particolare si constaterà come, seppure molti degli aspetti fondamentali delle configurazioni planimetriche naturali siano ben riprodotti anche utilizzando per il campo di moto delle soluzioni linearizzate molto semplificate, tuttavia, una stringente corrispondenza con gli alvei meandriformi reali sia resa possibile solo dall'adozione di soluzioni più raffinate in grado di analizzare in modo più completo i complessi meccanismi morfodinamici. Inoltre, utilizzando un modello linearizzato di campo di moto in grado di analizzare l'influenza morfodinamica nella sua interezza, sarà possibile l'individuazione di una nuova lunghezza scala caratteristica dei meandri, la quale, essendo in grado di sostenere anche il regime super-risonante, si rivelerà una scelta decisamente migliore rispetto alle vecchie scale spaziali utilizzate per i meandri. Infine, adottando una metodologia d'indagine consolidata nell'ambito dell'analisi delle serie temporali non-lineari ed analizzando la serie degli interarrivi dei cutoff, si metterà in evidenza come nelle dinamiche che regolano lo sviluppo dei sistemi meandriformi non sia riscontrabile né l'esistenza di un chiaro determinismo caotico, né tantomeno una loro tendenza ad auto-organizzarsi (self-organized criticality).

Introduction

There are many reasons for the sustained attention paid to meandering rivers by the geology, geomorphology, hydrology, and physics communities [Leopold and Wolman, 1957, 1960; Allen, 1965; Scheidegger, 1967; Schumm and Khan, 1972; Leeder and Bridges, 1975; Callander, 1978; Schumm, 1985]. The motivations range from the challenge of explaining complex natural phenomena in relatively simple terms to very practical industrial and environmental applications [Wicker, 1983; Salo et al., 1986]. One example of the latter is the interest of the oil and gas industry in oil reservoir formations created by ancient meandering rivers [Henriquez et al., 1990; Swanson, 1993]. The complex dynamics and strong segregation effects associated with meandering rivers lead, in fact, to the formation of porous sand bodies embedded into impermeable shales. The shales may act as traps and may also impede fluid flow between sand bodies. In addition, meandering river dynamics leads to a complex internal structure within the sand bodies and shale deposits. A better understanding of the distribution of the permeability and porosity could surely have an important economic impact on oil and gas industry.

Studies of meandering rivers can be divided into several categories according to the scale of interest. In a meandering river system, scales governing physical processes vary from the submicron scale of clay particles and of the surface roughness of sand grains to overall river basin scales of hundreds or thousands of kilometers. Reflecting this range of scales, a number of studies have been carried out on the flow field in natural or artificial curved channels [Thorne and Hey, 1979; Dietrich and Smith, 19 83; Smith and McLean, 1984; Thorne et al., 1985], on the segregation of materials with different grain sizes in meander bends [Bridge and Jarvis 1976; Parker and Andrews, 1985; Bridge, 1992], on the

morphological features and the dynamics of individual meanders [Langbein and Leopold, 1966; Brice, 1974; Hickin, 1974], and on the complex properties of entire meander trains [Schumm, 1963, 1968; Ferguson, 1975; Lapointe and Carson, 1986; Furbish, 1991].

A wide range of approaches has been used in the attempt to explain both the geometry and the dynamics of meandering rivers. They include theories based on the minimum energy dissipation rate hypothesis [Chang, 1979, 1988], models based on the most probable path assumption [von Schelling, 1951; Langbein and Leopold, 1966; Thakur and Scheidegger, 1970], and erosion models obtained by studying the instabilities of the flow in channels by using perturbation methods [Callander ,1969; Engelund and Skovgaad, 1973; Ikeda et al., 1981; Parker et al., 1982; Blondeaux and Seminara, 1985; Parker and Andrews, 1986]. An analogy between thermodynamics and meandering systems has been also pursued by Scheidegger [1967] on the basis of the theory of minimum variance in meandering rivers. It must however be noted that theories based on optimization concepts such as minimum energy dissipation and minimum variance do not have a firm theoretical foundation and do not provide a satisfactory explanation of meandering river geometry. On the other hand, statistical models, most of which derived heuristically, although generating meandering patterns that look realistic at large scales [Thakur and Scheidegger, 1968, 1970; Ferguson, 1973,1976], cannot be used to model the river evolution process, which often is of greater interest than the shape of individual meanders or meandering rivers viewed at one instant in time.

Process-based bend erosion models [Ikeda et al., 1981; Parker et al., 1982; Parker and Andrews, 1986] have been shown to successfully reproduce quantitative relationships between flow and the initial development of meanders from a straight river channel configuration and, therefore, are more suitable to our purposes. Nevertheless, A number of other physical processes has to be accounted for in order to reproduce the complex geometry of meandering rivers, especially at the meander-train scale. Many of the relevant processes, such as channel shortening via cutoff processes, are highly nonlinear. The changing river geometry also leads to a complicated and constantly evolving sedimentary environment in the flood plane, owing to segregation processes acting during deposition and reworking

by the river. This complex sedimentary environment in turn affects the dynamics of the meandering river, making it difficult to establish an unambiguous relationship between theoretical models and the resulting channel form. Finally, geological conditions may vary over the long timescales which characterize the evolution of meandering rivers. Thus the long term prediction of the behavior of meandering rivers remains a challenging problem [Schumm,1 983; Howard and Knutson, 1984].

The rest of the thesis is organized as follows. Chapter 1 briefly presents a geomorphological classification of alluvial channel patterns. Chapter 2 summarizes the mathematical formulation of the long-term planform evolution of meandering erodible channels. In particular, a nonlinear integro-differential planform evolution equation, a suitable erosion rule relating the lateral migration speed of the channel to stream hydrodynamics and a model of flow and bed topography in sinuous channels are the basic tools required to understand how meandering rivers evolve in space and time. Chapter 3 deals with the numerical procedure adopted to simulate both the short and long-term dynamics of meandering rivers. Chapter 4 analyzes the geometric characteristics of long-term planform configurations computed using two different linearized flow field models exhibiting a different degree of approximation. Principal component analysis (PCA) is used to pursue the comparison between synthetically generated patterns and a set of real meandering planforms occurring in different environmental contexts. Moreover, the presence in long term planimetric configurations and in the geometry of the abandoned channels (oxbow lakes) of distinctive flow field signatures is discussed with particular attention to the existence of the characteristic spatial scales which emerge when the full range of morphodynamic regimes is accounted for. In Chapter 5, nonlinear time series analyses are used to investigate both spatial and temporal patterns obtained from the mathematical model which has been shown to contain the fundamental ingredients needed to reproduce correctly the features of real rivers. In particular, the signatures of possibly chaotic dynamics or self-organized criticality triggered by repeated cutoff events are investigated. Finally, Chapter 6 draws some conclusions.

Chapter 1

Geomorphological classification of channel patterns

1.1 Introduction

Alluvial channels show a large variety of planform patterns. The form, or morphology, of a channel is the result of the ceaseless processes of sediment erosion, transport and deposition operating within the constraints imposed by the geologic architecture of the alluvial floodplain. Although natural channels form a continuum spectrum of morphological patterns [Leopold and Wolman, 1957], for engineering and management purposes it is useful to classify channels using a range of channel types that minimize variability within them and maximize variability between them [Thorne et al., 1997]. Indeed, rivers can be considered as morphological units which continuously evolve in relation to the regional climate, local weather and hydrologic regime. In this respect, the shape of an alluvial stream represents a dynamical equilibrium state which can be explained only by considering the action of all those variables (i.e. water discharge and sediment supply) which lead to the formation of the channel. The coupling of these variables with boundary conditions characterizing the alluvial floodplain (i.e. valley slope, bed sediments, bank materials and riparian vegetation) produces the morphology characterizing a given stream.

Most classification systems are based on the analysis of the planform pattern of the

river, but others include information on its cross-sectional shape and type of bed sediment (gravel, sand, or silt/clay). In this contest, following the pioneeristic contribution of Leopold and Wolman [1957], and thus accepting the criteria whereby there is no sharp distinction among planform patterns, we report the general relationship between sediment load, channel stability and channel form proposed by Schumm [1977], which allows us to grade from straight, through meandering to braided rivers with no abrupt interruptions in between (Figure 1.1). Straight or slightly sinuous channels are characterized by fine sediment moving in suspension and highly resistant banks. Therefore, they represent the less active planform configuration (types 1 and 2 in Figure 1.1). Meandering rivers (types 3 and 4 in Figure 1.1) are mixed-load streams with greater sediment supply and more erodible but somewhat resistant banks. Braided rivers are multi-threaded patterns with friable bank material and characterized by a significantly high and relatively coarse bedload transport (type 5 in Figure 1.1). Finally, in the event that the braid bars (anabranches), which commonly form braided channels, grow to the extent that they stabilize as semipermanent islands, the channel pattern is conventionally classified as anastomosed.

Although separation of distinctive patterns is somewhat arbitrary and different planform types can be observed along the same water course, for simplicity each major pattern is discussed separately in the following sections.

1.2 Straight channels

Straight reaches are generally present in the upper parts of rivers where channel slope is steep and river bed consists of coarse material, such as gravel, cobbles and boulders. Certainly, it is easier to find example of meandering, braided or anastomosed rivers than to find long straight reaches. In fact, rivers are seldom straight through a distance greater than about ten channel widths [Leopold et al., 1964], and so the definition of straight rivers must include also irregular, sinuous or simply non-meandering channels. For purposes of definition Leopold and Wolman [1957] classified a stream as straight using the tortuosity σ_T (ratio of channel length to valley length) as a criterion. Rivers having tortuosity of

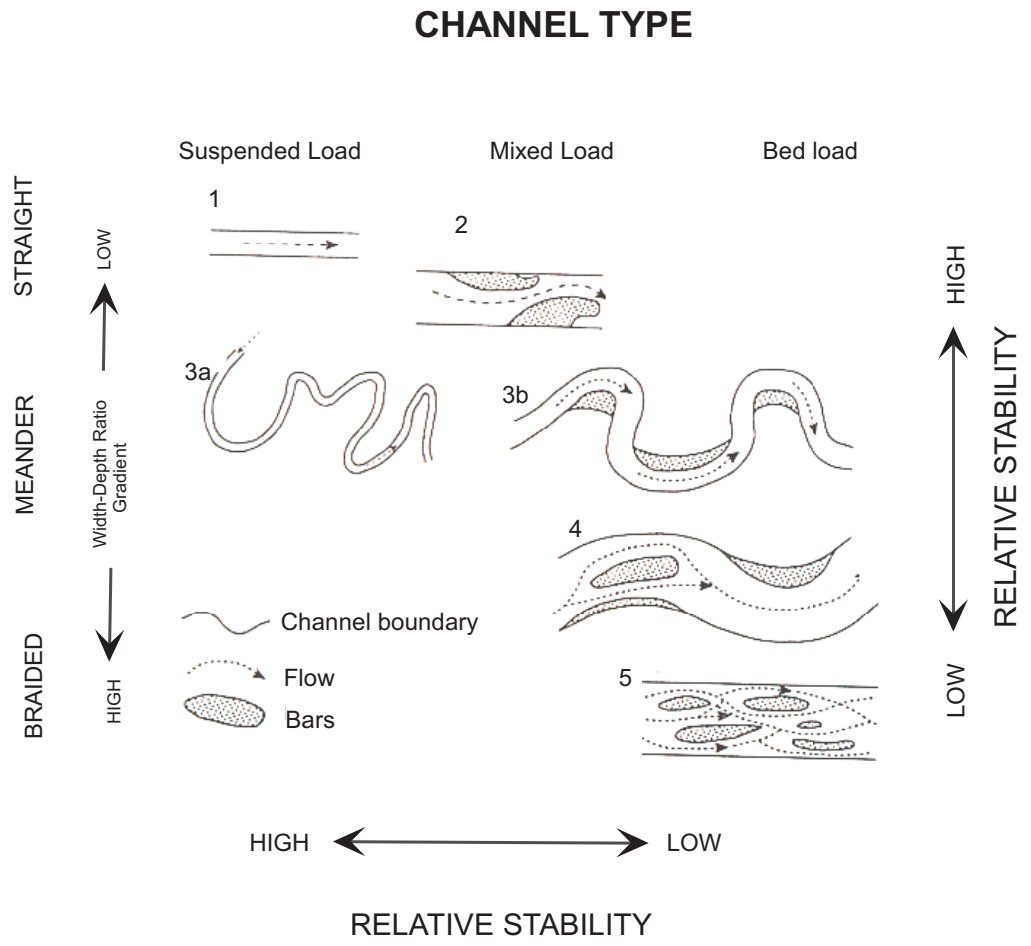

Figure 1.1: Classification of channel pattern based on sediment load and system stability after Schumm, 1977. [Thorne et al., 1997]

1.5 or greater are considered as meandering, on the contrary if their σ_T is below 1.5 they are called sinuous or straight.

The rarity of this kind of pattern can be directly related to both the variability of the topography and the heterogeneity of the sediment characterizing the alluvial floodplain. Even where the river is straight for a significant reach both the thalweg (line of maximum scour) and the maximum velocity streamline usually oscillate back and forth from one bank to the other. In particular, a point bar (a deposit of sediment) typically forms opposite to the deepest point. These bars tend to alternate (Figure 1.2) from one side to another describing a sinuous path and forming poll-riffle sequences which are clearly defined in gravel-bed rivers but can also be detected in sand-bed streams. Riffle bars are the highest points in the bottom profile, while scour pools are the lowest ones (Figure 1.3). The heterogeneity of bed material size can affect significantly the formation of pool-riffle sequences in non-meandering channels.

Despite the apparent simplicity of the overall form of this type of channel pattern, the links between planform and cross-sectional geometries, as well as the main features of the stream (i.e. flow resistance and sediment movement), are complex phenomena which can be explained only in terms of pool-riffle combinations.

1.3 Meandering

The study of meanders has been subject to considerable attention by geomorphologist and, more recently, also by engineers. However, only in the last three decades a series of mechanistic approaches have been developed to understand the basic phenomena subtending the formation/evolution of meanders, while the previous literature was mainly focused on the description of meander geometry.

Rivers freely flowing in alluvial flood plains are very seldom straight. Meandering patterns formation typically occurs in relatively low gradient valley with a dense vegetation cover and cohesive soils. According to Murray and Paola [1994] meandering can be seen as a particular case of braiding, characterized by a single-thread channel, occurring when the sediment is cohesive or in presence of riparian vegetation. Indeed, most natural

Figure 1.2: Alternate bars in the Rhine River, Switzerland [Jaeggi, 1984]

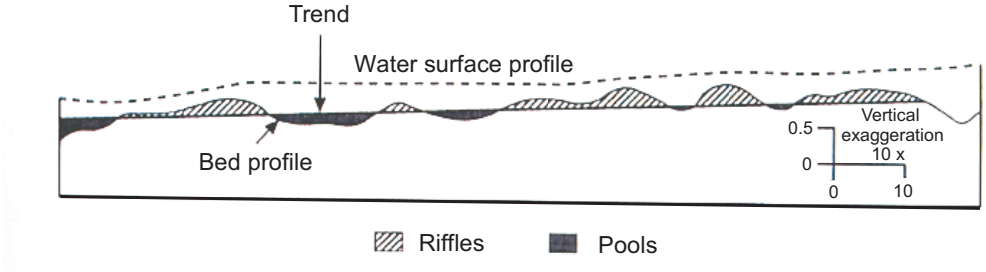

Figure 1.3: Pool-riffle sequence in the Fowey River, England (Thorne et al. [1997], modified from Richards [1982]).

Figure 1.4: Typical examples of fluvial meandering patterns carved in a rocky environment characterized by tectonic uplift (a), as well as wandering through flat and vegetaded valleys (b,c). a) Goosenecks of the San Juan River, Utah, USA. b) Rio Tamaya, Peru; note several abandoned loops (oxbow lakes) which rearrange the alluvial floodplainn. c) Amazon River, Brasil; note the presence of huge compound bends close to cutoff conditions.

meandering rivers flows through forests or in alluvial plains covered by vegetation (see Figure 1.4 b,c), whereas poorly vegetated banks tend to be associated to braided rivers [Leopold et al., 1964].

The flow field in meandering rivers is governed by the alternate succession of opposite bends. The interaction between the centrifugal force (induced by the curvature of the channel), the vertical gradient of the main flow velocity and the transverse pressure gradients (due to transverse inclination of the water surface) produces a secondary flow. This transverse circulation, combined with the longitudinal main current, produces the helical flow that is typical of meandering bends. In the case of a cohesionless bed, sediment particles are driven inwards by the secondary flow establishing a transverse bed slope (Figure 1.5). In such configuration, the thread of high velocity is shifted towards

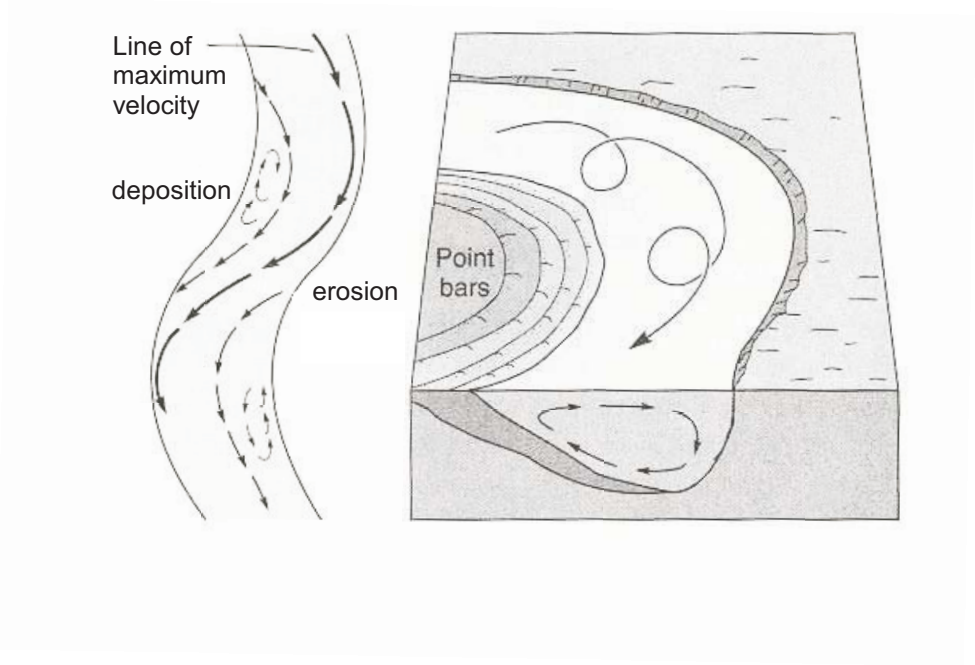

Figure 1.5: Sketch of the effects induced by secondary circulation in meandering bends.

the outer bank, inducing its erosion, and deposition of sediment along the inner bank. This determines the tendency of meander loops to amplify.

As a consequence, the progressive development of meandering rivers planimetry can be explained as the result of a self-forming process essentially consisting of an intermittent sequence of erosion of concave banks and accretion associated with deposition at convex banks. In this context, sediment is eroded from the outer bank causing local bank retreat, and deposited more downstream near the inner bank [Friedkin, 1945], where it contributes to the accretion of the point bar deposit. Owing to this configuration of the river bed the thalweg goes from one bank to the other crossing the channel at inflection points (i.e., where the channel curvature change sign).

The abrupt change of curvature experienced by the channel along its course disturbs the flow field. The bottom topography reacts to the new equilibrium state caused by the change of curvature through a sequence of damped steady oscillations of transverse bed slope (free steady bars). This phenomenon, called overdeepening, was explained theoretically by Struiksma et al. [1985] and later confirmed by Johannesson and Parker

[1989]. The development of such non-migrating spatially decaying bars may occur not only at the bend entrance (downstream morphodynamic influence), but also upstream of the inflection point (upstream morphodynamic influence) as pointed out by Semimara et al. [2001] and Lanzoni et al. [2006]. As a consequence, the direction, downstream or upstream, of meanders migration is directly related to the dominant morphodynamic influence: for channels characterized by width to depth ratios smaller than a threshold value downstream influence dominates the morphodynamics and the meandering pattern is characterized by downstream migration, being the single meanders upstream skewed. The picture completely reverses if upstream influence dominates: meanders migrate upstream with meander loops skewed downstream. The threshold value of the width to depth ratio discriminating these two different morphodynamic behaviours coincides with the resonant value found out by Blondeaux and Seminara [1985]. Upstream influence is associated with super-resonant conditions whereas downstream influence occurs in sub-resonant channels (see Chapter 2).

Meanders are usually defined in terms of their shape, bend radius of curvature, wavelengths and meander belt. In this study, according to Leopold et al. [1964], a meander is defined as segment of stream lying among three inflection points. Meander sinuosity σ_f (the f subscript refers to full meander quantities) is thus defined as the ratio between intrinsic (L_f) and cartesian (ℓ_f) meander wavelengths (Figure 1.6), and meander belt represents the corridor (Λ) along the floodplain across which the meandering stream periodically shifts its channel (Figure 1.7a). The channel width at the dominant discharge (i.e., formative discharge) is generally used to scale all the geometric meandering features.

On the basis of field observations, Langbein and Leopold [1964] suggested that periodic sequences of low amplitude symmetric meanders typically characterize the first stage of meandering rivers. In this scenario a sine-generated curve can resemble an idealized meandering river. However, under the absence of geological or anthropic constraints, meanders usually evolve towards shapes that are fattened and skewed with respect to the sine generated curve. This asymmetry is associated with the fact that the point of deepest bed scour and of maximum attack on the outer bank are usually shifted downstream

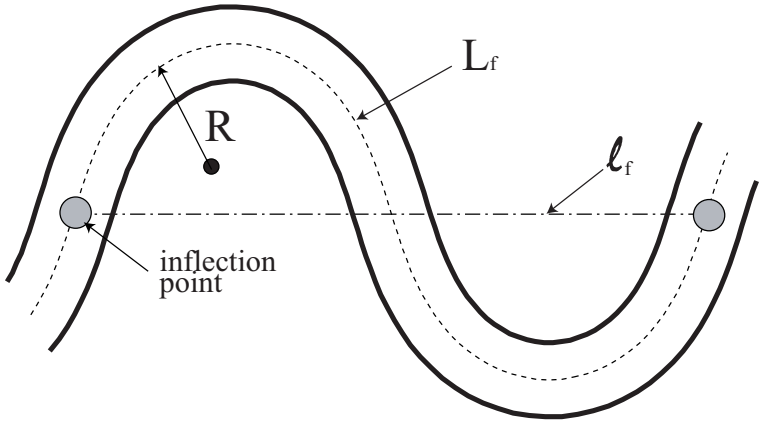

Figure 1.6: Sketch of a meandering channel. A meander is defined as segment of stream lying among three inflection points: L_f is the intrinsic full meander wavelength, ℓ_f is the cartesian full meander wavelength, R is the local radius of curvature of the bend.

(or upstream depending on the dominant morphodynamic influence) of the geometric apex of the bend. Kinoshita [1961], pointed out that such planimetric pattern can be described by correcting the sine-generated curve, through the inclusion of third harmonics. The latter feature, however, is not the only characterizing the real shape of meandering rivers. Indeed, simple bend, compound bends, and multiple loops (Figure 1.7a,b) are morphological units often observed in real meandering rivers [e.g., Brice, 1974; Hooke and Harvey, 1983]. A second important field observation which applies to freely developing meanders is the gradual reduction of the migration rate [Kinoshita, 1961] and the initial increase and eventual decay of lateral migration rate [Nanson and Hickin ,1983].

In a natural meandering river system various processes act to segregate and deposit granular materials producing different types of sediment, namely point bar formation, cutoff, natural levee growth and crevasse-splay [Allen, 1965]. Point bar and cutoff deposits are the most important and characteristic features of meandering systems, and account for the largest portion of the material deposited within the meander belt. As already mentioned, point bar deposits result from lateral migration of the channel and are composed of coarse material, with the grain size usually decreasing with height. When a river cutoff occurs, the isolated former river reach forms an oxbow lake. The sediments that fill the oxbow lake are mainly clay and silt. Although some sandy deposits are also

Figure 1.7: a) Jurua River, Peru (GoogleEarth). Yellow lines denote qualitatively the meander belt width, Λ. Note the coexistence of simple bend, compound bends and multiple loops upstream and downstream skewed. b) Mara River, Kenya. Note the presence of compound bends possibly created by heterogeneities in floodplain erodibility associated with cutoff deposits and the presence of vegetation.

found in cutoff sediments they are a minor component and never occupy more than the ends and a very thin layer at the top of the cutoff deposition.

Two different types of cutoff are usually recognized in natural channels, i.e., chute and neck cutoffs [Allen, 1965]. Chute cutoffs are relatively long flow diversions which occur when a meander loop is bypassed through a new channel which forms across the bar enclosed by the loop. They most frequently form in wide channels with large curvature bends, high discharges, poorly cohesive, weakly vegetated banks, and high gradients. This process is important in meandering rivers with restricted sinuosity. Neck cutoff forms when the local sinuosity becomes large enough for adjacent loops to touch causing the channel to reconnect at the neck of the loop while abandoning the former loop. Thus, this latter type of bend cutoff processes characterize high-sinuosity meandering rivers.

Figure 1.8: a) Peculiar coexistence at one single bend of both chute and neck cutoff. b),c) typical examples of neck cutoff process. The picture b) also shows how the oxbow lake formed by channel shortening is progressively filled by sediments.

1.4 Braiding

When the valley gradient becomes milder rivers generally assume a multithreaded, braided pattern. The separate channels of a braided stream are divided by ephemeral islands, formed by large deposits of sediments, which are often submerged at high flow (Figure 1.9). Compared to single-thread channels, the mechanisms which drive an alluvial system in producing a braided pattern is rather complex and it is not yet completely understood. In fact, engineers and fluvial geomorphologists have, until recently, associated braided rivers almost exclusively with a state of disequilibrium of the fluvial system. Nevertheless, Leopold and Wolman [1957] pointed out that braided patterns belong to a distinct type of dynamically stable planforms, likewise straight and meandering rivers. Clearly, it is difficult to recognize this stability in a system which exhibits rapid and unpredictable changes owing to sediment deposition and bed aggradation.

The origin of morphological descriptions of braided patterns stems form the work of Leopold and Wolman [1957]. Figure 1.10 describes the processes by which a single-thread channel evolves into a braided channel. In a river characterized by high and relatively coarse bedload, the formation of a central bar of sediment induces a flow deflection which, in turn, starts eroding the banks. The resulting bank migration, furnishing new sediment supply to the channel, works as a feedback for the further growth of the bar (Figure 1.10,A). As the bar growth, strong secondary currents, induced by the the separation of the main flow, scour the bed and further erode the outer bank of the channel while driving deposition of sediment along the inner margins of the anabranches (Figure 1.10,B-C). Bed scour in the divided reach drops the water surface elevation and, as a consequence, the top of the central bar emerges. Through time, this braid bar can develop triggering multiple flow divisions and subchannels (Figure 1.10,D-E). Finally, the formation of a central bar in each of the anabranch channels leads to further braiding processes following the same sequence of events. This subdivision of the main channel into increasing numbers of anabranches continues until the flow is no longer able to erode the outer banks which represent the input of sediments for the building of new braid bars [Leopold and Wolman, 1957, 1964]. Thus, the resulting planform configuration is rather complex and character-

Figure 1.9: Three example of braided rivers: a) Tasman River, New Zealand; b) Rakaia River, New Zealand; c) Tagliamento River, Italy.

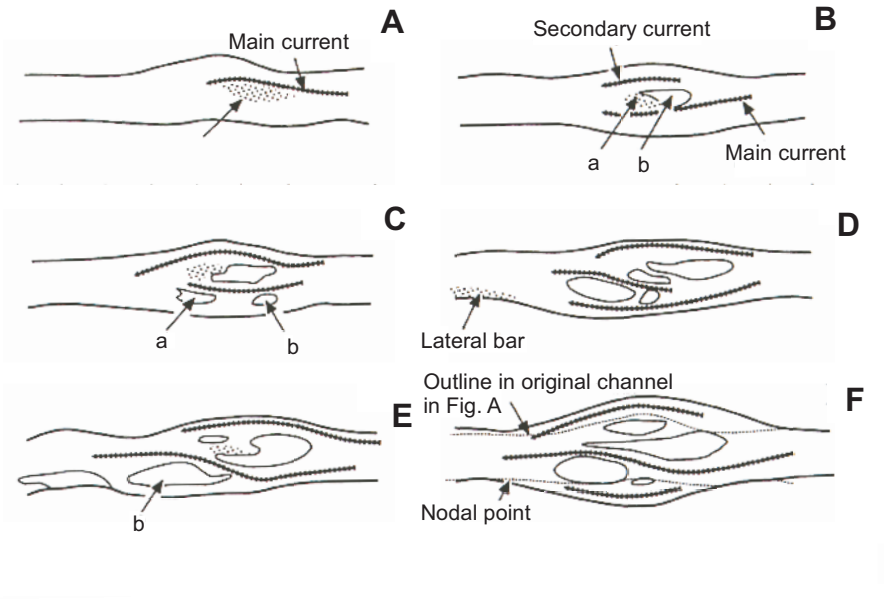

Figure 1.10: Development of a braided channel (after Leopold and Wolman, [1957]).

ized by long and wide multithreaded bar-island reaches alternated with short and narrow single-thread channels (Figure 1.10,F).

1.5 Anastomosing

Anastomosing was for many years viewed as a particular intense form of braiding [Leopold and Wolman, 1957]. However, following the work of the past three-four decades, it is now generally accepted that an anastomosing river is a multi-channel river (Figure 1.11) which is fundamentally different in form and process from a braided river.

Schumm [1968] is likely the first who pointed out that the term anastomosing should not be used as a synonym of braiding. However, Rust [1978] was the first proposing a qualitative diagram, based on channel tortuosity and braiding parameter (i.e., the number of braids per mean meander wavelength), describing the continuum of patterns given by straight, braided, meandering and anastomosed rivers (Figure 1.12).

The first distinctive difference between braiding and anastomosing relates to channel morphology [Ferguson, 1987]. In fact, braided rivers have a straight or slightly sinuous

Figure 1.11: Typical examples of anastomosing rivers: a) Columbia River, British Columbia, Canada; b) Matanuska River, Alaska, USA.

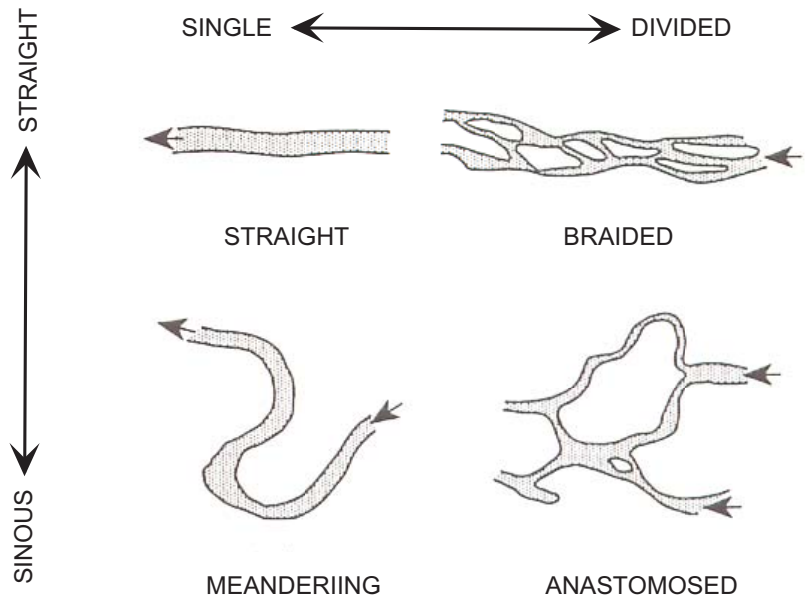

Figure 1.12: Channel patterns classification based on tortuosity and braiding parameter (i.e., degree of channel division). Thorne et al. [1997], adapted from Rust [1978].

channel in which flow diverges and converges around relatively small, mobile and unvegetated bars. The highest elevation of these bars is slightly lower than the elevation of the surrounding floodplain and, therefore, the bars are submerged at bankfull discharge conditions. On the contrary, anastomosed rivers have two or more high sinuous channel separated by large, semi-permanent, vegetated island. The highest elevation of the islands are about equal to that of the surrounding floodplain, so that the pattern remains multithreaded even at bankfull stage.

The second distinctive difference relates to channel slope [Ferguson, 1987]. Braided rivers usually have relatively steep slopes if compared to rivers with similar discharges and single-thread, meandering channels. On the contrary, anastomosed rivers have slopes which are as low or lower than those associated with equivalent meandering rivers.

Finally, Makaske [2001] proposed the following definition of anastomosing, which couples floodplain geomorphology and channel pattern: *"an anastomosed river is composed of two or more interconnected channels that enclose flood basins"*. Anastomosed patterns are thus classified as rivers having multiple coexistent channel belts, while braided as

regarded as river with a single channel belt, but multiple thalwegs.

Anastomosed rivers then constitute an important category of multi-channel rivers on alluvial plains usually formed by flow diversions (i.e. avulsions) that cause the formation of new channels on the floodplain. As a product of avulsion, anastomosed rivers essentially form in two ways: (1) by formation of bypasses, while bypassed older channel-belt segments remain active for some period; (2) by splitting of the diverted flow, leading to contemporaneous scour of multiple channels on the floodplain. Both genetic types of anastomosis may coexist in one river system, but whereas the first involves a wide portion of the floodplain, the latter only represents a stage in the avulsion process on a restricted part of the floodplain.

Chapter 2

Planimetric evolution of meandering rivers: mathematical framework

2.1 Introduction

Meandering rivers are highly nonlinear dynamic systems, which produce complex and fascinating planimetric patterns. Understanding the nature of morphologic changes of these rivers has long attracted the attention of the scientific community, both in the fields of fluvial geomorphology and hydraulic engineering. Various types of approaches have so far been proposed to explain how and why meanders are initiated and how they evolve. In the early stages of geomorphologic studies, the statistically stable relations obtained between meander parameters (i.e, meander length, channel width and radius of curvature of bends) suggested an interpretation of meander forms in terms of a quasi-equilibrium state, characterized by bends of almost permanent form migrating downstream [Leopold and Wolman, 1957, 1960; Langbein and Leopold, 1966]. Subsequent analyses of planform changes over historical timescales, however, pointed out the lack of equilibrium forms. Meandering systems were found to exhibit a wide range of behaviors [e.g., Hooke, 2007; Seker et al., 2005; Goswami et al., 1999], varying from meanders which are evolving very slowly (e.g., channels in bedrock or resistant material, channels with highly vegetated banks or very low slope reaches) to those which are highly complex and dynamic (Figure

1.4 and 1.7). These latter systems, often displaying a relatively high sinuosity, were associated with a typical tendency of meanders towards a non-linear autogenic behavior, due to intrinsic factors [Brice, 1974; Hickin, 1974; Hooke, 1984; Guccione, 1984]. Nonlinearities were thought as the cause of the wide variety of bend forms observed in nature, namely upstream (downstream) skewed bends, compound bend, and multiple loops, whereby upstream and downstream skewed bends coexist. Systematic monitoring of the planform evolution of meandering rivers in particular suggested that the formation of compound bend is one of the key process whereby new bends develop [Hooke and Harvey, 1983].

More recently, mainly in the last two decades, mathematical modelling has provided a deeper insight into meander dynamics [Ikeda et al., 1981; Blondeaux and Seminara, 1985; Johanneson and Parker, 1989; Zolezzi and Seminara, 2001] and meander formation has been explained in terms of a two-dimensional instability process (bend instability) driven by bank erosion [Seminara, 2006].

2.2 Mathematical formulation of bend instability

The mathematical problem governing the planform evolution of meandering channels has been thoroughly described, among others, by Seminara [2006], Lanzoni et al. [2006], Lanzoni and Seminara [2006]. Therefore, to set the scene for our discussions, we only briefly summarize the main ingredients of the problem. With reference to the notations of Figure 2.1, let us consider the permanent flow in a wide meandering channel with constant width $2B_0^*$, uniform and cohesionless sediment, with diameter d_s^*, and gently sloping erodible banks. Moreover, let D_0^* the reach averaged flow depth and U_0^* the depth averaged longitudinal velocity. Hereinafter a star superscript will denote dimensional quantities.

Following a framework stemming from the seminal work of Ikeda, Parker and Sawai [1981], we refer the flow field and bed topography to the orthogonal intrinsic reference system (s^*, n^*) illustrated in Figure 2.1, where s^* is the longitudinal coordinate locally coinciding with channel axis tangent, and n^* is the transverse coordinate, with origin at the channel axis. The problem of predicting the planform evolution of erodible channels

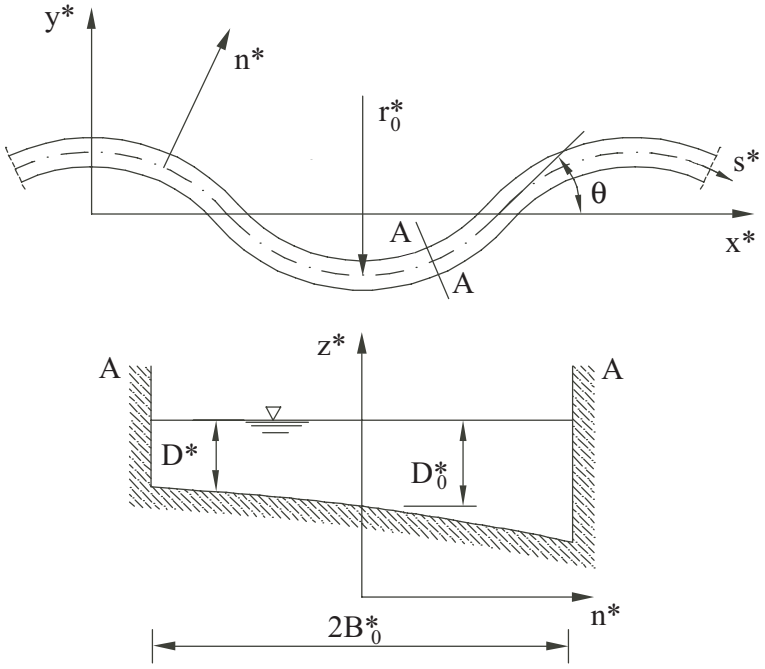

Figure 2.1: Sketch of the meandering channel and notations.

then reduces to determining the motion of a line (the channel centreline) lying on a plane (a flat valley), such that each point of the channel centerline evolves in time moving in the normal direction n^* with some lateral migration speed ζ^*, driven by bank erosion processes. Observing that, at a given time t^*, the channel axis configuration is described by the distribution $\theta(s^*, t^*)$ of the angle that the local tangent to the channel axis forms with the direction of a Cartesian axis x^*, the following non linear integro-differential planimetric evolution equation can be derived [Seminara et al. 2001]:

$$\frac{\partial \zeta}{\partial s} = \frac{\partial \theta}{\partial t} - \frac{\partial \theta}{\partial s} \int_0^s \zeta \frac{\partial \theta}{\partial s} ds \tag{2.1}$$

where the following scaling has been adopted:

$$(s^*, n^*) = B_0^*(s, n), \quad \zeta^* = U_0^* \zeta, \quad t^* = U_0^* t / B_0^* \tag{2.2}$$

The mathematical formulation of the problem next requires a suitable erosion law relating bank erosion process to stream hydrodynamics. The process of meanders migration is essentially governed by erosion at outer bank and deposition at inner bank of

Figure 2.2: Point bar deposits at the inner side of bends in a meandering channels.

channel bends. Usually, bank erosion is an intermittent and heterogeneous process, whose mechanism is rather complex. In fact, erosion may be associated with several causes, like bank collapse due to scour at the bank toe or development of tension cracks, groundwater seepage and vegetation [Darby and Thorne, 1996; Darby, 1998; Darby et al. 2002]. However, for long-term investigations, it is more appropriate to rely on an integrated description of the erosion process. In this approach, on the very slow time scale associated with channel planimetric development, erosion and deposition processes can be considered as contemporaneous events and, consequently, bank erosion may be modelled as a continuous process which keeps nearly constant the average width of the river (see Figure 2.2). In other words, the transient process whereby sediment eroded at concave banks is deposited at convex banks is taken to occur instantaneously. Once again, following Ikeda et al. [1981] we set:

$$\zeta = E\, U_b \tag{2.3}$$

where U_b is the near-bank velocity increment of the perturbed flow, scaled by U_0^*, and E is a dimensionless long-term erosion coefficient.

In order to complete the formulation of the problem we finally need a hydrodynamic model of flow field in sinuous channel with cohesionless bed and an arbitrary distribution of

channel curvature. The availability of such a model allows us to determine the quantity U_b appearing in equation (2.3) as a function of channel curvature ($\propto -\partial\theta/\partial s$), thus expressing the integro-differential equation (2.1) entirely in terms of the unknown function $\theta(s,t)$.

A number of hydrodynamic models have been so far proposed in the literature. In the present thesis we refer to two physics-based linear models, characterized by a different degree of approximation, namely the models proposed by Ikeda et al. [1981] and Zolezzi and Seminara [2001] (hereinafter referred to as IPS and ZS, respectively). These two models, which predict various important mechanisms operating in bend instability, can be regarded as the simplest and the much more refined tools among the category of physically based models. Both models have been derived under the assumptions of steady flow conditions, bedload dominated sediment transport, and do not account for the possible coexistence of free migrating and forced steady bars. The major difference between the two models (see also Section 2.4) is the full coupling between hydrodynamics and sediment transport present in the ZS model. The model developed by Johannenson and Parker [1989] was not considered simply because, as discussed in Camporeale et al. [2007], it represents an intermediate level of completeness in the hierarchy of linearized models.

2.3 The nature of bend instability: linear theory

Meanders form because, the straight configuration, which corresponds to the simplest solution of the planform evolution equation (2.1) is, in general, not stable. This type of instability is usually denoted as bend instability. Thus, bend instability can be defined as the process whereby a perturbation of an initially straight channel alignment grows, driven by bank erosion, and leads eventually to the development of a meandering pattern.

Following a classical normal mode approach, the main features of bend instability process may be stressed performing a planimetric stability analysis [Lanzoni and Seminara, 2006]. The basic state of the channel is taken to be the straight configuration, defined by the simple relationship $\theta = 0$. Moreover, the small perturbation of this basic state is taken to be a sequence of so called sine-generated meanders [Langbein and Leopold, 1964]

which are characterized by a sinusoidal distribution of channel curvature:

$$\theta = \theta_1 \exp i(\lambda s - \omega t) \tag{2.4}$$

where θ_1 is the small initial amplitude of the perturbation, λ is the intrinsic meander wavenumber, scaled by $1/B_0^*$, ω is the angular frequency, scaled by U_0^*/B_0^*, and i is the imaginary unit. Using the linearized form of the bend evolution equation (2.1), the erosion rule (2.3), and a suitable hydrodynamic model, one eventually derives a dispersion relationship for bend instability, i.e. a relationship between the complex quantity ω and the meander wavenumber λ. The functional relationship for the angular frequency turns out to be of the form:

$$\omega = \mathcal{F}[\beta, C_f, \tau_*, \lambda] \tag{2.5}$$

where β ($= B_0^*/D_0^*$) is the bankfull aspect ratio, C_f is the friction coefficient, which in general depends on the dimensionless grain size $d_s = d_s^*/D_0^*$ and on the bed configuration (i.e., plane or dune-covered), τ_* is the Shields parameter (a dimensionless measure of the bed shear stress). The imaginary part, ω_i, of the angular frequency represents the temporal growth rate of perturbations while the dimensionless complex phase and group velocities are given by $a = \omega/\lambda$ and $\partial\omega/\partial\lambda$, respectively. Relationships for meander growth rate (ω_i,) and migration speed a_r (real part of the dimensionless complex phase) as functions of meander wave number λ and for given values of the relevant parameters (β, C_f, τ_*) can be readily obtained from equation (2.5). The dispersion relationship thus allows one to characterize the main features of the bend instability process.

The arising scenario can be briefly summarize as follows. The bend instability process tends to select a meander wavelength λ which, in general, depends on the aspect ratio β of the channel, on the intensity of sediment transport and on flow resistance. Moreover, the response of the system tends to grow indefinitely for specific (resonant) values of the dimensionless intrinsic wavenumber and of the aspect ratio, λ_r and β_r. Figure (2.3) shows the resonant values λ_r, and β_r as functions of τ_*, and d_s, for both plane bed and the dune covered bed conditions. The plots are similar to those obtained by Seminara and Tubino

[1992], but here various bedload predictors have been considered.

The bed pattern associated with resonance consists of stationary (i..e, non migrating) sediment waves, arranged in periodic sequences of riffles and pools in alternate fashion. Note that this bed configuration would not develop spontaneously, but is excited by channel curvature at resonance, a condition which can be described only accounting for both curvature-forced variations in velocity and depth and alternate bars. A full coupling between the flow field, the bedload transport and the bed evolution is then needed, as pursued by Blondeaux and Seminara (1985), Johannenson and Parker (1989), Zolezzi and Seminara (2001). Conversely, resonance cannot be predicted by the dispersion relationship arising from the use of the pioneering approach of Ikeda et al. (1981), in which only curvature forcing is considered and the bed topography is not solved for.

Bar-bend instability theory, besides supporting the idea of an autogenic behavior of meandering channels, also highlights the existence of two distinct morphologic regimes which strongly influence meander dynamics. Theoretical findings [Seminara et al., 2001; Lanzoni et al., 2006] indicate that meandering pattern migrates while amplifying, owing to the occurrence of a phase lag between the erosion and curvature peaks, and that migration speed changes sign as the resonance conditions are crossed. Therefore, under sub-resonant conditions ($\beta < \beta_r$) meanders are typically characterized by upstream skewing and downstream migration (downstream influence) (Figure 2.4). In contrast, downstream skewing and upstream migration are obtained under super-resonant ($\beta > \beta_r$) conditions (upstream influence). The nature of bend instability is consequently not fully described by the IPS model. Indeed, Lanzoni and Seminara [2006] have shown that, in the sub-resonant regime, bend instability is invariably convective and the group velocity of meander trains is positive (downstream migration), while, under super-resonant conditions, bend instability is generally, although not invariably, convective and the group velocity is negative (upstream migration). On the contrary, the IPS model can only describe an invariably convective instability, with a positive group velocity.

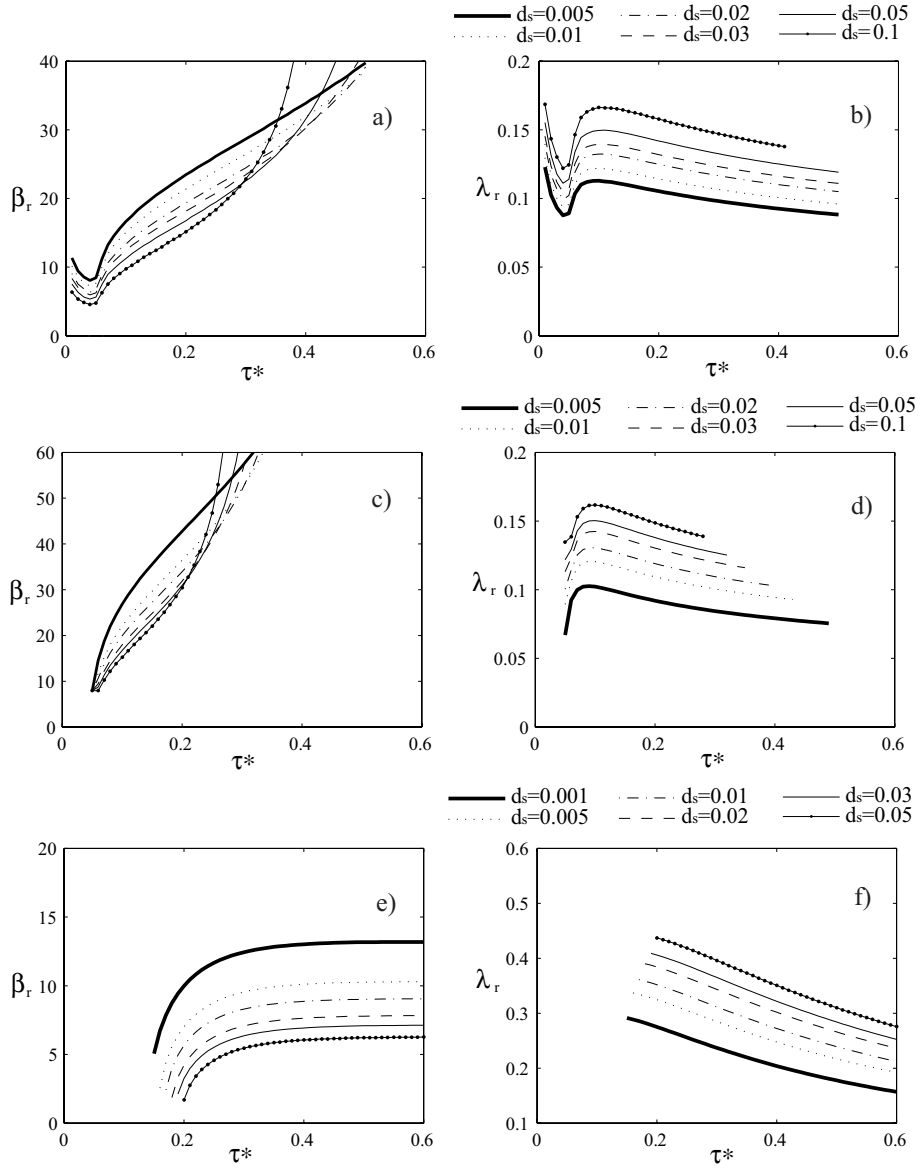

Figure 2.3: The resonant values of the meander aspect ratio, β_r, and of the meander wavenumber, λ_r, are plotted versus shear stress τ_* for give value of the dimensionless grain roughness d_s. a), b) plane bed and bedload transport evaluated through the Parker [1990a] relation. c), d) plane bed and bedload transport evaluated through the Meyer-Peter and Muller formula in the form given by Chien [1956]. e), f) dune covered bed and total sediment transport evaluated through the Engelund and Hansens [1967] formula.

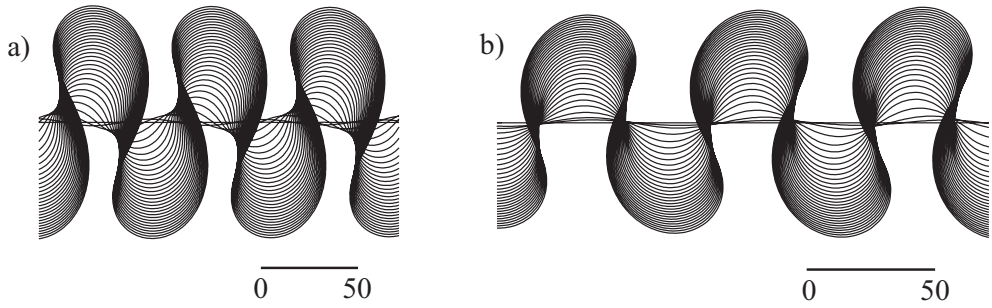

Figure 2.4: Typical response of the planform of an erodible channel to small random perturbations of an initial straight configuration. Run a) (ZS model, $\beta = 15$, $\tau_* = 0.15$, $d_s = 0.01$, plane bed, Parker [1990] formula) is characterized by sub-resonant conditions: meanders travel downstream and are upstream skewed. On the contrary, run b) (ZS model, $\beta = 18$, $\tau_* = 0.1$, $d_s = 0.01$, plane bed, Parker [1990] formula) is characterized by sub-resonant conditions: meanders travel upstream and are downstream skewed. Planimetric dimensionless scales are expressed in half-width units. Flow is from left to right.

2.4 The near-bank velocity increment

The IPS model, thanks to its simplicity, has been so far widely employed in the study of long-term meandering river dynamics [e.g., Howard and Knutson, 1984; Sun et al., 1996; Stolum, 1996; Edwards and Smith, 2002, Camporeale et al., 2005]. In this model the near-bank velocity increment U_b is evaluated by decoupling the hydrodynamic and the sediment conservation equations. The main consequence of this simplification is that resonance cannot occur and, therefore, the model provides only a part of the complete solution of the problem. In particular, the functional relationship for U_b turns out to be of the form

$$U_b = \mathcal{F}\left[\nu_0, \beta, C_f, \tau_*, \mathcal{C}, \int_0^s \mathcal{C}(\xi)\, e^{\lambda_0(s-\xi)}\, d\xi\right] \tag{2.6}$$

where ν_0 is the curvature ratio, defined as the ratio of half channel width to some characteristic value of the radius of curvature of the channel axis, say its minimum value in the meandering reach, $\mathcal{C}$ $(= -\nu_0^{-1}\partial\theta/\partial s)$ is the local value of the channel axis curvature, and $\lambda_0 = -2\beta C_f$ is a characteristic exponent. Equation (2.6) implies that the flow and

bed topography at a given section are affected not only by the local value of curvature but also, through the convolution integral, by the hydrodynamics and morphodynamics of the reaches located upstream (downstream influence).

The ZS model represents an extension to rivers with an arbitrary distribution of channel axis curvature of the bar-bend theory developed by Blondeaux and Seminara [1985]) for sequences of sine generated meanders. This model, similarly to the much simplified version proposed by Johannenson and Parker [1989], includes all the principal morphodynamic mechanisms, although at a linear level. In particular, the coupling of the two-dimensional linearized flow-field with the Exner sediment balance equation implies that meanders behave as linear oscillators which resonate at specific values λ_r and β_r of their intrinsic dimensionless wavenumber λ ($= \lambda^* B_0^*$) and aspect ratio β, depending on the intensity of sediment transport and friction. As discussed in Lanzoni et al. [2006] (but see also Seminara et al. [2001], Camporeale et al. [2007]), the ability of a model to reproduce resonance has important implications for the issues of upstream/downstream morphodynamic and hydrodynamic influence, and for the appropriate choice of the boundary conditions, at least on short time scales. The functional relationship for the near bank velocity increment U_b now reads

$$U_b = \mathcal{F}\left[\nu_0, \beta, C_f, \tau_*, \mathcal{C}, \int_0^s \mathcal{C}(\xi)\, e^{\lambda_{mj}(s-\xi)}\, d\xi\right] \tag{2.7}$$

where λ_{mj} ($m = 0, \infty; j = 1, 4$) are characteristic exponents for the m-th lateral Fourier mode. These exponents are crucial to determine, through the related convolution integrals, whether flow and bed topography at a given position along s are affected by the reaches located upstream (downstream influence) or downstream (upstream influence). Figure 2.5 describes a typical behavior of the characteristic exponents for the first transverse mode $m = 1$. The first two exponents λ_{m1} and λ_{m2} are always real, $O(1)$ quantities, with opposite sign ($\lambda_{m1} > 0$; $\lambda_{m2} < 0$) and, therefore, describe non-oscillatory spatial perturbations which decay fairly fast either downstream or upstream. The other two exponents, λ_{m3} and λ_{m4}, are complex conjugate, with real ($\lambda_{m3r} = \lambda_{m4r}$) and imaginary ($\lambda_{m4i} = -\lambda_{m3i}$) parts which attain values ranging about $0.1 - 0.3$. They describe

oscillatory spatial perturbations which decay fairly slowly, spreading their influence over a considerable channel length. In the sub-resonant regime ($\beta < \beta_r$), the real parts of the complex conjugate exponents are negative ($\lambda_{m3r} = \lambda_{m4r} < 0$) and, therefore, lead to a downstream influence, as in the case of the IPS model: meanders are skewed upstream and migrate downstream. An opposite scenario arises in the super-resonant regime ($\beta > \beta_r$) for which $\lambda_{m3r} = \lambda_{m4r} > 0$, thus leading to upstream influence: meander are skewed downstream and migrate upstream. Clearly, the uncoupled IPS model, being unable to predict the resonance phenomenon, cannot describe the super-resonant regime and the related dominant upstream morphodynamic influence.

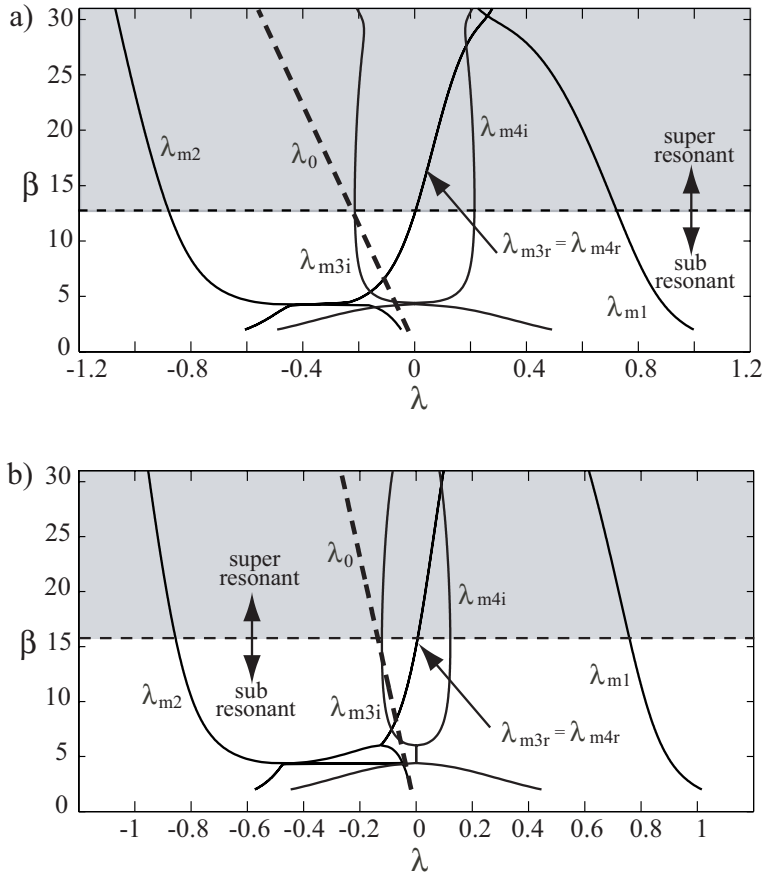

Figure 2.5: Typical behavior of the characteristic exponents of the two considered linearized flow fields models: IPS model (dashed line); ZS model ($m = 1$, solid line). The values of the relevant parameters are: a) $\tau_* = 0.4$, $d_s = 0.001$, dune covered bed; b) $\tau_* = 0.1$, $d_s = 0.01$, plane bed.

Chapter 3

Numerical Aspects

3.1 Introduction

The mathematical problem outlined in Chapter 2 needs to be solved numerically. In the following we describe various aspects of the numerical procedure adopted to compute the spatio-temporal evolution of meandering patterns.

3.2 Numerical algorithm

Rather than solving numerically the integro-differential equation (2.1), we have followed the computational procedure firstly proposed by Howard (1992) and Sun et al. (1996). Starting from an initial straight planimetric configuration, slightly and randomly perturbed, the evolution in time of the channel planform configuration is described by the migration of each point of its axis. The channel axis is thus discretized through a sequence of equally spaced nodes $P_i = (x_i, y_i)$ each of them representing a cross-section of the river, identified by the dimensionless streamline coordinate s. At every time step Δt, the planimetric evolution of the channel axis is calculated by displacing each node orthogonally to the channel centerline by an amount $\zeta_i \Delta t$:

$$\begin{cases} x_i(t + \Delta t) = x_i(t) - \zeta_i \Delta t \cos\theta_i \\ y_i(t + \Delta t) = y_i(t) + \zeta_i \Delta t \sin\theta_i \end{cases} \tag{3.1}$$

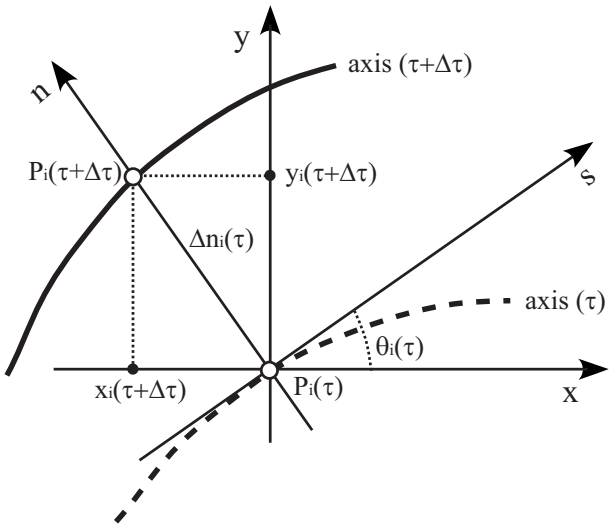

Figure 3.1: Sketch of the displacement that, at every time step, characterizes each points of the channel axis.

where ζ_i is the local lateral migration rate evaluated, after the computation of the near-bank velocity perturbation U_b (see Section 3.3), through equation (2.3).

The very slow time scale associated with the planimetric development of the channel is described in terms of the slow temporal variable $\tau = Et$, thus equation (3.1) reduce as follows:

$$\Delta n_i = \hat{\zeta}_i \Delta\tau \tag{3.2}$$

where Δn_i is the orthogonal displacement of the i-th cross-section and $\hat{\zeta} = \zeta/E$ is the normalized lateral migration rate (Figure 3.1). In our simulations, a constant erodibility coefficient E is assumed (say 10^{-8}) as a first approximation, thus neglecting the different erodibility characterizing the undisturbed floodplain, the point bar deposits and the oxbow lakes.

In order to improve the accuracy and efficiency of computation, a time marching predictor-corrector method (Crosato 1990) is used. The forward time step is performed using for each node the normalized migration rate obtained by averaging its values at the previous and present time steps:

$$\Delta n_i(\tau)_c = \frac{\Delta\tau}{2}\left[\hat{\zeta}_i(\tau) + \hat{\zeta}_i(\tau - \Delta\tau)\right] \tag{3.3}$$

where $\Delta n_i(\tau)_c$ is the corrected bank erosion rate of the i-th cross-section at time τ. The amplitude of the step size $\Delta\tau$ is controlled by requiring that

$$\Delta\tau \leq \epsilon \frac{\Delta s_{max}}{(\partial n/\partial\tau)_{max}} \tag{3.4}$$

where Δs is the distance between two consecutive nodes, $(\partial n/\partial\tau)_{max}$ is the maximum bank erosion speed, and ϵ is an empirical parameter defining the threshold between stable and unstable computations. The form of (3.4) is similar to the relation used by Courant et al. [1952] for the stability of explicit numerical schemes for computation of riverbed deformations. In this particular case, the celerity of propagation of an infinitesimal bed perturbation id replaced by the celerity of river migration $(\partial n/\partial\tau)$. Recalling the erosion law (2.3) we can set

$$\partial n/\partial\tau = \hat{\zeta} = U_b \tag{3.5}$$

and substituting (3.5) in (3.4) we get:

$$\Delta\tau \leq \epsilon \frac{\Delta s}{(U_b)_{max}} \tag{3.6}$$

where $(U_b)_{max}$ is the maximum value of the near-bank velocity increment of the perturbed flow, evaluated along the entire reach. The choice of the value of the parameter ϵ $(= 0.01)$ was made through suitable simulation tests, considering a balance between computational effort and accuracy of the numerical solution.

As the channel migrates, the distance Δs between individual nodes may increase or decrease. A standard cubic spline interpolation was used to remesh the points uniformly after each time step. Moreover, new nodes were periodically added to maintain the size of the spatial step in the range $0.8 - 0.9$. This interpolating procedure turned out to be very useful especially in the regions of high curvature (such as those formed by cutoffs) to ensure curve smoothness and, as a consequence, to prevent numerically spurious oscillations.

The ceaseless elongation/shortening of the channel intrinsic length causes a gradual reduction/increase of down-channel slope. As a consequence, assuming a constant formative bankfull discharge and a temporally constant valley gradient, the governing dimensionless parameters β, d_s and τ_* vary with time according to the relationships

$$\begin{aligned} \beta(\tau) &= \beta_0 \left(\sigma_T(\tau)^{-1} \frac{C_{f_0}}{C_f(\tau)} \right)^{1/3} \\ \tau_*(\tau) &= \tau_{*_0} \left(\sigma_T(\tau)^{-1} \right)^{2/3} \left(\frac{C_{f_0}}{C_f(\tau)} \right)^{-1/3} \\ d_s(\tau) &= d_{s_0} \left(\sigma_T(\tau)^{-1} \frac{C_{f_0}}{C_f(\tau)} \right)^{1/3} \end{aligned} \tag{3.7}$$

The temporal evolution of the relevant parameters then depends on their initial values (β_0, d_{s_0}, τ_{*_0}) and on the evolution of channel tortuosity $\sigma_T(\tau)$ (i.e., the ratio of channel length to valley length) and channel friction C_f. Figure 3.2a,b shows a typical example of the time evolution of channel tortuosity σ_T and its related aspect ratio β until incipient cutoff conditions are reached. The progressive elongation/shortening of channel intrinsic length causes a variation not only of the aspect ratio β, but also of its resonant value β_r, which, as explained in Chapter 2, is a function of the intensity of sediment transport and of flow resistance. This fact may drive the crossing of resonant conditions (Figure 3.2c,d) during a given run. The morphodynamic issues associated with this phenomenon are discussed in Chapter 4.

3.3 Computation of local erosion rate

As already mentioned, on the large time-scale characterizing the channel migration the local erosion rate ζ is assumed to dependent parametrically on the near bank velocity increment U_b and, hence, it requires the computation of both the local channel axis curvature and some convolution integrals involving it (see equations 2.6 and 2.7). At each time step, the computation of ζ then consists of the following steps.

Given the planform configuration, the spatial distribution of the angle $\theta(s)$, formed by the local tangent to the channel axis and the direction of a generic Cartesian axis of

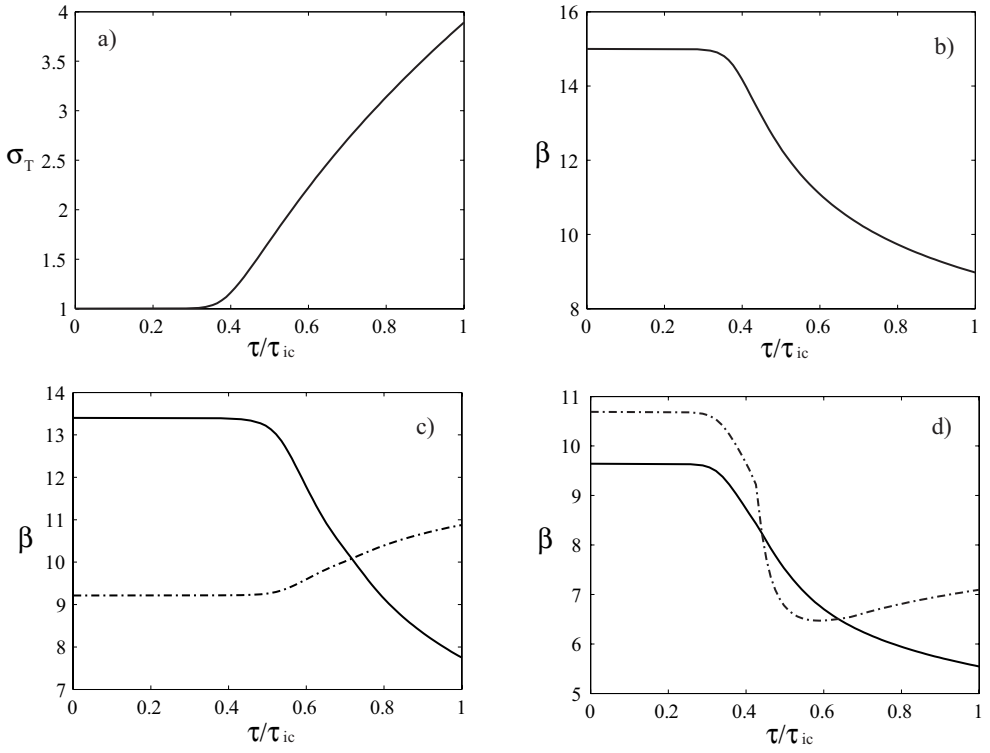

Figure 3.2: Typical examples of time evolution of (a) channel tortuosity σ_T and (b) aspect ratio β until incipient cutoff conditions (ZS model). The initial values of the parameter used in the simulation are: $\beta = 15$, $d_s = 0.01$, $\tau_* = 0.15$, plane bed. c),d) Time evolution of the aspect ratio β (dash-dotted line) and of its resonant value β_r (dash-dotted line). c) Transition from super to sub-resonant regime. The initial values of the parameter used in the simulation are: $\beta = 13.4$, $d_s = 0.05$, $\tau_* = 0.7$, dune covered bed. d) Double transition in the morphodynamic regime: from sub to super-resonant and then from super to sub-resonant conditions. The initial values of the parameter used in the simulation are: $\beta = 9.64$, $d_s = 0.027$, $\tau_* = 0.076$, plane bed. In all cases the Parker bedload formula has been adopted.

reference, is obtained by averaging back and forth according to the following relationship [Seminara et al., 2001]:

$$\theta_i = \frac{1}{2}\left(\arctan\frac{y_{i+1}-y_i}{x_{i+1}-x_i} + \arctan\frac{y_i-y_{i-1}}{x_i-x_{i-1}}\right) \tag{3.8}$$

The local value of dimensionless channel curvature $\mathcal{C}$ is then readily determined from the geometrical relationship:

$$\mathcal{C}(s) = -\frac{1}{\nu_0}\frac{\partial\theta}{\partial s} \tag{3.9}$$

Central differences are used to calculate the s derivatives of θ, except at the upstream and downstream boundaries, where forward and backward differences are employed, respectively. This procedure turns out to give a quite robust estimate of the curvature series limiting as much as possible numerical errors which could locally arise in the curvature series when resonant condition are crossed (see Chapter 4) or after the occurrence of a cutoff event. In any case, the local value of the curvature is periodically monitored by using a Savitzky-Golay smoothing filter.

The convolution integrals which appear in both (2.6) and (2.7) are next evaluated. In order to significantly reduce the computational effort required by these integrals, the integration is performed using a semi-analytical approach, based on the assumption that the curvature varies linearly between two consecutive nodes. Moreover, taking advantage of the fact that the functions to be integrated decays exponentially, the integration is truncated when the function is smaller than a given tolerance (say 0.0001), with a further significant reduction of the computational time.

Once the distribution of channel axis curvature and the convolution integrals are known, the local erosion rate $\zeta(s)$ is evaluated by employing equation (2.3).

3.4 Beyond cutoff: modelling of channel shortening

On long time scales typical of river meander evolution, the features of planimetric patterns are further complicated by the occurrence of cutoff processes (see Figures 1.8 and 3.3).

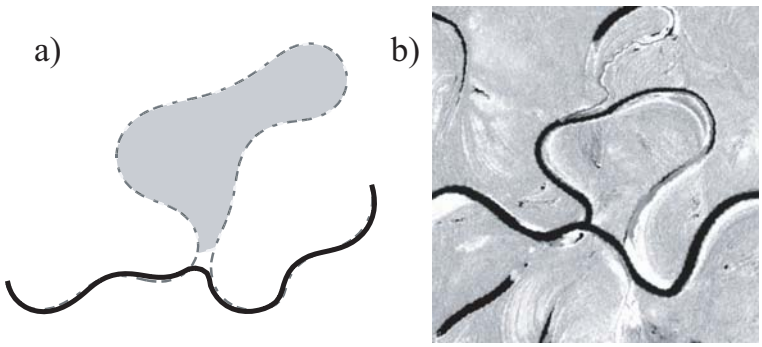

Figure 3.3: Examples of channel shortening via neck cutoff process. a) Numerical simulation (ZS model). b) Natural river located in Brazil (Juruá river, from *http* : *//glcfapp.umiacs.umd.edu/* web site). Flow is from left to right.

In fact, the abrupt channel shortening associated with cutoff produces strong nonlinear interactions which add up to geometric nonlinearities related to equation (2.1) and, although neglected here, to flow field nonlinearities. Obviously, external controls (e.g., flow variability, spatio-temporal heterogeneity of flood plain and bank characteristics, geological processes, human interference) also contribute to the nonlinear shaping of meander bends [Hooke, 2007] but, as we will see (Chapter 4), they are not strictly necessary to reproduce the main features of the patterns observed in nature.

Two different types of cutoff are usually recognized in natural channels, i.e., chute and neck cutoffs. Chute cutoffs are relatively long flow diversions which occur when a meander loop is bypassed through a new channel which forms across the bar enclosed by the loop. They most frequently form in wide channels with large curvature bends, high discharges, poorly cohesive, weakly vegetated banks, and high gradients [Howard and Knutson, 1984], and their prediction is a yet unresolved problem. In the present contribution we thus focus our attention only on neck cutoff processes (see Figure 3.3), which characterize the long-term development of highly sinuous meandering rivers. This kind of cutoff occurs when the local sinuosity becomes so large that adjacent loops intersect each other, leading to the formation of an abandoned loop (oxbow lake) when sedimentation closes the ends of the former loop.

Following Howard and Knutson [1984] and Sun et al. [1996], the presence of potential

neck cutoffs is detected by controlling whether the distance between the i-thnode P_i and a given node P_{i+k} (not immediately upstream or downstream of P_i) approaches some critical distance (say $2.2B_0^*$). When such a distance is reached, all the points $P_{i+j},\ j = 1, k$, representing the abandoned channel loop, are removed. To recognize the nodes closer than the selected critical distance we used the matrix algorithm described by Camporeale et al. [2005], which ensures a significant reduction of the computational effort. Furthermore, in order to avoid the presence of physically nonrealistic cusp-like regions with very high curvature at a reconnection, we chose to remove also a few nodes upstream and downstream of P_i and P_{i+k}, respectively (see Figure 3.4a). This somehow artificial procedure is justified by the fact that, in meandering rivers, the rapid smoothing of sharp bends through neck cutoff is a well-known process [Hooke, 1995] (see also Figures 3.3b and 3.4b).

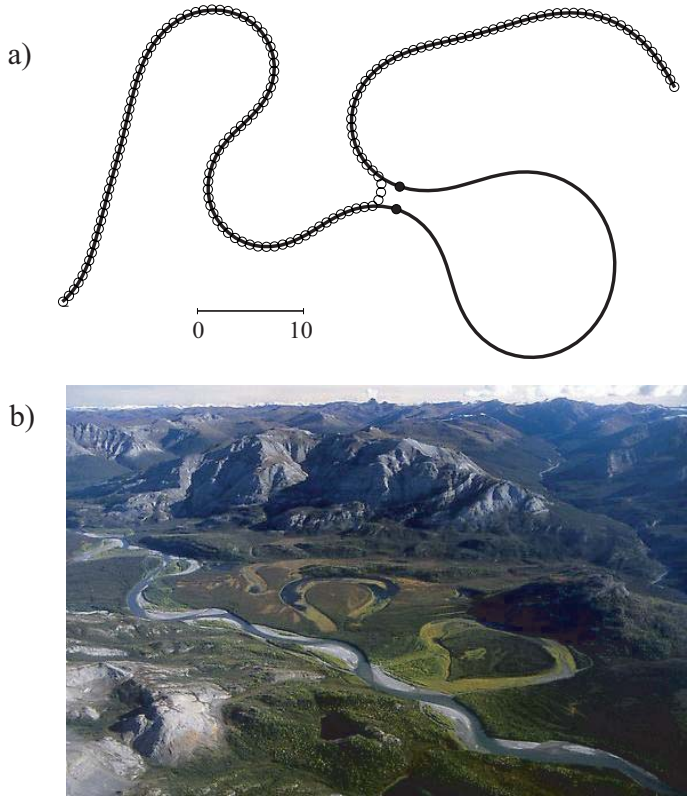

Figure 3.4: a) Modelling of neck cutoff process (ZS model, flow is from left to right). Black circles indicate the points were the critical threshold is approached. Some other points are removed in order to avoid the presence of unrealistic cusp-like regions. b) Two examples of real neck cutoffs and relative oxbow lakes. Alatna River, Alaska, USA.

Chapter 4

Morphodynamic regime and long term evolution of meandering rivers

4.1 Introduction

On the short timescale characterizing meander evolution before cutoff, theoretical models proved able to reproduce many of the morphologic and dynamic features of planimetric patterns observed in nature. In the absence of geological constraints (like valley confinement), it has been demonstrated that meanders of permanent form cannot migrate in the longitudinal direction without displaying any growth or decay [Parker et al., 1983; Parker and Andrews, 1986, Seminara et al. 2001]. The curves proposed by Langbein and Leopold [1966] and by Kinoshita [1961] to describe the planimetric pattern of meanders, rather than purely empirical correlations, turned out to be the leading and second order approximations of the exact solution of a suitable planimetric evolution equation [Seminara et al. 2001]. A general consent also exists that, on short time scales, the computed planimetric forms crucially depend on the ability of a given flow field model to account for the resonance phenomenon [Lanzoni et al. 2006; Camporeale et al. 2007]. For example, the formation of multi lobed meander loops (see Figure 4.1) before incipient cutoff conditions was found to be favored by the growth of harmonics higher than the third, which is enhanced near resonant conditions [Seminara et al. 2001, Sun et al., 2001].

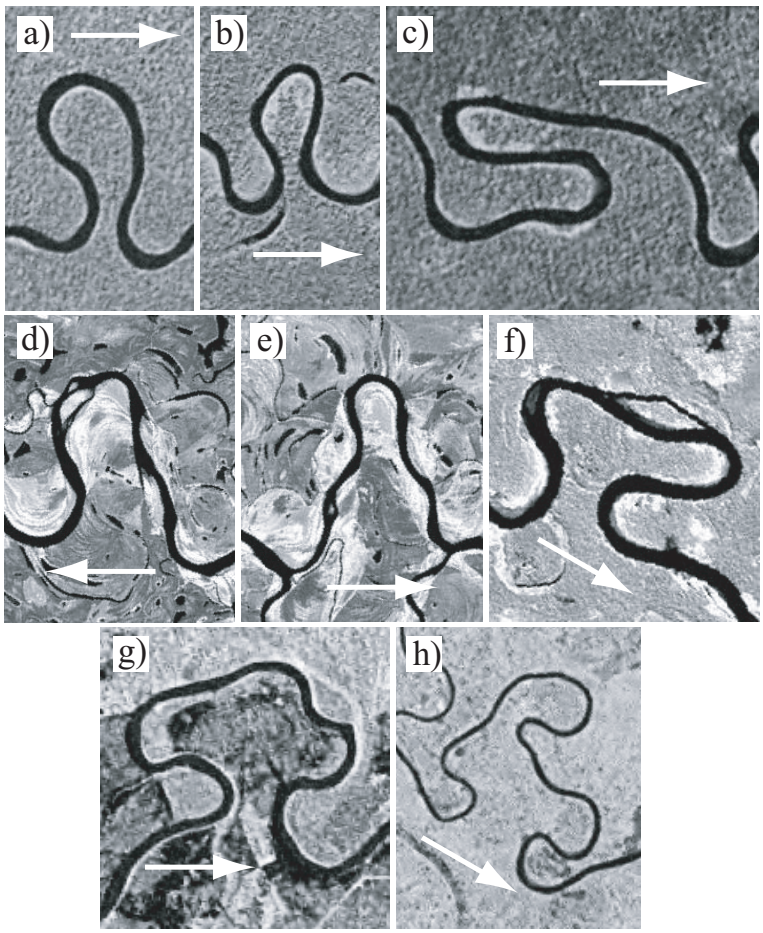

Figure 4.1: Examples of the shapes of meandering bends usually observed in nature. a) Downstream and b) upstream skewed bends; c), d), e) and f) compound bends; g)and h) multiple loop. The river locations are: a),b),c) northern Papua New Guinea; d),e) Alaska (Porcupine River); f) Peru (Rio Madre de Dios); g) western Canada; h) Peru. The images have been obtained from the Landsat mosaic image web sites: a),b),c),g),h), *https* : *//zulu.ssc.nasa.gov/mrsid/* web site; d),e),f), *http* : *//glcfapp.umiacs.umd.edu/*. The arrows indicate flow direction.

Mathematical models have been widely used also for the study of the long term evolution of meandering streams, that is after the repeated occurrence of cutoffs has substantially altered the geometry of the channel axis [e.g., Ferguson, 1976; Howard, 1992, 1996; Sun et al., 1996]. Indeed, numerical simulations allow for a wide exploration of the variations in physical process assumptions, in boundary conditions, and in initial conditions,whereas the field study of meandering channel dynamics at historical timescales is typically complicated by the absence of homogeneous reaches of sufficient length, by the deficiency of historical time records and by the interplay of inherent dynamics of the river and changes in external controls [Hooke, 2007]. On the other hand, mathematical models are necessarily based on a simplified description of process laws and of external controls, owing to the constraints placed by the the long-time intervals and the large spatial scales to be investigated. The question then arises of assessing how much long term, synthetically generated patterns reproduce the morphological features observed in the field. Howard and Hemberger [1991], using multivariate statistical methods, showed that, despite visual similarities, long-term meander planforms generated by numerical models can be statistically distinguishable from natural meanders. Possible reasons for the observed morphometric differences were found in bank erodibility heterogeneities, usually characterizing real rivers, and in the inability of the adopted models to reproduce correctly the formation of compound bends evolving from simple bends through the development of a curvature reversal [Howard, 1992; Sun et al., 1996; Lancaster and Bras, 2002]. Recently, Camporeale et al. [2005, 2008], comparing the results of different numerical models suggested that cutoffs not only provide a statistical equilibrium to meandering rivers, limiting the growth of sinuosity [Stolum, 1996], but also exert a filtering action, preventing several fluid dynamics mechanisms that are important in the short-term from exerting a significant role in the long-term meandering dynamics. In particular, the reduction of planform complexity (generated by meander elongation through bend erosion) was associated with the tendency of cutoffs to remove older meanders. Camporeale et al. [2005] also suggested that the overall complexity of the equilibrium state becomes essentially regulated by only one spatial scale, namely a length of purely hydrodynamic

origin, emerging from the simplified hydrodynamic model of Ikeda et al. [1981], as firstly recognized by Parker and Johannenson [1989] and subsequently reconsidered by Edwards and Smith [2002].

In this chapter we are interested to investigate whether the inspiring findings of Camporeale et al. [2005] also apply to channels evolving under super-resonant conditions or changing morphodynamic regime during their evolution. The analysis of Camporeale et al. [2005], in fact, was carried out by considering only sub-resonant conditions, which we know to represent only one of the morphologic regimes which can be experienced by alluvial rivers. The issue becomes particularly remarkable in the light of the analyses recently carried out by Zolezzi et al. [2008] on a wide data set of single-thread, gravel bed meandering rivers, indicating that the occurrence in the field of super-resonant conditions is not so uncommon, and transitions from one regime to another (most frequently from super- to sub-resonant) are to be often expected during the evolution of natural reaches. The questions we want to answer then are: To what extent does the morphodynamic regime (either super- or sub-resonant) influence, on the long term, the geometrical features of synthetically generated patterns? In particular, do the most advanced numerical models reproduce the formation of compound bends and cumuliform shapes (Figure 4.1), often observed in nature, without invoking external heterogeneities? And, in order to make a comparison with the real word, which statistics must be considered to objectively evaluate the differences/similarities of different patterns? Finally, does a unique spatial scale emerge also when considering the whole range of morphodynamic conditions?

4.2 Analysis of long-term planforms

4.2.1 Morphologic Features of Computed Patterns

Starting from an initial straight planimetric configuration, slightly and randomly perturbed, we have simulated the long term planform evolution of meandering rivers using both the ZS and the IPS linearized flow field models. Sub-resonant and super-resonant regimes, as well as plane and dune covered bed conditions, have been investigated. In

all cases, no constraints on channel migration have been imposed at either channel ends [see Lanzoni and Seminara, 2006]. We also recall that, since we were interested in understanding the ability of mathematical models to describe natural forms without invoking changes in external controls, we assumed a constant formative bankfull discharge yielding, at the beginning of each runs, the values of the relevant parameters β, d_s, τ_*, reported in Table 4.1. Moreover, as already mentioned, a temporally constant valley gradient was also assumed during a given simulation. Furthermore, the total time of each simulation was set large enough to ensure the achievement of statistically steady conditions. The total time of simulation, normalized by the time at which incipient cutoff condition occurred and averaged over IPS and ZS simulations, is reported in Table 4.1.

Figure 4.2 reports a summary of the typical patterns resulting from computations carried out with the ZS model. Visual comparison with the bend forms depicted in Figure 4.1 shows that the entire range of bend geometries observed in nature, namely simple bends (upstream or downstream skewed), compound bends, and multiple loops can be correctly generated by the model. Particularly remarkable is the ability of the model to reproduce the formation, often observed in nature [e.g., Brice, 1974; Hooke and Harvey, 1983], of a compound bend evolving from a simple bend which develops a curvature reversal along the bend itself. Figure 4.3 shows how this ability is strictly related to the transition from super to sub-resonant conditions. As described in Chapter 3, the ceaseless elongation/shortening of channel intrinsic length causes a variation not only of the aspect ratio β, but also of its resonant value β_r, and this fact may produce a change in morphodynamic influence, as depicted in Figure 4.3b. These results indicate that the formation of compound bends does not necessarily need the locking of the system (owing to a neck cutoff event) near resonant conditions, as suggested by previous numerical analysis [Sun et al., 2001; Seminara et al., 2001]. Similarly, heterogeneity of bank erodibility, invoked by Sun et al. [1996] to explain multiple loops (i.e., the cumuliform shapes observed by Howard [1992]), is not strictly needed to reproduce these bend forms, although it surely helps to determine the actual meandering shapes. As far as the the much more simplified IPS model is concerned, numerical simulations show that it does not simulate

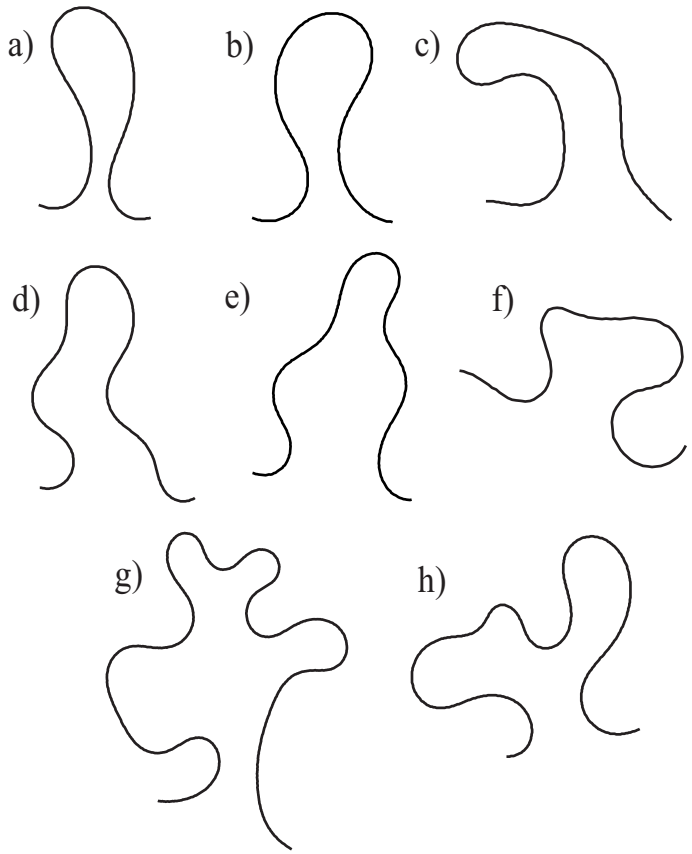

Figure 4.2: Examples of the shapes of meandering bends generated synthetically using the ZS linearized flow field. a) Downstream skewed bend; b) upstream skewed bend; c), d), e), f) compound bends; g),h) multiple loops. The flow is from left to right. [Frascati and Lanzoni, 2009]

the formation of downstream skewed bends, in accordance with the fact that it is unable to reproduce resonance and, hence, super-resonant conditions. Moreover, compound bends and multiple loops can be generated only by repeated cutoffs.

4.2.2 Comparison with natural patterns

In order to objectively test the ability of mathematical models to reproduce the long term dynamics of river meandering we can pursue either a kinematic or a static comparison. Although the former approach is potentially effective, it however requires a set of information not easily available. Indeed, systematic monitoring at historical timescales of the

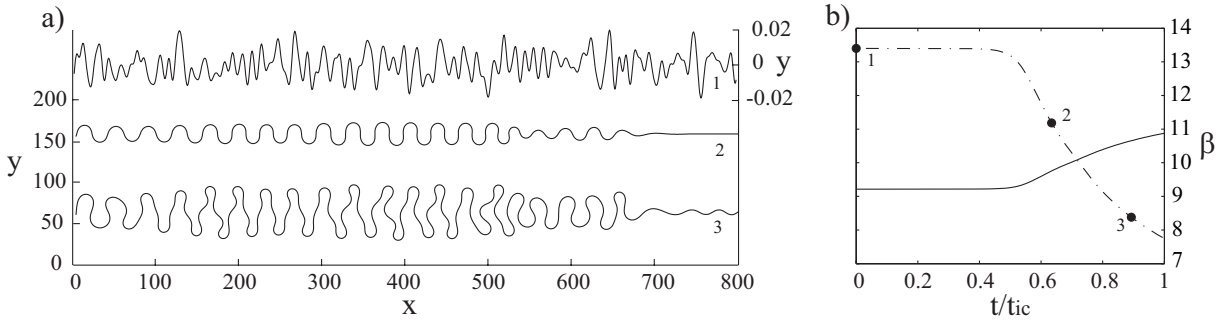

Figure 4.3: a) Typical example of the planform channel evolution, until incipient cutoff condition, starting from a straight planar configuration, slightly and randomly perturbed (configuration 1). b) Time evolution of the aspect ratio β (dashed line) and of its resonant value β_r (solid line). The ceaseless elongation/shortening of the channel intrinsic length causes a variation of resonant conditions and this fact may produce a change in morphodynamic influence. Here is reported the case of a transition from super (configurations 1 and 2, $\beta > \beta_r$) to sub-resonant (configuration 3, $\beta < \beta_r$) conditions with formation of compound bends and disappearance of the downstream straight reach. The initial values of the parameter used in the simulation are: $\beta = 13.4$, $d_s = 0.005$, $\tau_* = 0.7$, dune covered bed. t_{ic} denotes the time at incipient cutoff condition. [Frascati and Lanzoni, 2009]

planar evolution of long enough river reaches [e.g., Hooke, 1995; Gautier et al., 2007] is, in general, not accompanied by other key data required by numerical models, concerning detailed information on upstream and downstream boundary conditions, hydraulic conditions, sedimentological properties of the investigated stream and of the surrounding floodplain, and information on possible hydrological changes. On the other hand, static comparison between different planform configurations has the advantage to point out the deficiencies in mathematical models by simply exploring the range of values which can be attained by the relevant parameters. The richness of meandering geometries, however, has to be measured properly in order to emphasize the subtle differences which can emerge between apparently similar configurations. In this thesis, a static comparison has been pursued by considering fifteen real river reaches with likely minimal anthropic perturbations (see Table 4.2). In particular, the selected set of rivers has been chosen on the basis of data available in literature and also trying to include as much as possible

different environmental and geological contexts (e.g, Amazonia, North America, Papua New Guinea).

Various criteria have been so far proposed to achieve static characterization of meandering patterns [Howard and Hemberger, 1991; Andrle, 1996; Lancaster and Bras, 2002]. Here, following the multivariate approach developed by Howard and Hemberger [1991], we set up a suite of twelve morphometric variables able to distinguish between natural and modelled channels. These variables are summarized in Table 4.3, and can be sorted out into four groups. The first includes quantities concerning the sinuosity, referred either to the entire reach under investigation or to single meanders (or half-meanders). They are: the total sinuosity (tortuosity) σ_T, the half-meander average sinuosity σ_H, and the full-meander average sinuosity σ_F, defined by the following relationships:

$$\sigma_T = \frac{\sum L_i}{L_T} \quad \sigma_H = \frac{1}{N}\sum \frac{L_i}{\ell_i} \quad \sigma_F = \frac{1}{M}\sum \frac{L_{fi}}{\ell_{fi}} \tag{4.1}$$

where, as shown in Figure 4.4a, L_T is the cartesian distance between the initial and the final points of the investigated planform configuration, L_i (L_{fi}) is the half-meander (full meander) intrinsic wavelength, ℓ_i (ℓ_{fi}) is the half meander (full meander) cartesian wavelength, and N (M) is the total number of half-meanders (full meanders). The second group of variables concerns the distribution along the reach of the cartesian half-meander wavelength and includes the mean (ℓ_{av}), the variance (ℓ_{va}), the skewness (ℓ_{sk}) and the kurtosis (ℓ_{kr}) of ℓ_i. The third group of statistics consists of the variance ($\mathcal{C}_{var}$) and the kurtosis ($\mathcal{C}_{kr}$) of the the spatial distribution of the local channel axis curvature. This group does not include the mean ($\mathcal{C}_{av}$) and the skewness ($\mathcal{C}_{sk}$) of $\mathcal{C}$ in order to avoid redundancy of information. Indeed, the analysis carried out by Howard and Hemberger [1991] indicates that $\mathcal{C}_{av}$ and $\mathcal{C}_{sk}$ are not really able to discriminate between different patterns. Finally, the fourth group of morphometric parameters measures the tendency of meanders to be asymmetrical by considering the asymmetry index [Howard and Hemberger, 1991]:

$$\mathcal{A} = \frac{L^u - L^d}{L} \tag{4.2}$$

where L^u and L^d are the intrinsic lengths of the channel axis upstream and downstream

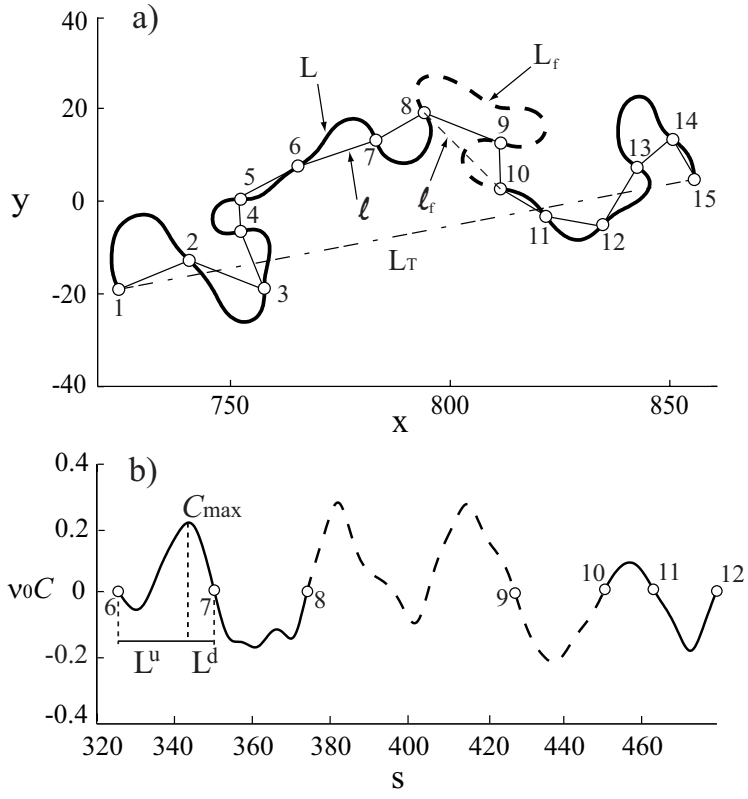

Figure 4.4: a) Planimetric pattern of channel centerline showing: the inflection points (solid dots), the half-meanders (full meanders) intrinsic L (L_f) and cartesian ℓ (ℓ_f) wavelengths, and the straight distance, L_T, between the initial and final inflection point of the investigated reach. The portion of channel axis denoted by a dashed line shows a typical example of multiple loop. b) Spatial distribution of the corresponding local curvature $\nu_0\mathcal{C}$ [Frascati and Lanzoni, 2009].

the locus of maximum curvature C_{max} along the half-meander (see Figure 4.4b). The parameter $\mathcal{A}$, which can take values between -1 and +1, determines whether half-meanders are upstream ($\mathcal{A}$<0) or downstream skewed ($\mathcal{A}$>0), and therefore can be of some help in discriminating between downstream and upstream morphodynamic influence, as it will be discussed later on. In order to objectively quantify the morphodynamic regime prevailing in the analyzed reaches, we then consider the reach averaged asymmetry coefficient $\mathcal{A}_{av}$, its kurtosis $\mathcal{A}_{kr}$, and the 60-90 length percentile $\mathcal{A}_{60-90}$.

The selected suite of statistics has been analyzed through Principal Component Analysis (PCA), a decomposition technique commonly adopted for recognizing patterns in

data sets [see Lay, 2000]. This methodology, which allows one to reduce a complex data set to a lower dimension, emphasizing the role of the most relevant parameters, can be briefly summarized as follows. Let $\mathbf{P} = [\mathbf{p}_1\mathbf{p}_2...\mathbf{p}_M]$ the NxM data matrix, where the components of vector $\mathbf{p}_j$ (j=1,M) represents the sampled values of the N (= 12 in our case) statistics related to the j-th planform configuration. We first create a new data set matrix $\mathbf{Q} = [\mathbf{q}_1\mathbf{q}_2...\mathbf{q}_M]$ whose elements are obtained from $\mathbf{P}$ elements by the relationship:

$$q_{ij} = \frac{p_{ij} - \mu_i}{\delta_i} \qquad (i = 1, N; j = 1, M) \tag{4.3}$$

where μ_i and δ_i are the mean and the standard deviation of the i-th row of $\mathbf{P}$, respectively. The operation (4.3) produces a standardized data set with zero mean and unit standard deviation. We next compute the square sample covariance matrix $\mathbf{Z}$ and its eigenvalues ($\varphi_1 > \varphi_2 > ... > \varphi_N$) and eigenvectors ($\mathbf{e}_1, \mathbf{e}_2, ..., \mathbf{e}_N$). The eigenvector $\mathbf{e}_1$ with the highest eigenvalue (φ_1) represents the first principal component of the data set, the eigenvector $\mathbf{e}_2$ associated with the second highest eigenvalue is the second principal component, and so on. Hence, the full set of principal components is as large as the original set of variables. Since $\mathbf{Z}$ is symmetric, all the principal components are orthogonal to each others and any vector column $\mathbf{q}_j$ can be written as a linear combination:

$$\mathbf{q}_j = \sum_{i=1}^{N} a_{ij}\, \mathbf{e}_i \qquad (j = 1, M) \tag{4.4}$$

Observing that the percent of total variability associated with each principal component decreases progressively from the first to the N-th principal component, it is possible to neglect the components of lesser significance (i.e., associated with smaller eigenvalues). Keeping only the term corresponding to the K largest eigenvalue we finally obtain the reduced matrix $\hat{\mathbf{Q}}$ with components:

$$\hat{\mathbf{q}}_j = \sum_{i=1}^{K} a_{ij}\, \mathbf{e}_i \qquad (K < N; j = 1, M) \tag{4.5}$$

where $\mathbf{a}_j = (a_{1j}a_{2j}...a_{kj})^T$ is the representation of $\hat{\mathbf{q}}_j$ in the principal component basis $(\mathbf{e}_1, \mathbf{e}_2, ..., \mathbf{e}_K)$.

In the specific case treated here the first two principal components, $\mathbf{e}_1$, $\mathbf{e}_2$, account for about 62% of the total variance of the original data. The scatter plot of their coefficients a_1,a_2, displayed in Figure 4.5a, indicates that the ensemble of morphological variables here considered can discriminate among different meandering patterns. First of all, it turns out that the simplified description of the physical processes embodied by the IPS model does not reproduce correctly the overall geometrical characteristics observed in nature. The cluster of points resulting from IPS simulations and those referring to natural stream, in fact, does not overlap at all. Some differences are also observable between IPS and ZS planforms under sub-resonant conditions. A certain overlapping with observed patterns is on the contrary attained when considering the ZS planforms simulated under super-resonant conditions. This result is extremely encouraging, also in consideration of the simplifications embodied by the ZS model and of the fact that present simulations do not account for changes in external controls (e.g., discharge intermittency, floodplain inhomogeneities, vegetation effects). The scatter plot of Figure 4.5a also points out that it is essentially the coefficient a_1 which discriminates among the various patterns.

Some information on the causes of similarities/differences intrinsic to the various planforms can be gathered from Figure 4.5b, describing the contribution to the first two principal coefficients provided by each morphological variable of the original set. As already pointed out by Howard and Hemberger [1991], and Howard [1992], natural rivers tend to have less sinuous half and full meander (i.e., smaller σ_F, σ_H) and smaller overall sinuosity (σ_T). This result is not surprising if we recall that the occurrence of chute cutoff has not been considered in the present simulations. Indeed, the formation of these longer flow diversions has been demonstrated to be able to produce also in simulated patterns a degree of sinuosity resembling natural landforms [Howard, 1996]. A clear difference between natural and simulated patterns disclosed by Figure 4.5b is related to the degree of asymmetry. IPS patterns turn out exaggeratedly upstream skewed, whereas natural streams are characterized by a nearly vanishing asymmetry or, like ZS super-resonant planforms, are skewed downstream, thus leading to a negative weighting of $\mathcal{A}_{av}$ and $\mathcal{A}_{60-90}$. A possible explanation of this latter result, in accordance with the analysis carried out by Zolezzi

et al. [2008], is that transitions from one morphodynamic regime to another (most frequently from super- to sub-resonant) are to be often expected during the evolution of natural reaches. This implies the presence along a given reach of both upstream skewed and downstream skewed bends which leads to a relatively small value of $\mathcal{A}_{av}$. We must however point out that the formation of almost symmetric or downstream skewed meanders can be also related to the role played on meander migration by heterogeneities in floodplain erodibility associated, for example, with the interplay between river morphology and vegetation dynamics [Perrucca et al., 2007]. The role played by half-meander and curvature statistics is less clear, as also emerges from Table 4.4, reporting the mean value of the morphological variables calculated for each type of patterns. In general, natural rivers and ZS super-resonant planforms tend to have similar values of ℓ_{av}, ℓ_{va}, ℓ_{sk} and $\mathcal{C}_{va}$. IPS configurations exhibit values of ℓ_{av}, ℓ_{va}, ℓ_{kr} and $\mathcal{C}_{kr}$ higher that those observed in the field. Finally, ZS super-resonant planforms are characterized by mean values of the morphologic parameters that are intermediate between those of ZS sub-resonant configurations and those typical of natural forms.

4.3 Morphodynamic signatures and action of cutoff

The analysis carried out so far suggest that the better performance of the ZS model in reproducing the geometric features of observed patterns is related to its ability to account for the entire range of morphodynamic regimes. In particular, we have seen that the transitions from super- to sub-resonant conditions can generate compound bends even before incipient cutoff. On the other hand, the analysis put forward by Camporeale et al. [2005] suggests that the statistically steady state attained as a consequence of the filtering action exerted by repeated cutoff events is independent of the morphodynamic model adopted in the simulations. These apparently contrasting results can be explained by recalling that Camporeale et al. [2005] considered only sub-resonant conditions, a morphodynamic regime which describes only one aspect of the behaviour of natural streams. Moreover, the results of PCA analysis just discussed indicate that the properties used by Camporeale et al. [2005] to characterize statistically the river geometry, i.e., the local curvature, the

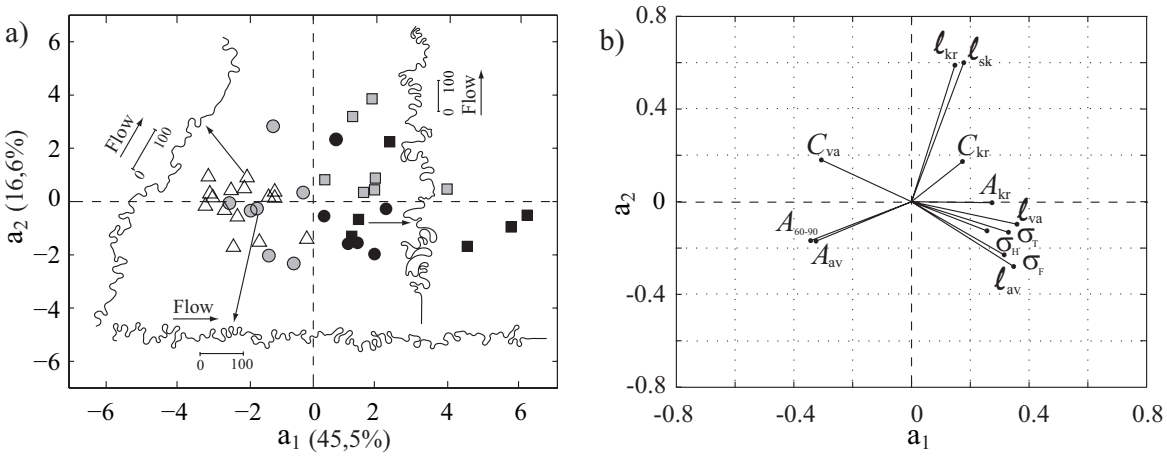

Figure 4.5: a) Scatter plot of the principal component coefficients a_1 and a_2. Symbols are as follows: squares, IPS model; circles, ZS model; triangles, natural rivers. Grey symbols denote super-resonant conditions; black symbol denote sub-resonant conditions. The typical planform configurations also reported in the figure refer to a natural river located in Peru (Rio Madre de Dios), and to two synthetic patterns simulated considering the IPS model (run 3), and the ZS model (run 3). The dimensionless planimetric scale is expressed in half-width units. b) In this plot each of the twelve morphometric variables considered in the analysis is represented by a vector, and the direction and length of the vector indicates how each variable contributes to the two principal components in the plot [Frascati and Lanzoni, 2009].

intrinsic wavelength and the cartesian wavelength, are not sufficient to fully characterize the subtle, but fundamental differences among meandering planform configurations.

The presence of clear morphodynamic signatures even in the long term, i.e., after repeated cutoff events have removed the older reaches from the active river, also giving rise to a shot noise that randomly disturbs (in space and time) the deterministic dynamics and propagates along the river [Camporeale et al., 2008], can be appreciated by considering the morphodynamic length scale $\mathcal{L}_m$ which arises within the context of the ZS model. This scale is associated with the inverse of the imaginary parts of the two complex conjugate exponents λ_{m3} and λ_{m4} appearing into (2.7), and determines the typical length of spatially oscillating disturbances. Figure 4.6b shows that the spatial scale $\mathcal{L}_h$ $(= 1/\lambda_0)$, emerging from the IPS model, can attain values similar to $\mathcal{L}_m$ $(= 1/\lambda_{m3i}, m = 1)$ not only in the sub-

resonant region but also, depending on the values of the relevant parameters, in the lower portion of the super-resonant region. However, the two scales tend to deviate significantly (by a factor larger than 1-2) as the bankfull aspect ratio of the river increases sufficiently above its resonant value. This behavior is related to the fact that $\mathcal{L}_h$ determines the length typically required for a perturbation of the near bank velocity increment U_b to decay and, therefore, is dictated only by curvature-forced variations in velocity and depth. On the other hand, meander dynamics generally depends also on the free response of the sediment bed in terms of alternate bars, accounted for through $\mathcal{L}_m$.

The persistence also in the long term of geometric features intrinsically related to a specific morphodynamic regime is described by Figure 4.7. As already documented by Camporeale et al. [2005], the curvature probability density functions of both IPS and ZS planform configurations, when scaled by $\mathcal{L}_h$, tend to collapse on a common behavior (Figure 4.7a,b). Nevertheless, the scatter exhibited by ZS curves is significantly higher when both the morphodynamic regimes are accounted for. This result is not surprising, in that the hydrodynamic scale $\mathcal{L}_h$ approximates reasonably the actual morphodynamic length scale mainly in the sub-resonant regime (see Figure 4.6b). Conversely, a remarkable collapse on two distinct common behaviours is obtained if $\mathcal{L}_m$ is adopted to scale the pdf of curvature associated with ZS planforms (see Figure 4.7c). The signature of the morphodynamic regime (either sub or super resonant) then persists also in the long term and, therefore, the occurrence of repeated cutoffs is not sufficient to filter out completely the geometrical complexity driven by morphodynamic influence.

The importance of the role played by the morphodynamic length scale $\mathcal{L}_m$ is confirmed by the analysis of the geometric features of oxbow lakes (summarized by the intrinsic length L_o and the area A_o defined in Figure 4.8) formed by neck cutoff processes during the entire channel planform evolution. Figure 4.9 reports the cumulative distribution functions (cdf) of oxbow lakes intrinsic length characterizing IPS (4.9a) and ZS (4.9b) planforms. Again, all the cdf curves deriving from IPS simulations completely merge if scaled by $\mathcal{L}_h$, whereas a remarkable collapse on two distinct common behaviors, corresponding to either sub-resonant or super-resonant conditions, is attained by scaling ZS

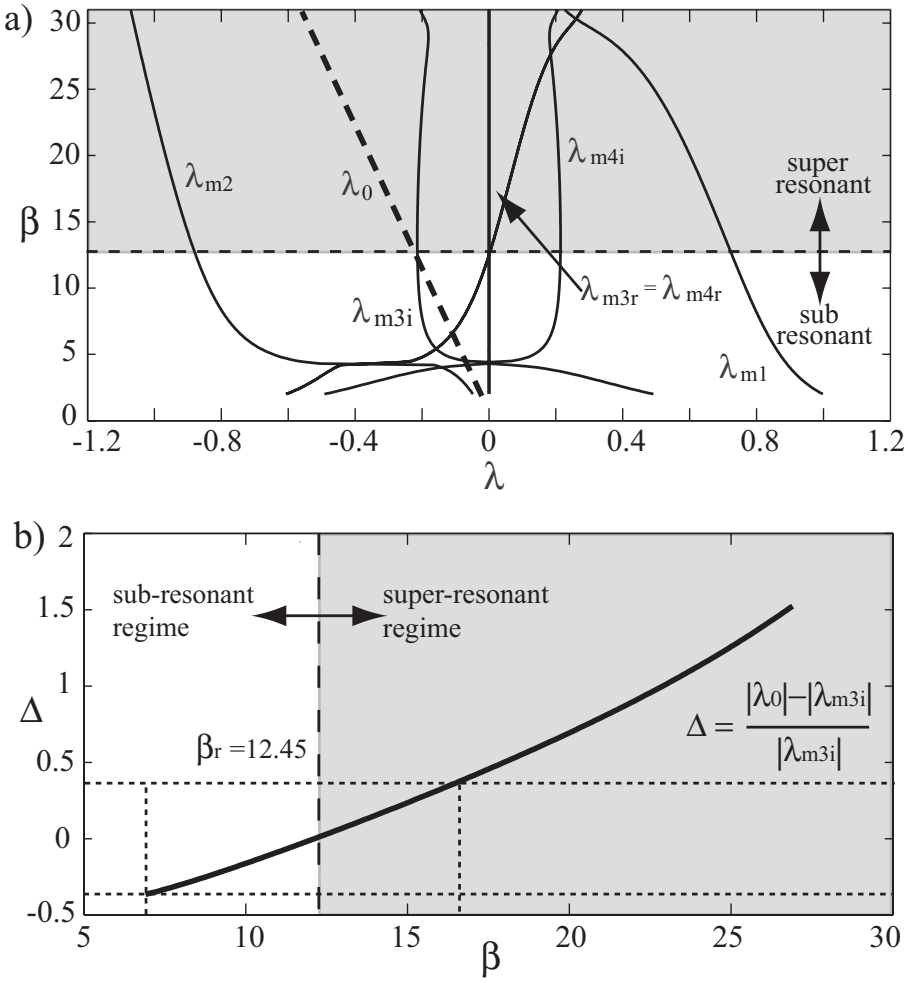

Figure 4.6: a) Typical behavior of the characteristic exponents of the two linearized flow fields models used in the computations: IPS model (dashed line); ZS model ($m = 1$, solid line). b) Plot of the normalized difference Δ between the eigenvalue (λ_0) of the IPS model and the imaginary part of the complex conjugate eigenvalues ($\lambda_{m4i} = -\lambda_{m3i}$) of the ZS model as a function of the aspect ratio β of the channel. The values of the relevant parameters are: $\tau_* = 0.4$, $d_s = 0.001$, dune covered bed [Frascati and Lanzoni, 2009].

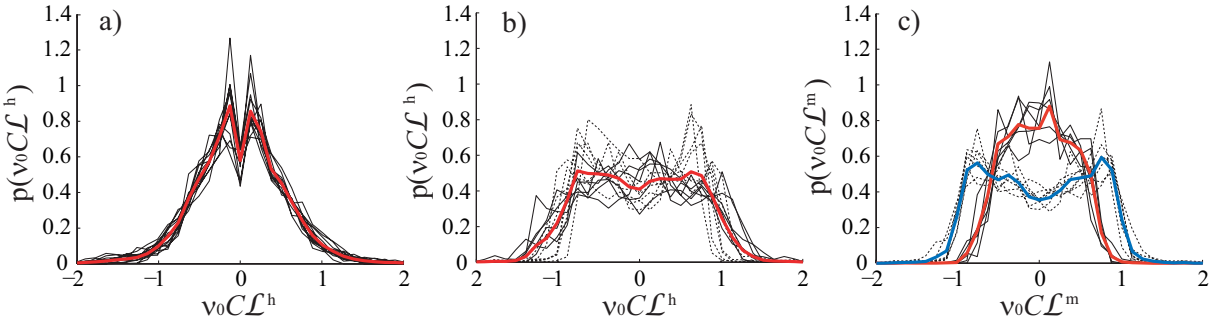

Figure 4.7: Scaling of the probability density function (pdf) of channel axis curvature resulting from different models. a) IPS model, pdfs scaled by $\mathcal{L}_h$; b) ZS model, pdfs scaled by $\mathcal{L}_h$. Solid lines denote sub-resonant conditions whereas dashed lines denote super-resonant conditions. c) ZS model, pdfs scaled by $\mathcal{L}_m$. Once again, solid lines denote sub-resonant conditions and dashed lines denote super-resonant conditions; red and blue lines denote mean pdf distributions [Frascati and Lanzoni, 2009].

cdfs by $\mathcal{L}_m$.

Which conclusions can then be drawn about the long term role of cutoffs? Surely the removal of older, well developed meanders limits the planform geometrical complexity and, consequently, ensures the reaching of statistically steady planform configurations. This systematic elimination action, along with the propagation of the disturbances locally generated by each cutoff event (i.e., the geometric and dynamic mechanisms pointed out by Camporeale et al., 2008) likely smooth out the differences associated with the various level of approximation adopted in modelling curvature-forced circulations. These differences, embodied by the length scales $\mathcal{L}_h$ and $\mathcal{L}_m$, are anyhow relatively limited under sub-resonant conditions, for which $\mathcal{L}_h$ and $\mathcal{L}_m$ get very similar values. In this case, the advantage of resorting to $\mathcal{L}_h$ (defined as the ratio of the depth to the friction factor) consists of the easiness of its estimation. The computation of $\mathcal{L}_m$, in fact, requires the solution of a fourth order algebraic equation whose coefficients are functions of the relevant parameter of the problem (namely the bankfull aspect ratio, the Shields stress of the basic uniform flow and the relative grain roughness) and, hence, is surely less immediate. In any case, the signatures exhibited by different morphodynamic regimes are not removed by the filtering action of cutoffs. In order to catch the long term similarity of different

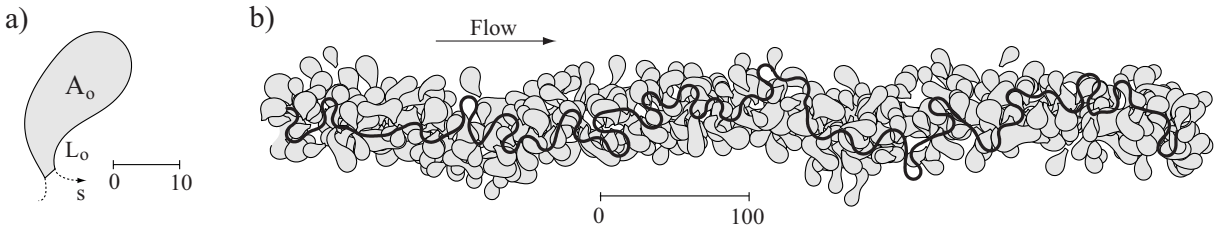

Figure 4.8: Details of a single oxbow lake and notations. b) Typical example of long term planform configuration of a meandering river resulting from the linearized ZS flow field model (run 2). The figure highlights the oxbow lakes (grey lobes) occurring during the entire planimetric evolution. Planimetric dimensionless scales are expressed in half-width units. [Frascati and Lanzoni, 2009]

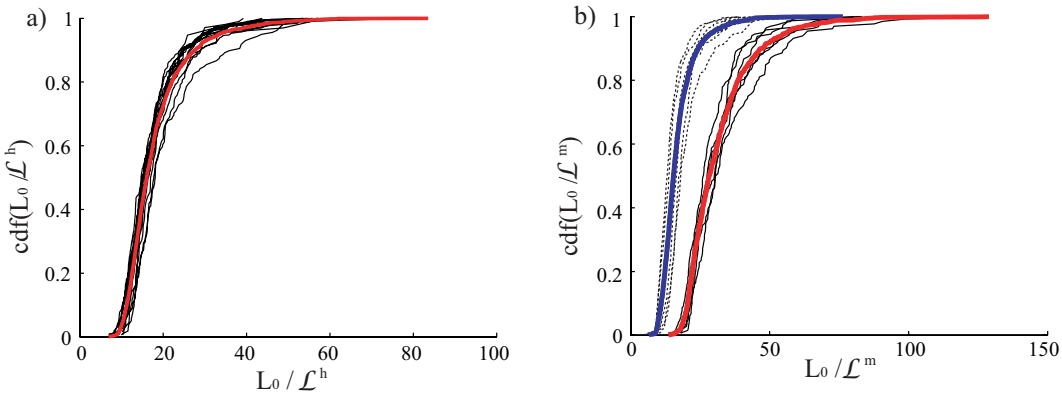

Figure 4.9: Scaling of the cumulative distribution function (cdf) of oxbow lakes intrinsic length resulting from different models. a) IPS model, cdf scaled by $\mathcal{L}_h$. b) ZS model, cdf scaled by $\mathcal{L}_m$. Solid lines denote sub-resonant conditions; dashed lines denote super-resonant conditions; red and blue lines denote mean cdf distributions. [Frascati and Lanzoni, 2009]

planform configurations it is thus necessary to introduce the morphodynamic length scale $\mathcal{L}_m$ which arises only if the free response of the sediment bed in terms of alternate bar perturbations is also considered. For reasonable values of the relevant parameters, the wavelength of these perturbations, falling in a range of about 10-30 channel widths, is very similar to the cartesian wavelength (i.e., the distance between three consecutive inflection points) exhibited by real meanders. The repeated occurrence of cutoffs likely reinforces the selection of this particular length scale which, strictly speaking, arises in the early stages of meander development (i.e., when the perturbations are small enough).

Table 4.1: Values of the relevant dimensionless parameters at the beginning of each simulation, i.e., for a straight, slightly and randomly perturbed, planimetric configuration. β_0: bankfull aspect ratio; d_{s0}: dimensionless grain size; τ_{*0}: shields parameter; t/t_{ic}: total time, averaged over runs, adopted in IPS and ZS models and normalized by the time t_{ic} at incipient cutoff conditions.

Runs	β_0	d_{s0}	τ_{*0}	bed	morphodynamic influence	t/t_{ic}
1	12	0.001	0.6	dune	sub-resonant	9.0
2	15	0.005	0.7	dune	super-resonant	8.8
3	20	0.005	0.4	dune	super-resonant	13.5
4	11	0.001	0.5	dune	sub-resonant	14.3
5	25	0.005	0.4	dune	super-resonant	10.6
6	22	0.0025	0.6	dune	super-resonant	9.5
7	13	0.0001	0.6	dune	sub-resonant	15.0
8	15	0.01	0.15	plane	sub-resonant	12.8
9	18	0.01	0.1	plane	super-resonant	14.8
10	14	0.025	0.08	plane	super-resonant	16.7
11	13	0.005	0.1	plane	sub-resonant	14.0
12	20	0.03	0.15	plane	super-resonant	10.3
13	13	0.005	0.1	plane	sub-resonant	7.4

Table 4.2: Real rivers used in the comparison with synthetically generated planforms. Sources are as follows: 1) Beltaos and Day (1978); 2) Stolum (1998); 3) http://glcfapp.umiacs.umd.edu; 4) Lancaster and Bras (2002).

Rivers	Location	Data Source
Lesser Slave River	Alberta, Canada	1,3
Jurua River	Brazil	2,3
Porcupine River	Alaska, USA	3
Athabasca River	Alberta,Canada	3
Rio Madre de Dios	Peru	3
Ramu River	Papua-New Guinea	3
Preacher Creek	Alaska, USA	4
Takotna River	Alaska, USA	4
North Fork Kuskokwim River	Alaska, USA	4
Melozitna River	Alaska, USA	4
Teklanika River	Alaska, USA	4
Dishna River	Alaska, USA	4
Birch Creek River	Alaska, USA	4
North Fork Kuskokwim River, Medfra	Alaska, USA	4
Innoko River	Alaska, USA	4

Table 4.3: Suite of the morphometric variables used to objectively characterize planform meandering patterns.

Variable	Description
σ_T	reach tortuosity
σ_F	full meanders average sinuosity
σ_H	half meanders average sinuosity
ℓ_{av}	half meanders intrinsic length average
ℓ_{va}	half meanders intrinsic length variance
ℓ_{sk}	half meanders intrinsic length skewness
ℓ_{kr}	half meanders intrinsic length kurtosis
$\mathcal{C}_{va}$	variance of local curvature
$\mathcal{C}_{kr}$	kurtosis of local curvature
$\mathcal{A}_{av}$	average half meanders asymmetry coefficient
$\mathcal{A}_{kr}$	kurtosis of asymmetry
$\mathcal{A}_{60-90}$	60th-90th percentile of asymmetry

Table 4.4: Mean values attained by the morphologic variables when considering each type of patterns separately.

Variable	IPS	ZS-sub	ZS-super	NAT
σ_T	3.5	3.2	2.8	2.5
σ_F	2.4	2.3	2.2	1.9
σ_H	1.9	2.0	2.0	1.5
ℓ_{av}	36.7	38.7	20.2	19.7
ℓ_{va}	425.7	193.4	71.5	70.3
ℓ_{sk}	1.6	1.2	1.0	0.8
ℓ_{kr}	7.6	5.3	6.2	3.8
$\mathcal{C}_{va}$	0.007	0.004	0.019	0.018
$\mathcal{C}_{kr}$	6.7	3.5	3.0	3.4
$\mathcal{A}_{av}$	-0.3	-0.13	0.12	0.02
$\mathcal{A}_{kr}$	2.9	2.8	2.5	2.4
$\mathcal{A}_{60-90}$	-0.1	0.01	0.39	0.30

Chapter 5

River cutoffs as part of chaotic dynamics?

5.1 Introduction

The occurrence of cutoffs is a key mechanism in the dynamics of meandering rivers. They introduce a strong source of nonlinearity in the process of river meandering evolution, which strongly contributes to the formation of the complex planform patterns usually observed in nature. In particular, channel shortening induced by cutoffs tend to limit the growth of channel sinuosity [Stolum, 1996], which can decrease dramatically when multiple cutoffs occur within short reaches [Mosley, 1975, Hooke, 2004, Hooke, 2007]. The formation of cutoffs, on the one hand, removes older meanders and thus provides a filtering action which, although tending to reduce the geometrical complexity driven by fluid dynamic processes [Camporeale et al., 2008], do not obscure the signature of the morphodynamic regime experienced by the river [Frascati and Lanzoni, 2009]. On the other hand, the occurrence of cutoffs generates an intermittent noise that is able to influence the spatiotemporal dynamics of the whole river [Camporeale et al., 2008], and may lead, for example, to the formation of multiple loops bends [Hooke, 2007].

Varying opinions exist on the causes of meander cutoffs. Inhomogeneities in bank material [e.g. Friedkin, 1945], changes in effective discharge (or other external conditions)

controlling equilibrium morphology and causing adjustment [Mosley, 1975], occurrence of exceptionally high floods [Erskine et al., 1992; Leys and Werritty, 1999] are some of the causes invoked for the occurrence of cutoffs. Alternative explanations originate from the concept of geomorphic thresholds and complex response, firstly put forward by Schumm [1973]. Sudden changes of the system can take place without significant changes in external conditions provided that a given threshold, to be suitably identified, is exceeded. This idea is quite close to the concept of self-organized criticality introduced by Bak et al. [1987], whereby a state is reached in the system in which sudden readjustment occurs to regain order and reorganization. Stolum [1996], using a simulation model, interpreted the occurrence of clusters of river cutoffs as a mechanism which leads the system to evolve toward a self-organized critical state in which the sinuosity oscillates around a constant mean value. In order to examine the possible evidence of non-linear behavior and self-organized criticality Hooke [2007] proposes to interpret morphological changes observed in actively meandering rivers from the plotting of trajectories and identification of phase spaces.

The idea to explain active meandering systems in terms of chaotic dynamics and self organization is surely fascinating, but needs a deeper insight into the dynamics of cutoff events, with particular reference to the formation of spatiotemporal clusters of cutoffs. Moreover, the detection of a possibly chaotic or self-organized behaviour requires adequate records of planform changes over historical timescales, carried out on long enough homogeneous river reaches. Although good historical data are now available for some highly mobile channels [Hooke 2004, Gautier et al., 2007], a unreasonably longer observation period is likely necessary to reliably detect the presence of chaos. Moreover, the analysis may be complicated by the interplay of both the inherent dynamics of the river and changes in external controls induced by, e.g., hydrologic and climate changes, as well as human activities [Hooke, 2007].

An alternative approach relies on the use of time series obtained from mathematical models. These models, owing to the constraints placed by the the long-time intervals and the large spatial scales to be investigated, are necessarily based on a simplified description

of process laws as well as of external controls. Nevertheless, it has been demonstrated that, when a enough refined, although linearized, flow field model is adopted, these models capture the essential features of both the short and the long term behaviour of meandering rivers [Lanzoni et al., 2006; Camporeale et al., 2007; Frascati and Lanzoni, 2009].

The question we want to address in the present study then is: do mathematical models really provide evidence of a chaotic behaviour of active meandering rivers as suggested by Stolum [1996] and Hooke [2004] on the basis of numerical simulations and field observations, respectively? To this purpose we analyze the results obtained from the mathematical model described in Chapters 2 and 3, which has been shown (see Chapter 4) to contain the fundamental ingredients needed to reproduce correctly the features of real rivers.

5.2 Methodologies

Chaos is one of the topics in the field of nonlinear dynamics, studying the characteristics of the time evolution of dynamical systems. Generally, these systems can evolve stochastically, i.e. according to some random process, deterministically, in which case the future is only uniquely determined by the past according to some rule or mathematical formula, or chaotically. This latter behaviour is often called deterministic chaos and it can only occur when the governing equations are nonlinear.

The features of deterministic chaos are described in a rich literature and a number of analysis techniques have been specifically developed for its characterization. Major research efforts are dedicated to two related questions. The first is if chaos theory can be used to gain a better understanding and interpretation of an observed complex dynamical behavior. The second is if chaos theory can give an advantage in predicting or controlling such time evolution. Time evolution as a system property can be measured by recording time series. Thus, nonlinear time series methods are the tools needed to answer to the above questions.

We note that, among the various classes of observable dynamical systems, chaos lies between the well studied domain of predictable, regular, or quasi-periodic signals and

the set of totally irregular stochastic signals (noise) which are completely unpredictable. Chaos looks like noise when adopting conventional linear tools, such as Fourier transforms. Nevertheless, chaos has a well defined structure in an appropriate state or phase space, and this is the reason why nonlinear methods represent an indispensable tool for chaos analysis. The existence of a defined structure implies that time series generated by a chaotic process can be, at some extent, predicted thus providing useful information for controlling, also from an engineering point of view, the source of the signal.

However, nonlinear time series analysis is far less established than its linear counterpart. Detecting chaos in a signal is still more an art than science, since the application of the various methodologies often do not yield results that can be unambiguous interpreted. The fact that simple deterministic systems generically exhibit complicated temporal behaviors in the presence of nonlinearity has influenced thinking and intuition in many fields, and a wide spectrum of approaches (e.g., chaos, self organized criticality, fractals, neural networks, etc.) have been proposed to study the complex outputs of these systems. Therefore, even though new tests are constantly developed, caution is strongly needed in detecting evidences of chaotic behaviour in a dynamical system, since the results of these tests are seldom definitive.

5.2.1 Chaos in continuous and discrete time dynamics

Let us introduce some notation adopted in the analysis of deterministic dynamical systems in the so called phase space. For simplicity we assume that the phase space is a finite-dimensional vector space $\mathcal{R}^m$. A state is specified by a vector $\mathbf{x}\ \epsilon\mathcal{R}^m$. The dynamic system is described by either m-dimensional discrete map

$$\mathbf{x_{n+1}} = \mathbf{F}(\mathbf{x})_n \tag{5.1}$$

or by system of m first-order ordinary differential equations (i.e., a flow)

$$\frac{d\mathbf{x}(t)}{dt} = \mathbf{F}(t, \mathbf{x}(t)) \tag{5.2}$$

A sequence of points $\mathbf{x}_n$ (or $\mathbf{x}$(t)) solution of the system of equations (5.1) (or (5.2)), given the initial conditions $\mathbf{x}_0$ (or $\mathbf{x}(0)$), is called a trajectory of the dynamical system.

All the time series we will have to deal with are given at discrete time steps, thus we will focus our attention on discrete time maps. Note that also the numerical integration of the differential equations (5.2), with finite time step Δt, yields a map. For example, a continuous flow can be represented as a finite sampled evolution trough the Euler integration scheme:

$$\mathbf{x}(t_0 + (n+1)\Delta t) \approx \mathbf{x}(t_0 + n\Delta t) + \Delta t\, \mathbf{F}(\mathbf{x}(t_0 + n\Delta t)) \tag{5.3}$$

On the other hand, extracting quantitative information from the observations of the signal produced by a dynamical system (i.e., from a map) allows us to analyze only one or, at the best, a few of the dynamical variables which govern the behaviour of the system at hand. A question then arises: how can we characterize the multivariate state (phase) of a complex dynamical system getting information from scalar univariate observations?

5.2.2 Embedding: phase-space reconstruction

The answer to the question raised at the end of the previous section is given by the Taken's delay embedding theorem [Takens, 1981]. The reconstruction, from a scalar time series, of a vector space which is equivalent to the original state space of a system is the basis of almost all nonlinear methods. A scalar measurement is a projection of the unobserved internal variables of a system into an interval of the real axis and, as a consequence, causes a reduction in dimensionality. However, most dynamical properties such as eigenvalues of fixed points and Lyapunov exponents, and topological properties such as the attractor dimension of a system are contained within any observed variable and its time lag. Furthermore, it is not usually necessary or even desirable to reconstruct the entire phase-space from the measured variable since the attractor dimension is often much smaller than the dimension of this space.

It is thus sufficient to construct a new space in which an equivalent attractor can be embedded. This new space should have the properties that every points in it maps to

a unique next point of the dynamics (uniqueness of the dynamics) and that there is a smooth nonsingular transformation between it and the original space. Furthermore, this new space is chosen to be Cartesian (rectangular) rather than curve. This method is called phase-space reconstruction and was proposed by Takens [1981] and later on generalized by Sauer and Yorke [1993].

Embedding parameters

The problem to convert observations into a state vector is called phase-space reconstruction. The most important phase space reconstruction technique is the method of delays. Vectors in a new space, the embedding space, are formed from time delayed values of the scalar measurements [Kantz and Schreiber, 1997]:

$$\mathbf{x}_n = (x_{n-(m-1)\tau_d}, x_{n-(m-2)\tau_d}, ..., x_{n-\tau_d}, x_n) \tag{5.4}$$

where the number m of elements is called the embedding dimension, while the time τ_d is generally referred to as the time delay (or lag).

The time delay τ_d between successive elements in the delay vectors is not the subject of the embedding theorem. However, for practical purposes the proper choice of the delay time τ_d is quite important. If it is taken too small, there is almost no difference between the different elements of the delay vectors, and all points are accumulated at the bisectrix of the embedding space (Figure 5.1b), leading to redundancy (Casdagli et al. [1991]). On the contrary, if τ_d is chosen too large, the different coordinates may be almost uncorrelated. In this case the reconstructed attractor may be very complicated even when the underlying true attractor is simple (Figure 5.1d).

Unfortunately, there is no rigorous way of evaluating the optimal value of the time delay, and it is even unclear what properties the optimal value should have. In the practical application one can try to optimize the performance of the choice by varying the value of τ_d. Some quantitative tools are however available to guide the choice of τ_d. The most natural statistic is the autocorrelation function of the signal:

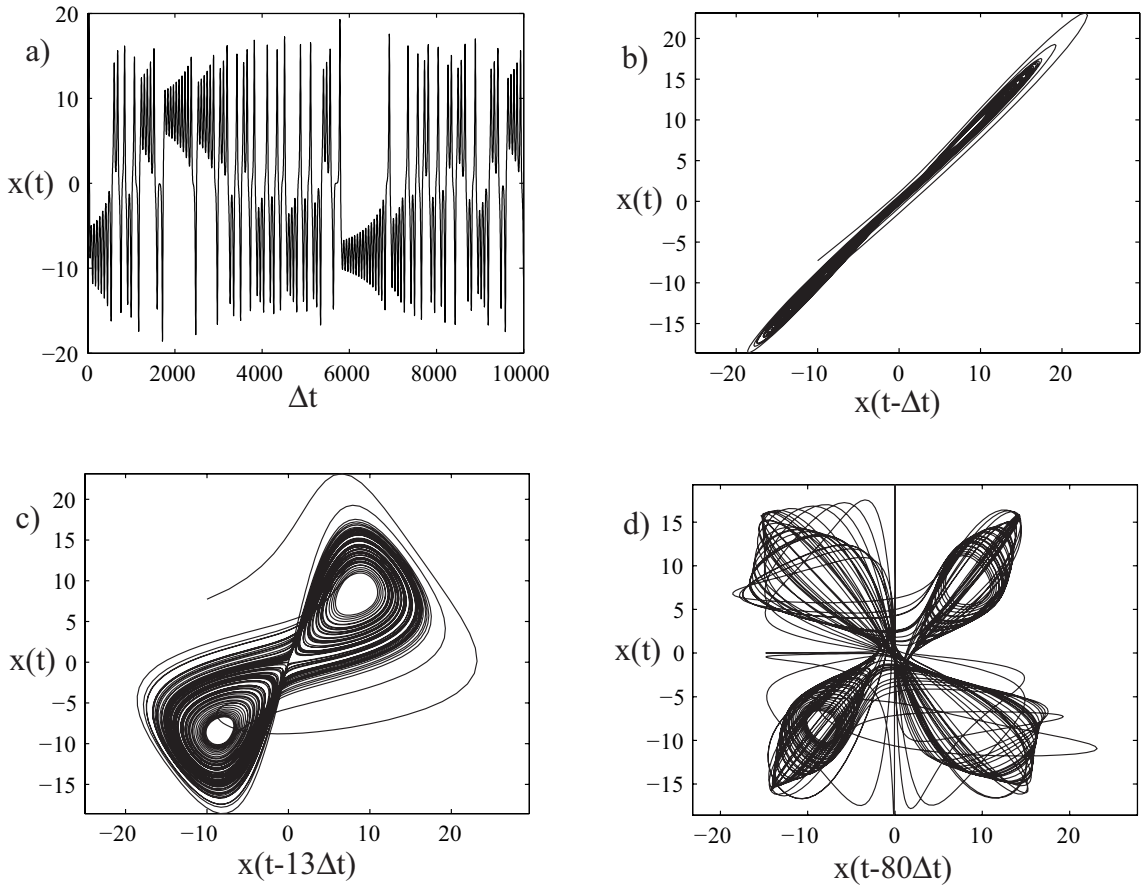

Figure 5.1: a) Time series generated by the $x(t)$ component of the Lorenz system of differential equations. The system has been solved through the Runge-Kutta method with a time step $\Delta t = 0.01$. The parameters used in the computations are: $\sigma = 10, r = 28, b = 8/3$. b) Examples of time delay representation of the signal when: a) the time delay is taken too small (redundancy); c) the time delay is correctly chosen; d) the time delay is taken too large (the reconstructed attractor appears very complicated).

$$c(\delta) = \frac{\langle \left(w_n - \langle w \rangle\right)\left(w_{n-\delta} - \langle w \rangle\right) \rangle}{\langle \left(w - \langle w \rangle\right)^2 \rangle} \tag{5.5}$$

where δ is the lag, $\langle \cdot \rangle$ is a linear operator indicating the expected value of the function. In order to approximate the data in a hypersphere in higher dimension, $c(\delta)$ should be zero at lags equal or larger than τ_d. However, following this condition can lead to cross the limit of uncorrelated element which is not desirable. Therefore, a reasonable value for time delay τ_d, is the time at which the autocorrelation function decays to $1/e$ (whit e Neper's number) [Kantz and Schreiber, 1997]. A quite reasonable objection to this procedure is that is based on linear statistics, and hence does not take into account nonlinear dynamical correlations among data. Conversely, the average mutual information [Fraser and Swinney, 1986] takes into account also nonlinear correlation. The mutual information is defined as:

$$I(\delta) = \sum_{i,j} p_{ij}(\delta) \ln p_{ij}(\delta) - 2 \sum_{i} p_i \ln p_i \tag{5.6}$$

where, for some partition on the real numbers, p_i is the probability to find a time series value in the i-th interval, while $p_{ij}(\delta)$ is the joint probability that an observation falls into the i-th interval and the observation time δ later falls into the j-th. If the delayed mutual information $I(\delta)$ exhibits a marked minimum at a certain value of δ, then this is a good candidate for a reasonable time delay τ_d. However, there is no theoretical reason why there always has to be a minimum. Moreover, the argument defining the first minimum of the average mutual information as a good choice of time delay has to be modified when the embedding dimension exceeds two [Kantz and Schreiber, 1997]. Therefore, when the minimum of the mutual information lies at times considerably larger than the $1/e$ decay, it is in any case advisable to chose τ_d inside this latter interval.

The embedding dimension m represents the integer global dimension necessary to unfold observed orbits from self overlaps arising from projection of the attractor on a lower dimensional space. A method to determine the minimal sufficient embedding dimension m was proposed by Kennel et al. [1992]. It is called the false nearest neighbour method. The method is conceptually simple: find the nearest neighbour $\mathbf{x}_l$ for each points $\mathbf{x}_n$ in a time-delay embedding m, and define the separation between this point as follows:

$$R_n(m) = \sqrt{(\mathbf{x}_l - \mathbf{x}_n)^2 + (\mathbf{x}_{l-1} - \mathbf{x}_n)^2 + \cdots + (\mathbf{x}_{l-\tau_d} - \mathbf{x}_n)^2} \tag{5.7}$$

Then calculate the separation $R_n(m+1)$ in an embedding $m+1$. If $R_n(m+1)$ significantly exceeds $R_n(m)$, then the neighbours are close only because of the overlapping of the trajectories and are false. The criterion of falseness is thus

$$\frac{R_n(m+1)}{R_n(m)} > R_T \tag{5.8}$$

where R_T is a threshold value. Abarbanel [1996] recommends $R_T = 15$, but the value is not critical. It is worthwhile to stress that if an m-dimensional embedding yields a close representation of the state space, every m'-dimensional reconstruction with $m' > m$ does so as well. This argument is important because if too small m causes trouble we can optimize the analysis by varying m. However, the choice of a too high m may also cause some troubles. In fact, if m is unnecessarily high the data becomes sparse and each embedding dimension introduces additional noise. With experimental data, an objective criterion is needed (e.g., the false nearest neighbours test), and the optimal embedding is probably different for the various tests. For this reason, dealing with real data (i.e., maps), it is advisable to systematically investigate a wide range of values of m and τ_d. Figure 5.2 shows an example of phase space reconstruction of the Lorenz attractor achieved employing the method of delays.

5.2.3 Space-time separation plot

Space-time separation plots, introduced by Provenzale et al. [1992], helps identifying temporal correlations inside the time series and is relevant to estimate a reasonable delay time, and, more importantly, the Theiler-window t_w to be used in dimension and Lyapunov analyses. The idea is that in presence of temporal correlations the probability that a given pair of points has distance smaller than ϵ does not only depend on ϵ but also on the time that has been elapsed between the two measurements. This dependence can be detected by plotting the number of pairs as a function of the relative time separation Δt and the spatial distance ϵ. Two examples of space-time separation plots for the Lorenz attractor

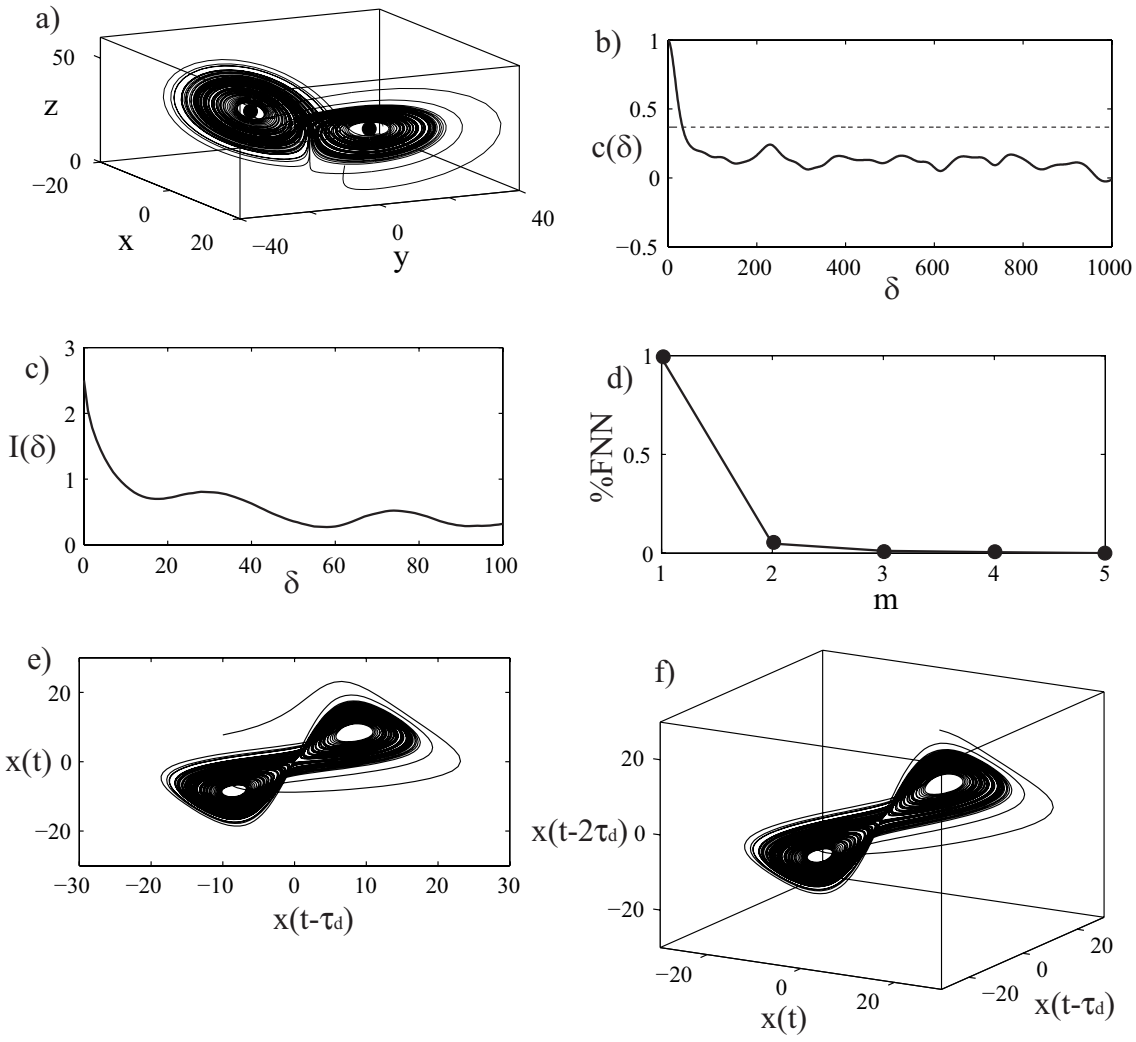

Figure 5.2: a) Three-dimensional visualization of the Lorenz strange attractor. b) Autocorrelation function of the $x(t)$ component; the dotted horizontal line is located at $c(\delta) = 1/e$. c) Average mutual information of the $x(t)$ component. d) Percentage of false nearest neighbours as a function of the embedding dimension m using τ_d=17 individuated from $I(\delta)$ plot. e),f) Two-dimensional and three-dimensional visualization of the reconstructed attractor of the $x(t)$ component.

are reported in Figure 5.3a. The contour lines reported in the plo indicate the distance required to find a given fraction of pairs, depending on their temporal separation δt. Only values of δt where lines are flat (or, on average, oscillate around a mean value), temporal correlation does not cause spurious effects in the correlation sum.

5.2.4 Attractor dimension

Let $C(\epsilon)$ be the correlation sum defined by the number of points which are closer than a given distance ϵ,

$$C(m,\epsilon) = \frac{2}{N(N-1)} \sum_{i=1}^{N} \sum_{j=i+1}^{N} \Theta(\epsilon - \|\mathbf{x}_i - \mathbf{x}_j\|) \tag{5.9}$$

where Θ is the Heaviside function

$$\Theta = \begin{cases} 0 \ for \ x < 0 \\ 1 \ for \ x \geq 0 \end{cases} \tag{5.10}$$

and $\|\mathbf{x}_i - \mathbf{x}_j\|$ is the spatial separation between two points i and j, usually given by the Euclidean norm in an m-dimensional time-delay embedding. The correlation sum $C(m,\epsilon)$ converges to the correlation integral for $N \to \infty$ (N being the number of data). The relationship (5.9) used to quantify the correlation sum is called the Grassberger and Procaccia [1983a,b] algorithm. Equivalently, $C(m,\epsilon)$ can be considered as the probability that two different randomly chosen points have to be closer than a given distance ϵ.

The correlation dimension D_2 is defined by

$$D_2 = \lim_{\epsilon \to 0} \lim_{N \to \infty} \frac{d \log C(m,\epsilon)}{d \log \epsilon} \tag{5.11}$$

and can be determined by plotting $\log C(m,\epsilon)$ versus $\log \epsilon$ and determining, through a fitting, the straight line line for which saturation occurs (Figure 5.3b,c):

Since the statistical fluctuations in plots like the one depicted in Figure 5.3b show characteristic correlations, it has been suggested [Takens, 1985; Theiler, 1988] to apply a maximum likelihood estimator to obtain optimal values for D_2 (Figure d). The Takens-Theiler estimator reads:

$$D_{TT}(\epsilon) = \frac{C(m,\epsilon)}{\int_0^\epsilon \frac{C(m,\epsilon)}{\epsilon} d\epsilon} \tag{5.12}$$

The literature dealing with the correct and spurious estimation of the correlation dimension is huge [Kantz and Schreiber, 1997]. The most important precaution is to exclude temporally correlated points from the pair counting into (5.9) by introducing the so called Theiler window t_w. In order to become a consistent estimator of the correlation integral (from which the dimension is derived), the correlation sum should cover a random sample of points drawn independently according to the invariant measure on the attractor. Therefore, all pair of points in equation (5.9) whose time indices differ by less than t_w are ignored in the computation of $C(\epsilon)$.

5.2.5 Exponential divergence: Lyapunov exponents

Chaos arises when the trajectories of a dynamic system are highly sensitive to initial conditions, thus leading infinitesimal perturbations to grow exponentially. A global folding mechanisms also acts to guarantee that solutions maintain bounded. The exponential instability is characterized by the spectrum of Lyapunov exponents [Eckmann and Ruelle, 1985]. Lyapunov exponents are invariant under smooth transformations and are thus independent of the measurement function or the embedding procedure. They carry a dimension of an inverse time and have to be normalized to the sampling interval. However, there is a practical problem in the computation of spectrum. In fact, since the physical phase space is unknown, the spectrum is computed in some reconstructed embedding space. Thus the number of exponents depends on the reconstruction, and might be larger than in the physical phase space. Such additional exponents are called spurious and there are several suggestions to either avoid them or to identify them [Stoop and Parisi, 1991].

Here, we restrict our attention on the maximal Lyapunov exponent λ_{max} (Figure 5.4a). It can be determined numerically without the explicit construction of a dynamic model for the investigated time series. Let us consider two points $\mathbf{x}_0$ and $\mathbf{x}_i$ with distance $\Delta\mathbf{x}_0 \ll 1$ at time t_0. Each of these points generate an orbit in the state space. Denoting by $\Delta\mathbf{x}$ the distance at time t between the two trajectories emerging from these points, then λ_{max}

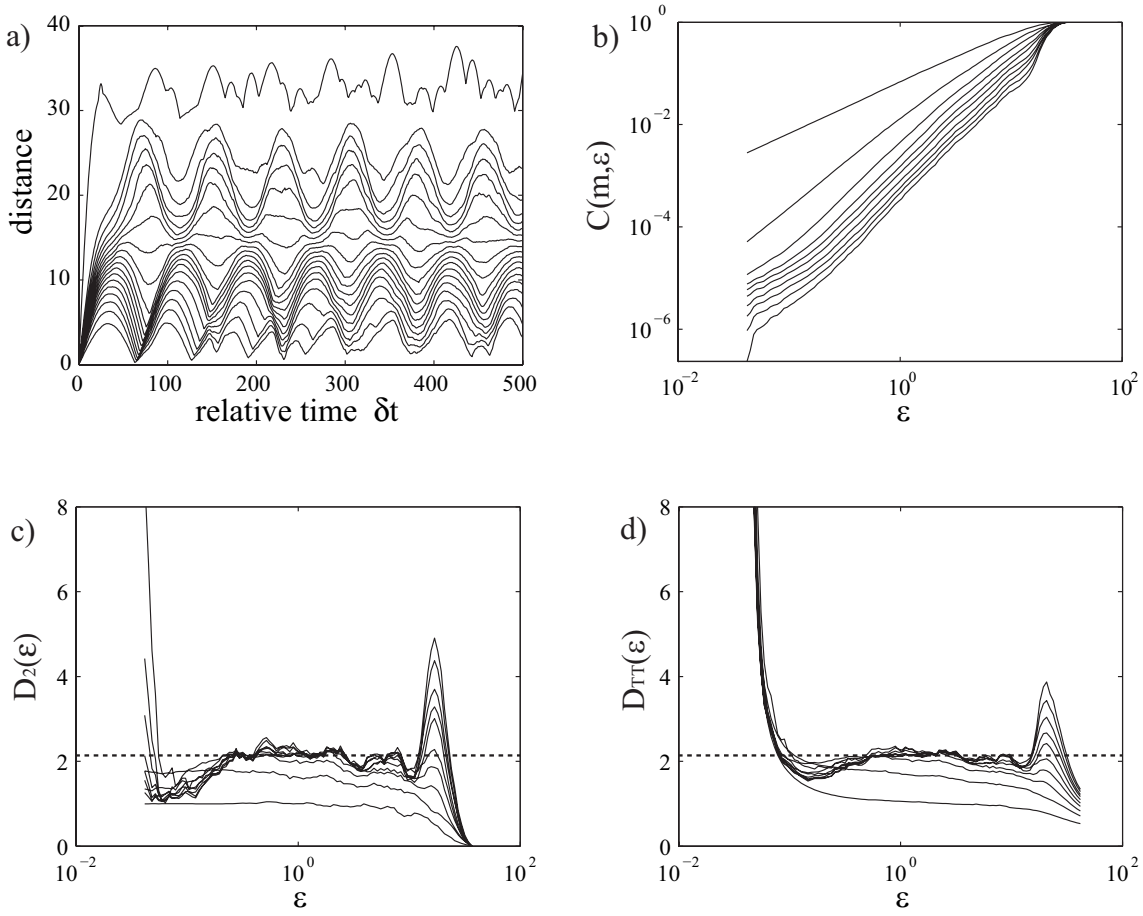

Figure 5.3: a) Space-time separation plot for the $x(t)$ component of the Lorenz model. An initially fast increase is later followed by stable oscillations with the dominant period of the system. b) Correlation sum of $x(t)$. Estimation of the correlation dimension for various embedding ($m = 1, ..., 10$): c) slopes of the correlation determined by straight line fitting of the log-log plot of the correlation sum $C(m, \epsilon)$; d) Takens-Theiler estimator of the same slope. In both plots a clear saturation is evident for $m \geq 3$. For attractors with less uniform measures, the saturation is less pronounced, and there is some benefit in using an embedding higher than theoretically necessary. The Theiler's window has been set equal to 100, as suggested by the space-time plot a).

can be determined by

$$\Delta \mathbf{x} \simeq \Delta \mathbf{x}_0 e^{\lambda_{max}(t-t_0)} \tag{5.13}$$

If λ_{max} is positive (see Figure 5.4a), then nearby points, no matter how close, will diverge exponentially. Thus the orbit is unstable and chaotic. Since a positive maximal exponents is a strong signature of chaos, it is of considerable interest to determine its value for a given time series. A robust, consistent and unbiased estimator for the maximal Lyapunov exponent is given by:

$$S(\epsilon, m, t) = \frac{1}{N} \sum_{i=1}^{N} \ln \left(\frac{1}{|\mathcal{U}(\mathbf{x}_0)|} \sum_{\mathbf{x}_i \in \mathcal{U}(\mathbf{x}_0)} |\mathbf{x}_0(t) - \mathbf{x}_i(t)| \right) \tag{5.14}$$

where the reference points $\mathbf{x}_0$ are the embedding vector, and $\mathcal{U}(\mathbf{x}_0)$ is the neighbourhood of $\mathbf{x}_0$ with diameter ϵ. If $S(\epsilon, m, t)$ exhibits a linear increase with identical slope for all m larger than some m_0 and for a reasonable range of ϵ, then this slope can be taken as an estimate of the maximal exponent λ_{max}. Apart from parameters characterizing the embedding, the initial neighborhood size ϵ is of relevance: the smaller ϵ, the large the linear range of S, if there is one. Obviously, noise and the finite number of data points limit ϵ from below. Figure 5.4b shows a linear increase with identical slope for reasonable range of ϵ. The trajectories are exponentially divergent, thus unstable and chaotic.

5.2.6 Testing for nonlinearity: the surrogate data

Preliminarily to any investigation on the existence of chaos signatures within a given temporal series, it is necessary to ascertain wether the data contain a certain degree of nonlinearity. Indeed, nonlinearities are a fundamental ingredient of deterministic chaos. Answering to the above question is not a trivial task and several methods are available. In this contest we adopt a surrogate-based methodology. Surrogates are constructed in such a way to have the same power spectrum and, hence, the same autocorrelation function of the original series, but any inherent nonlinearity is destroyed since the process by which the surrogates are generated randomizes the phases in the Fourier space. The

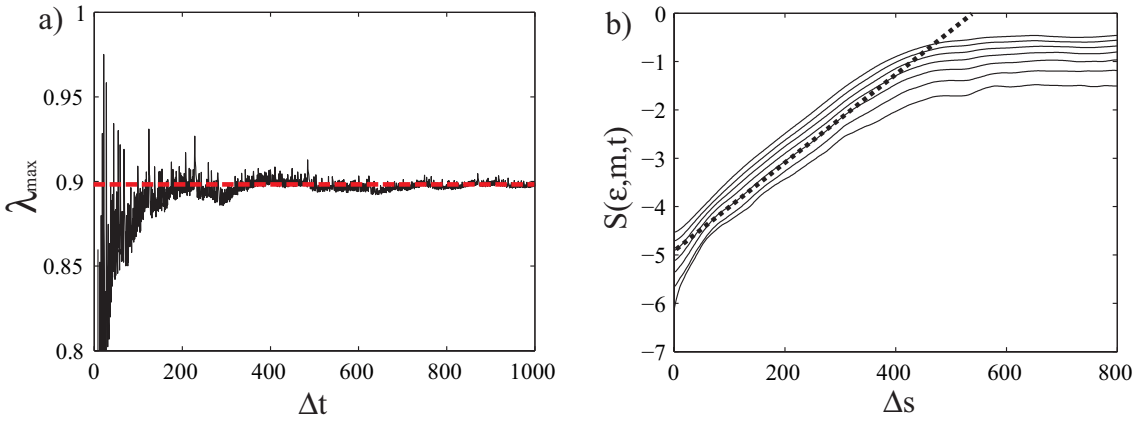

Figure 5.4: a) Convergence at the largest Lyapunov exponent $\lambda_{max} \approx 0.9$ for the $x(t)$ component of the Lorenz attractor. b) Estimation of λ_{max} from the map of $x(t)$. The straight line has slope $\lambda \approx 0.09$ which normalized with the time integration step $\Delta t = 0.01$ gives a good approximation of λ_{max}. The parameters are: $\tau_d = 17$, $m = 2, ..., 8$.

method is conceptually simple and can be summarized as follows: i) calculate the discrete Fourier Transform of the test data (this consist of an amplitude and a phase at each frequency); ii) randomize the phase at each frequency, imposing a uniform distribution in the interval $[0, 2\pi]$ (this preserve the phase and the symmetry around frequency 0); iii) take the inverse Fourier Transform. The method we used for surrogate series generation is the Iterative Amplitude Adjusted Fourier Transform (IAAFT) method of Schreiber and Schmitz [1996]. This method is an improvement of the earlier Amplitude Adjusted Fourier Transform (AAFT) method of Theiler et al. [1992], and iteratively adjusts both the pdf and linear correlation structure to minimize their deviation from the original series.

The surrogate time series are used to estimate how a given statistic is distributed in the absence of dynamical nonlinearity. Therefore, the null hypothesis is that the data are adequately described by their single time probability distribution and their power spectrum. If the value of the statistic for the test data fails into the distribution for surrogate data, then there is no evidence of dynamical nonlinearity. On the other hand, if the test data have a value for the statistic that is outside of the distribution for the surrogates then we can conclude that the test data are somehow different from the surrogates. Thus, if we assume that the dynamics underlying the test data are stationary we then have

evidence that there is some dynamical nonlinearity in the original data set.

Once an ensemble of surrogate series is generated, a time reversibility test and a locally constant predictor test are used as discriminating statistics for the detection of nonlinearities. In order to get tests at the 99% level of significance, we generate collections of 99 surrogate time series which share with the data the single time sample probability distribution and the periodogram. Figure 5.5 shows an example of surrogate data tests applied to the Lorenz series.

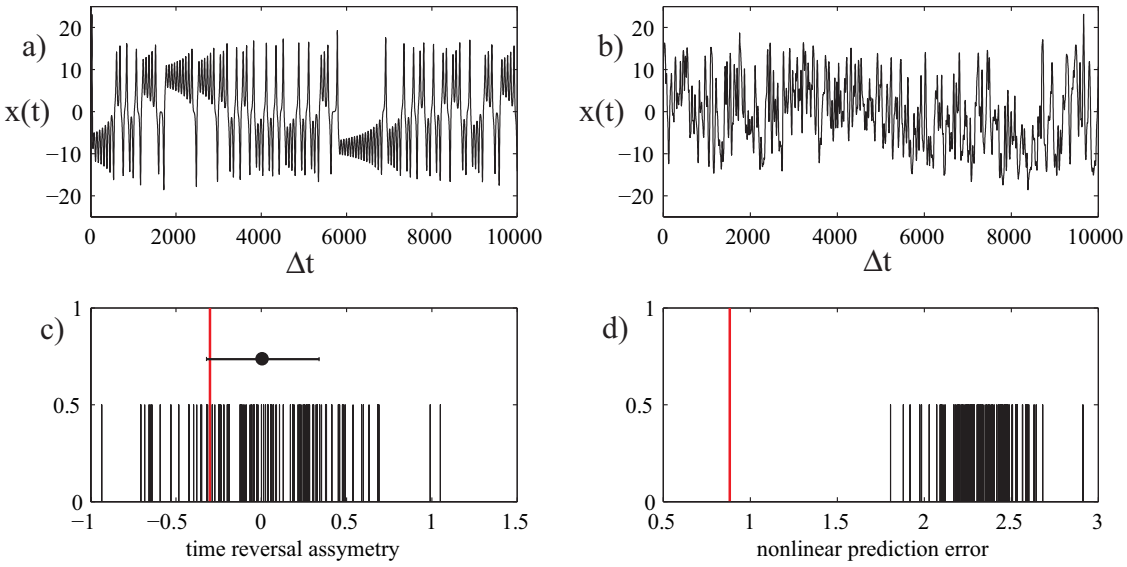

Figure 5.5: a) Time series of the $x(t)$ component from the Lorenz model. b) Example of surrogate time series of $x(t)$. c),d) Tests for nonlinearity. The red longer line denotes the original data set, while black shorter lines refer to surrogates. The error bar indicates the mean and standard deviation of the statistic computed for the surrogates. c) Time reversibility test: the null hypothesis cannot be rejected. d) Locally constant predictor test: the null hypothesis has to be rejected, since the prediction error for the original data is smaller than the errors for the surrogates. The test clearly indicates that predictability is significantly reduced by destroying the nonlinear structure which characterize the Lorenz attractor.

5.2.7 Deterministic vs stochastic signals

Before pursuing numerical tests, it is useful to distinguish between deterministic and stochastic signals. To this aim we consider the following quantity [Cao, 1997]:

$$E(m, \tau_d) = \frac{1}{N - m\tau_d} \sum_{i=1}^{N-\tau_d} |\mathbf{x}_{i+m\tau_d} - \mathbf{x}_{n(i,m)+m\tau_d}| \tag{5.15}$$

where $n(i, m)$ is the integer such that $\mathbf{x}_{n(i,m)}(m)$ is the nearest neighbor of $\mathbf{x}_i(m)$. Its variation from m to $m + 1$ can be investigated by considering

$$E_2(m, \tau_d) = E(m + 1, \tau_d)/E(\tau_d) \tag{5.16}$$

For a random time series, since the future values are independent of the past ones, $E_2(m)$ will be nearly equal to 1 for any m investigated. On the contrary, for deterministic data, $E_2(m, \tau_d)$ is certainly related to m. As a result, $E_2(m, \tau_d)$ cannot be a constant for all m and, hence, there must exist some value of m such that $E_2(m, \tau_d) \neq 1$. Figure 5.6 clearly shows the ability of this quantity to discriminate deterministic signals (Lorenz series) from stochastic (colored noise) signals.

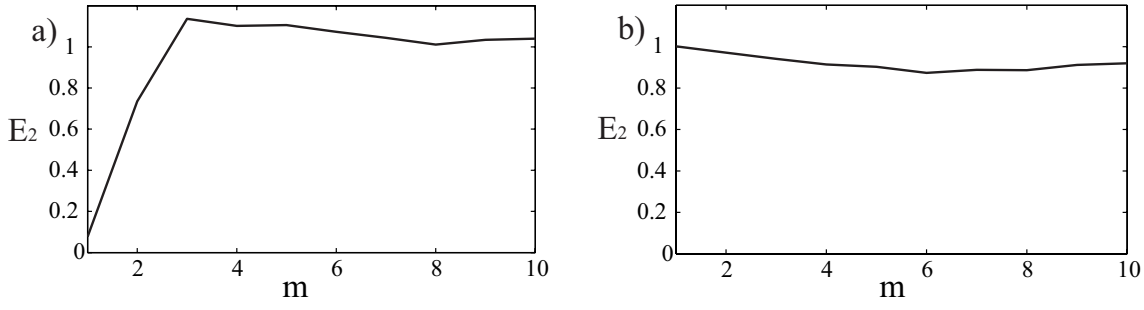

Figure 5.6: Deterministic versus stochastic test. a) $x(t)$ component from the Lorenz model. This data are clearly highly deterministic, since $E_2 < 1$ for $m < 4$. b) Gaussian colored noise generated from the relation: $x_{n+l} = 0.95x_n + y_n$, where y_n is a white gaussian noise. Here E_2 is approximately equal to 1 for any m.

5.3 Results of nonlinear analyses

We now apply the methodologies describes in the previous sections to ascertain whether a signature of chaotic behaviour can be found in the spatiotemporal patterns arising from the long term numerical simulation of meandering rivers.

Figure 5.7a shows that, starting from a straight planar configuration randomly perturbed, the reach tortuosity, σ_T, after an initial monotonic growth until incipient cutoff conditions (region I), begin to fluctuate (region II), eventually reaching a steady state, in which it oscillates around a constant value (region III). Figures 5.7b,c show that the introduction at a certain instant (i.e., $\tau_3 \simeq 760$) of a small disturbance leads to quite different series of both the curvature (Figure 5.7b) and the final planform configurations (Figure 5.7c). We then wonder wether this long term behaviour is characterized, or not, by deterministic chaos signatures.

The deterministic dynamics of the system under investigation is described by discrete maps of the forms:

$$\mathbf{x}_{i,n+1} = \mathbf{F}(\mathbf{x}_{i,n}) \qquad \mathbf{F} : \mathcal{R}^2 \rightarrow \mathcal{R}^2 \tag{5.17}$$

obtained by discretizing the equations giving the displacements of the channel axis. Here, the suffixes i and n denote the i-th point, $\mathbf{x}_i$, of the channel axis and the discrete time $t = n\Delta t$, respectively. Moreover, $\mathbf{F}(\mathbf{x}_{i,n}) = \mathbf{x}_{i,n} - \zeta_{i,n}[\cos(\theta_{i,n}), \sin(\theta_{i,n})]$, with $\theta_{i,n}$ the value attained at each node of the angle that the local tangent to the channel axis forms with the direction of the reference Cartesian axis x (see Chapter 2). The spatiotemporal patterns given by the sequences of points $\{\mathbf{x}_{i,n}\}$ represent a set of trajectories of our dynamical system, which are uniquely determined once the initial conditions $\mathbf{x}_{i,0}$ are specified.

The nonlinear analysis of spatiotemporal patterns, however, is a subject which, at the present is not yet settled, and no general methods are available. We have then to resort to either spatial patterns, as done by Montgomery [1993] or to a quantity which likely synthesize the overall behaviour of the system, such as the tortuosity [Stolum, 1996]. Obviously, the significance of this latter measure in summarizing the intrinsic features

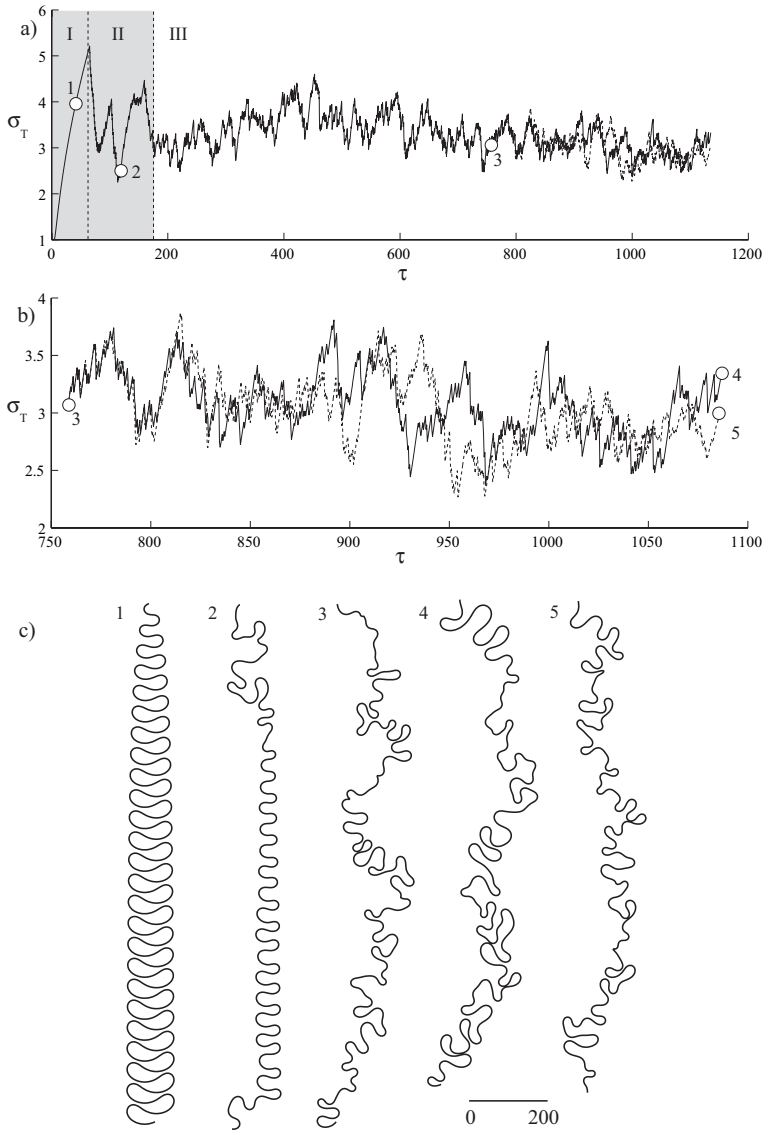

Figure 5.7: Data used in the nonlinear investigation of the possible existence of a chaotic behaviour in synthetically generated meandering planforms. a) Time-series of the reach tortuosity, σ_T. The first grey region refers to the initial phase in which the sinuosity progressively grows until incipient cutoff conditions. The second grey region characterizes a phase in which, owing to repeated cutoff events, the sinuosity reach a steady state. Finally, the third region, represent steady conditions, whereby the tortuosity oscillates around a constant value. The point denoted by 3, it the instant at which a small perturbation is introduced in the planform configuration resulting after a given cutoff event. b) Stretch of the steady region, for $\tau > \tau_3$. The continuous and the dashed lines denotes the unperturbed and the perturbed tortuosity time series, respectively. c) Spatial patterns characterizing a few typical time instants (pointed out in the previous plots) of the evolutionary process. In particular, configurations 4 and 5 correspond to unperturbed and perturbed planforms attained at the end of the simulations.

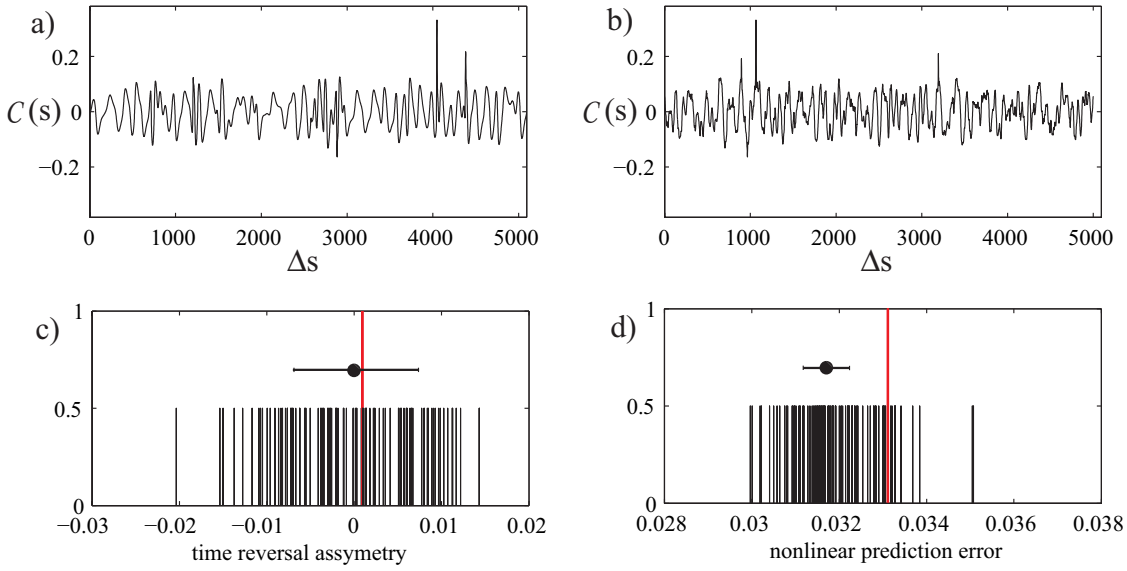

Figure 5.8: a) Spatial series of the channel axis curvature $\mathcal{C}(s)$ for the configuration 4 of Figure 5.7. b) Example of a surrogate series of $\mathcal{C}(s)$. c) Space reversibility test. d) Locally constant predictor test. It is evident that the data are not singled out by these properties and we are unable to reject the null hypothesis of a linear stochastic stationary process.

of the whole dynamics system, and hence its state, is not known. Several measures may indeed act as state parameters [see, e.g., Frascati and Lanzoni, 2009]. Here, the tortuosity is considered only because it represents the simplest possible state parameter.

5.3.1 Testing for nonlinearity

Most of the methods and quantities adopted to detect signatures of deterministic chaos are most appropriate in cases where the data show strong and consistent nonlinear deterministic signatures. Therefore, before addressing nonlinear analyses it is advisable to establish statistical evidence for nonlinearity. Surrogates series and deterministic versus stochastic test, described in section 5.2.6 and 5.2.7, respectively, are used to this aim.

Figure 5.8 shows the reversibility test and the locally constant predictor test carried out for the spatial series of the channel axis curvature corresponding to the unperturbed final configuration reported in Figure 5.7. Both tests indicate that the null hypothesis can not be rejected, and therefore suggest that no nonlinearity, or at the most, only a

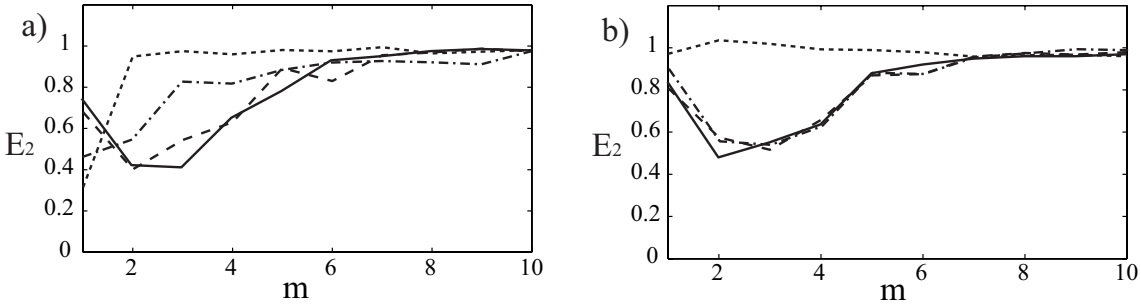

Figure 5.9: Deterministic versus stochastic test. a) Curvature series. b) Tortuosity series. Various plots of E_2 for given values of the space delay τ_d are shown: dotted line, $\tau_d = 5$; dash-dotted line, $\tau_d = 5$; dashed line, $\tau_d = 20$; solid line, $\tau_d = 50$. Note that if τ_d is too small, the strong correlation among data alters the test.

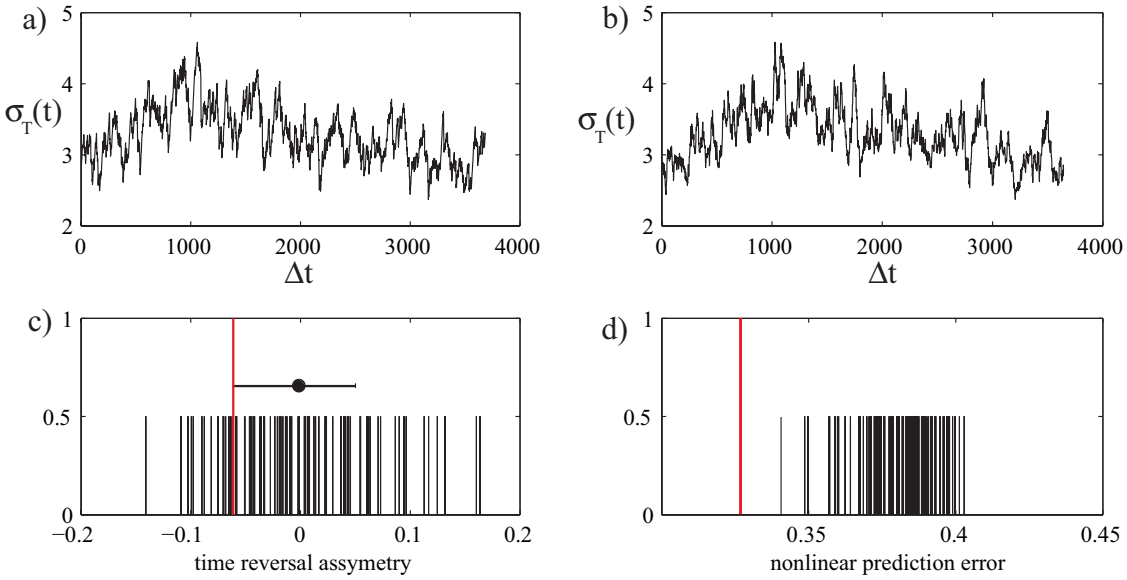

Figure 5.10: a) Time series of the channel tortuosity $\sigma_T(t)$ recorded after statistically steady conditions have been attained (region III of Figure 5.7. b) Example of a surrogate series of $\sigma_T(t)$. c) Time reversibility test. d) Locally constant predictor test. Since the prediction error is lower for the data (longer red impulse) than for the 99 surrogates (shorter black impulse), the null hypothesis can be rejected at the 99% level of significance.

weak nonlinearity characterizes the investigated planform. This result is in accordance with the outcomes of the various tests for detecting nonlinearities carried out by Perucca et al. [2005] on the curvature series of the planimetry of various real meandering rivers.

On the other hand, the test depicted in Figure 5.9 clearly indicates that the curvature spatial series (5.9a) as well as the time series of the tortuosity (5.9b) are clearly of deterministic origin.

The nonlinearity tests for the time series of tortuosity are reported in Figure 5.10. The nonlinear prediction test clearly suggests that null hypothesis can be rejected and, hence, the series exhibits a certain degree of nonlinearity.

5.3.2 Embedding parameters

The embedding parameters which likely characterize the spatial series of curvature are investigated in Figure 5.11. The false nearest neighbours method suggests an embedding dimension m in the range 2-6 for the curvature series (Figure 5.11d) , in accordance with the analyses carried out by Montgomery [1993] on a set of real rivers. Less clear is the embedding dimension for the tortuosity time series, for which a range 10-20 is suggested.

A glance at the autocorrelation function and at the mutual information shown in Figures 5.11b,c suggests that a space lag $\tau_d \simeq 20$ can be used for the analysis of the curvature series. The phase plots of Figures 5.11e,f, however, dot not suggest any particular structure of the signal.

The analyses shown in Figure 5.12 have been repeated also for the tortuosity time series. The resulting embedding dimension m is in the range 10-20, while no clear indications on the time delay emerge from the autocorrelation function and the mutual information.

5.3.3 Dimensions

The correlation dimensions calculated for the space series of the curvature and the time series of the tortuosity are shown in figures 5.12 and 5.15, respectively. In both cases no saturation of the curves obtained varying the embedding dimension is observed. This

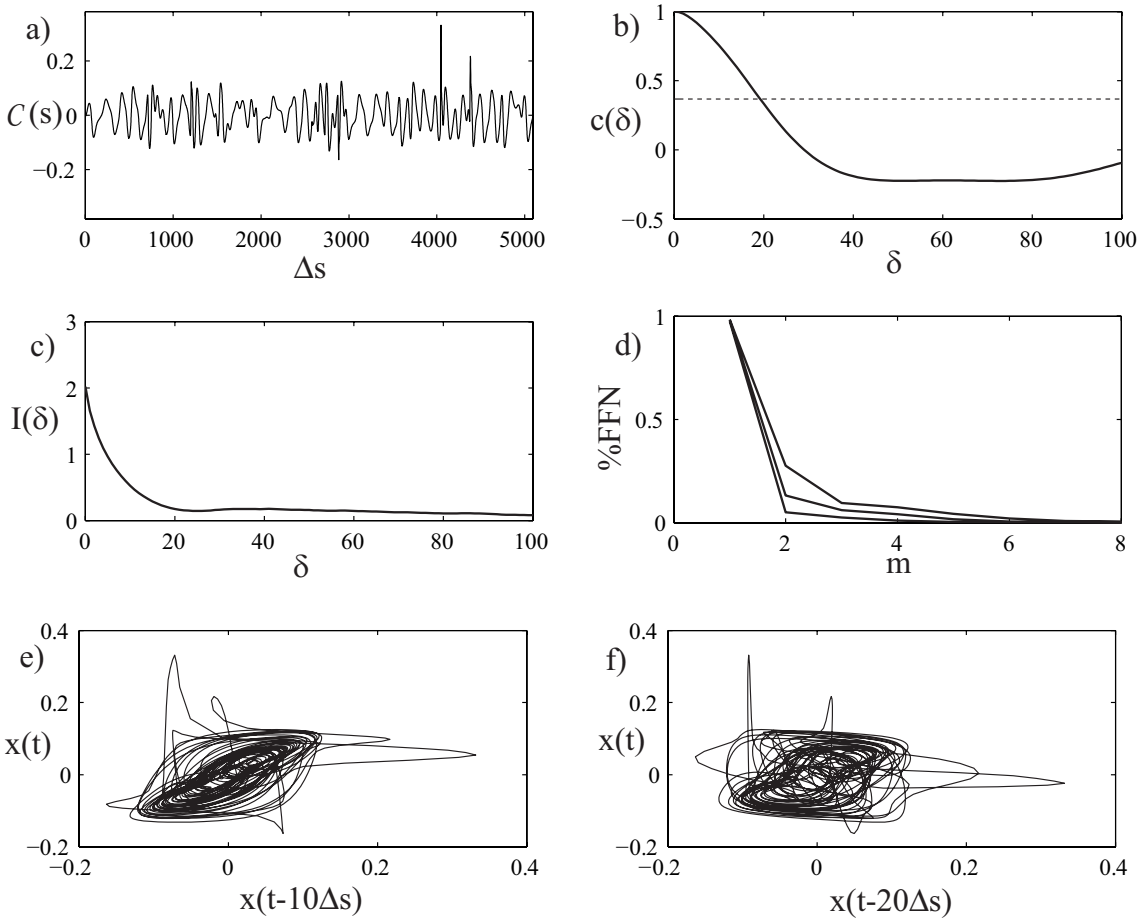

Figure 5.11: a) Curvature series. b) Autocorrelation function. d) Average mutual information. c) Percentage of false nearest neighbour (for various value of the ratio factor) as a function of the embedding dimension m using a space delay $\tau_d \cong 20$ individuated where the autocorrelation function decays to $1/e$. e),f) Phase space reconstruction of the attractor using a space delay $\tau_d = 10$ and $\tau_d = 20$, respectively.

imply that no scaling range exists and the dimension cannot be established. It is however worthwhile to note that the dimension arising from the space series of the curvature for $m = 6$ is close to the value 2.5 found by Montgomery [1993]. However, this value emerge only if if a very small spatial delay is taken and then imposing a strong correlation among data.

Similar results are obtained also for the time series of tortuosity, as depicted in Figure 5.15. Again, no plateau common to all the embedding dimensions is detected by using the various estimators and, as a consequence, a unique value of the dimension cannot be established.

Note that, in both the analyses of the curvature and of the tortuosity series, a value of Theiler window suggested by the space-time separation plot (see Figure 5.14a) has been adopted.

5.3.4 Lyapunov exponents

The estimation of the maximal Lyapunov exponent λ_{max} for the space series of the curvature and the time series of the tortuosity are reported in figures 5.14 and 5.15, respectively. In both case, even though a wide range of values of m and τ_d has been considered, no linear increase of the plotted curves can be clearly detectable. This lack of robust exponential divergence of nearby trajectories which emerges from these analysis suggests the idea that, not only the active meandering river geometry, but also the entire meandering dynamics cannot be considered as part of chaotic system.

5.3.5 Cutoffs inter-arrivals

Stolum [1996] explained the robustness of the stationarity state of long term meanders in terms of a dynamical state of self-organized criticality (SOC). Actually, if meandering systems really tended to SOC then spatial and temporal power-law scaling should be expected [Bak, 1987]. On the contrary, our analysis of neck cutoff processes temporal distribution reveals that their time inter-arrivals are exponentially distributed (Figure 5.16). Now, it is well known that exponential distributions belong to a class of proba-

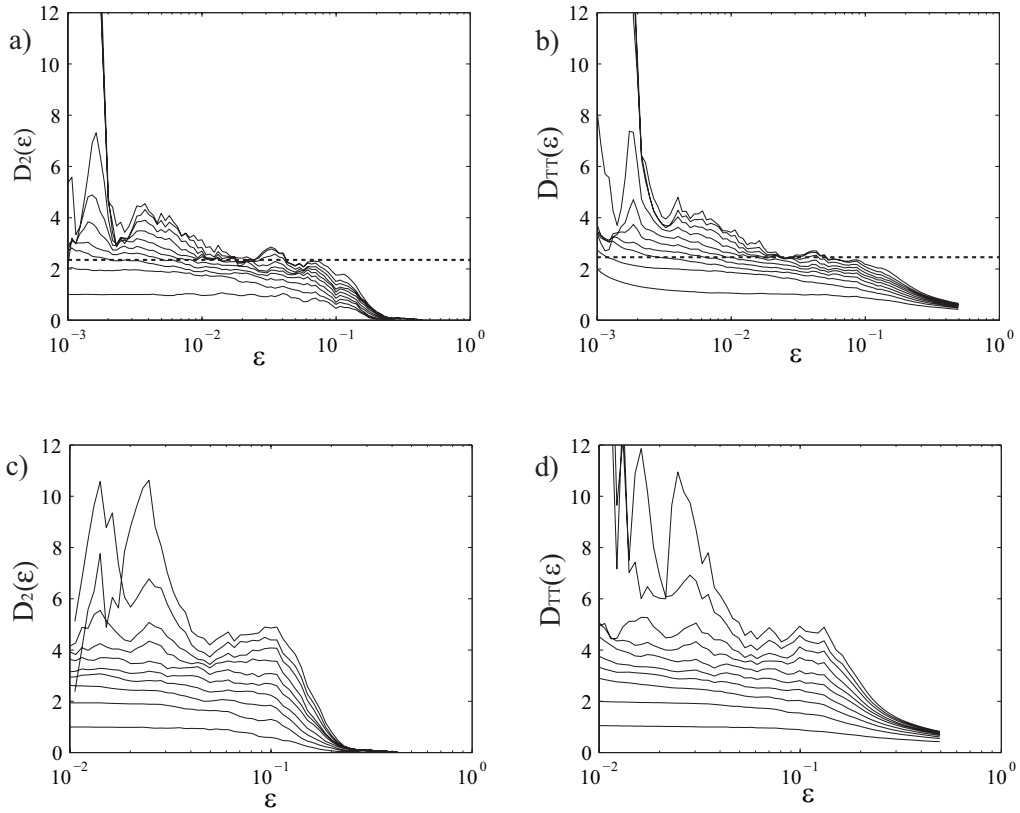

Figure 5.12: Correlation dimension of the curvature series for various embedding dimension ($m = 2, ..., 12$). Panels a),b) show the local slope estimator and Takens-Theiler's estimator for a space delay $\tau_d = 5$, respectively. c),d) Same plots obtained setting $\tau_d = 20$. t_w has been set equal to 100. No saturation is detectable for value of space delay close to that resulting from the autocorrelation function. On the contrary, a dimension correlation of about 2.5 emerges if a very small spatial delay is taken. However, for this value of τ_d the correlation among data is very strong and, as a consequence, the saturation may be unrealistic.

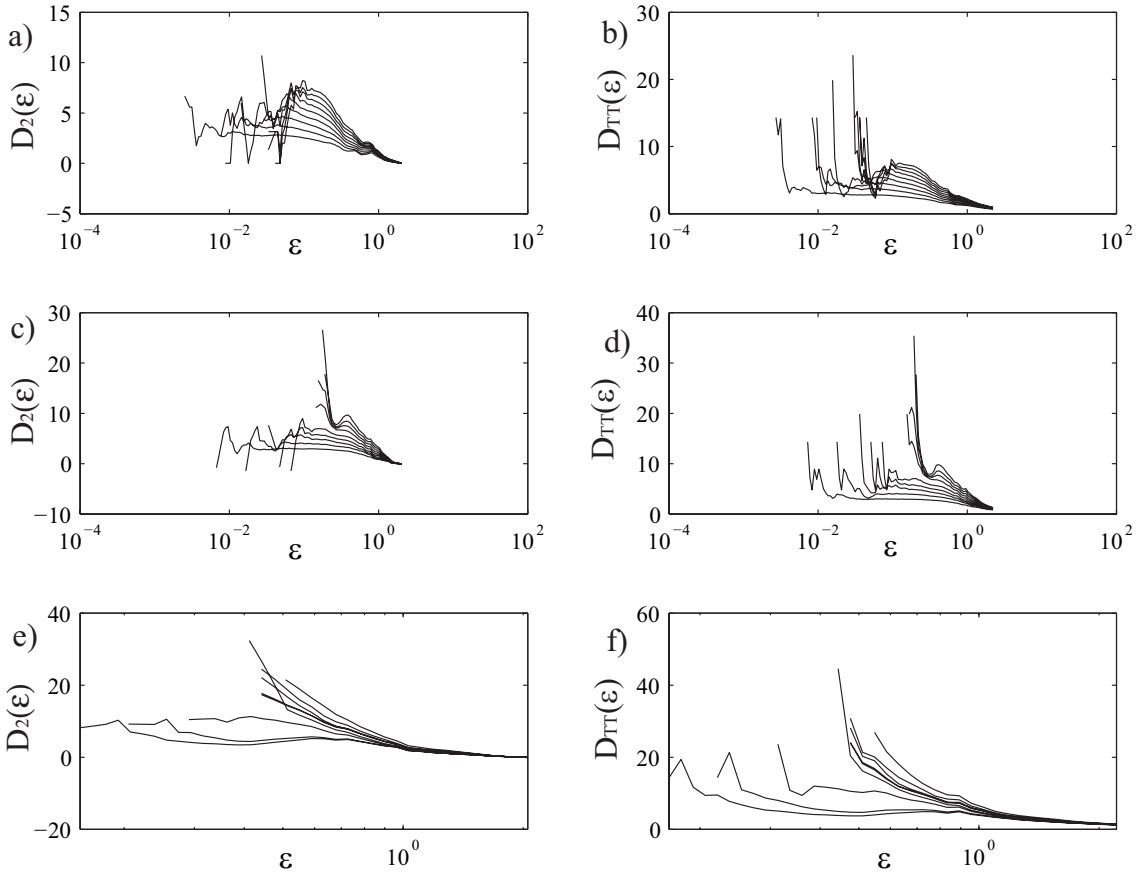

Figure 5.13: Correlation dimension of the tortuosity time series for various embedding dimension ($m = 2, ..., 12$). Left panels: local slope estimator; the right panels: maximum likelihood estimator. a),b) $\tau_d = 5$; c),d) $\tau_d = 50$; e),f) $\tau_d = 100$. t_w has been set equal to 500. No saturation is detectable.

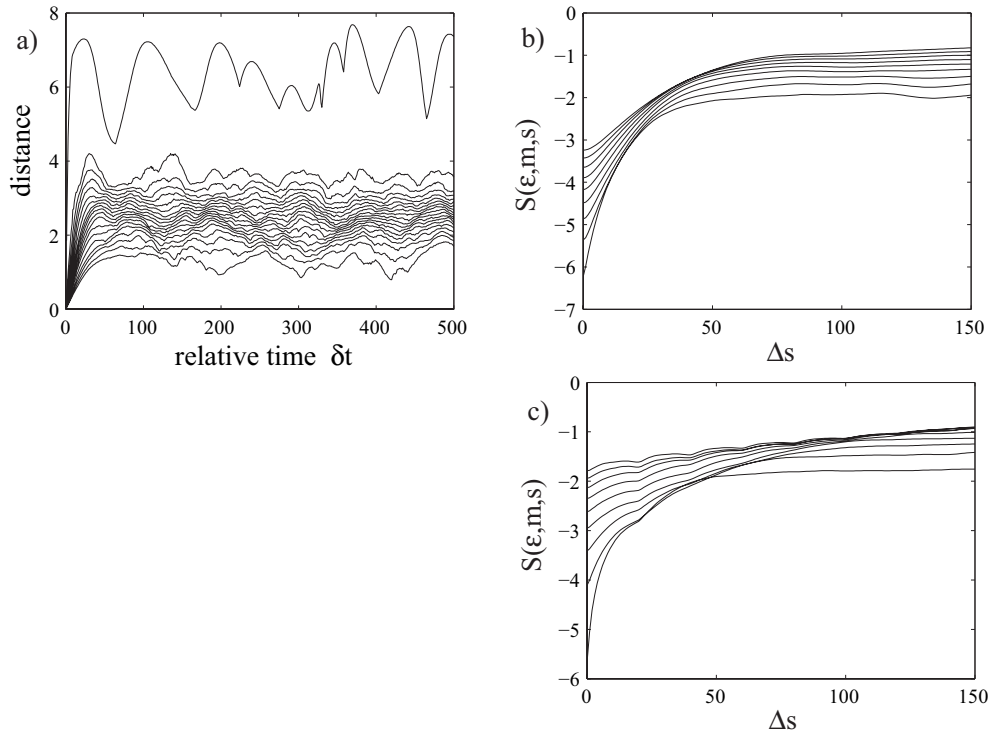

Figure 5.14: a) Estimation of the Theiler's window t_w for the curvature series. It is clearly visible a saturation above $\Delta s \approx 80$. b),c) Estimation of the maximal Lyapunov exponent using as a spatial delay $\tau_d = 5$ and $\tau_d = 20$, respectively. Embedding dimension varies from $m = 2, ..., 8$. No linear increase is detectable, reflecting the lack of exponential divergence of nearby trajectories.

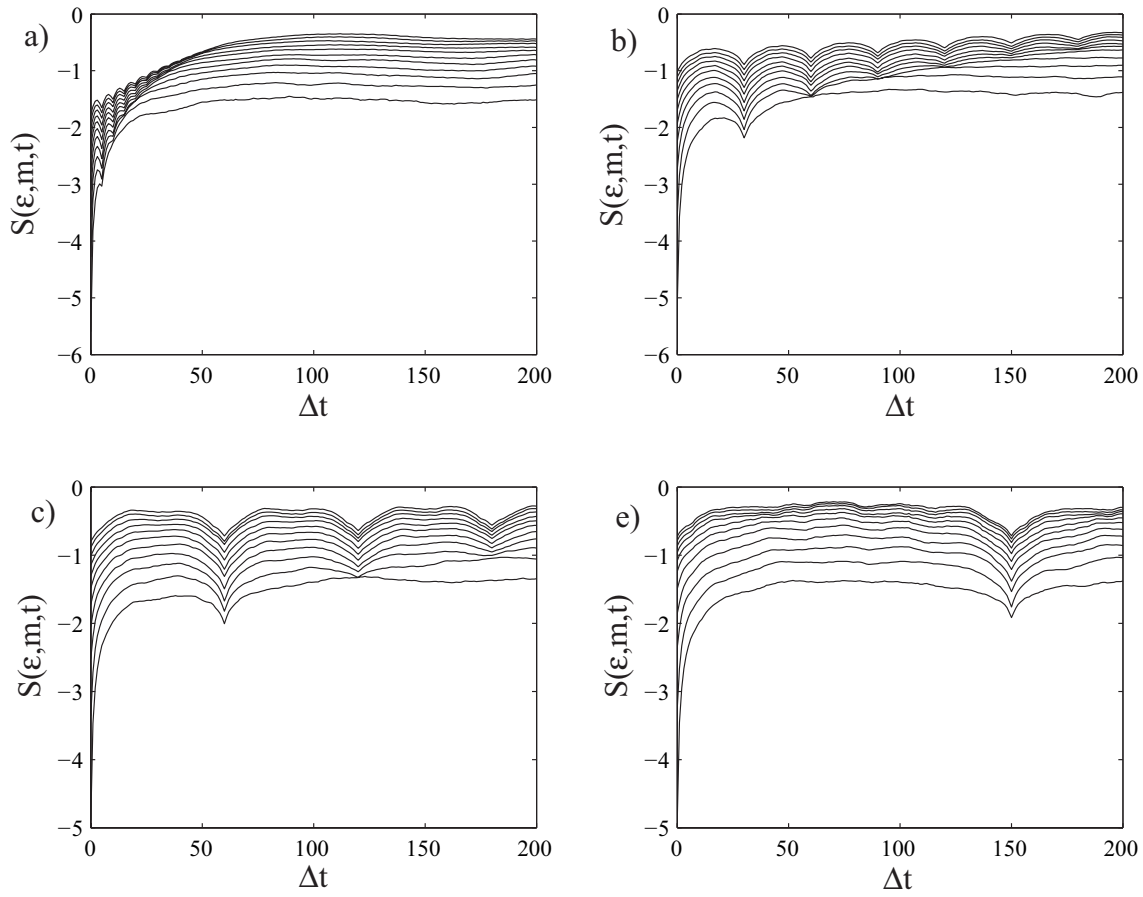

Figure 5.15: a),b),c),d) Estimation of the maximal Lyapunov exponent of the tortuosity series using as a time delay $\tau_d = 5$ and $\tau_d = 30$, $\tau_d = 60$, $\tau_d = 150$ respectively. Embedding dimension varies from $m = 2, ..., 12$. No linear increase is detectable, reflecting the lack of exponential divergence of nearby trajectories.

bility distributions which describe the times between events in a process in which events occur independently to each other (Poisson processes). These stochastic processes are memorylessness process in which no evidences of spatio-temporal clusters are detectable. Therefore, the lack of power-law scaling, along with the absence of temporal clusters in the cutoff inter-arrivals distribution, seems to confute the idea that meandering patterns tend to a dynamical state of SOC related to the occurrence of spatio-temporal chaos and intermittency brought into the system by cutoff events.

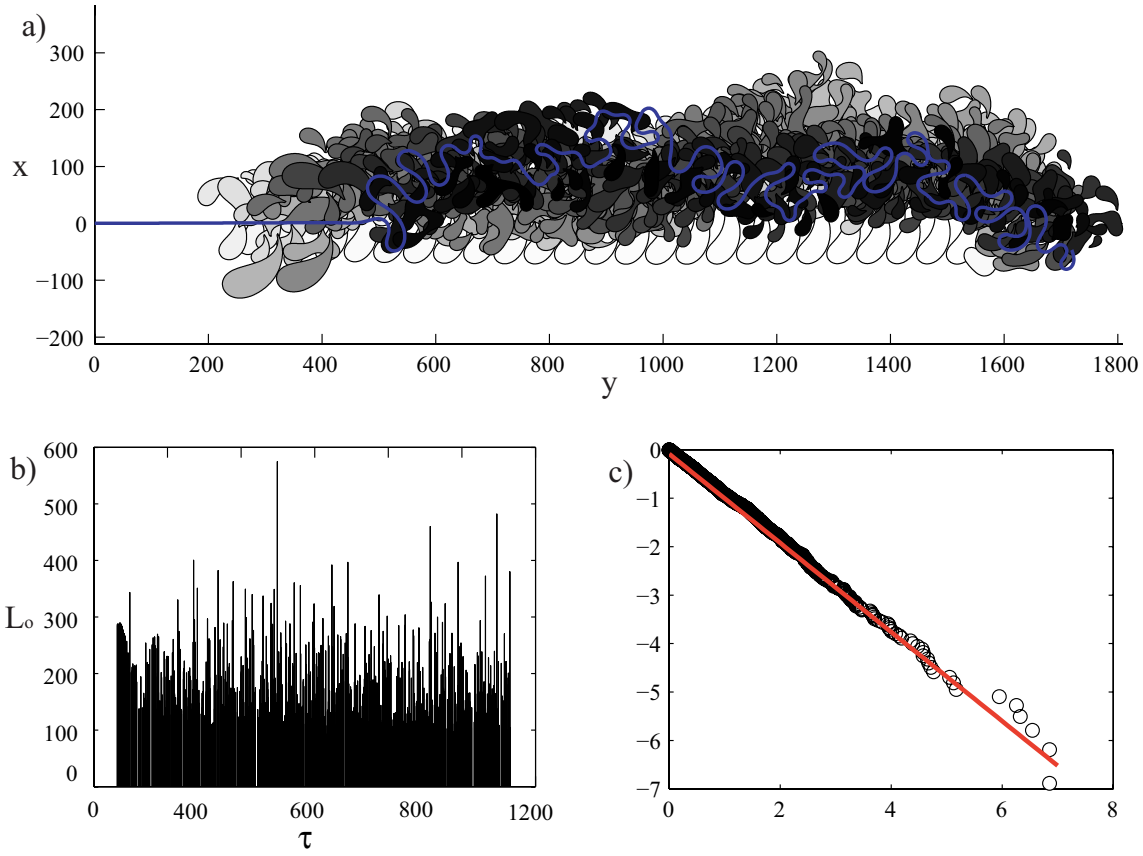

Figure 5.16: a) Long-term planform configuration of a meandering river resulting from the linearized ZS flow field model. The initial values of the parameter used in the simulation are: $\beta = 11$, $d_s = 0.001$, $\tau_* = 1.3$. The figure highlights the oxbow lakes occurring during the entire planimetric evolution. Oxbow lakes age is characterized using grey-scale tones. Dark oxbow are the most recent ones, whereas light oxbows are the oldest ones. b) Intrinsic length of oxbow lakes against time cutoff occurrence. c) Semi-log plot of the cumulative function of oxbow lakes inter-arrivals (mancano i labels sugli assi).

Chapter 6

Conclusions

The fully nonlinear simulation of the lateral migration of meandering channels, combined with an analytical description of the linearized flow field, gives a powerful and yet computationally accessible tool to investigate short and long term evolution of alluvial rivers.

Present study indicates that the ability of the flow field model to account for the resonance phenomenon, and therefore to describe the whole range of morphodynamic regimes (sub- and super-resonant) is a crucial ingredient for reproducing the variety of bend forms observed in nature not only on short timescales, typical of the evolution of single meanders before cutoff, but also on the long term, when older reaches are systematically removed from the active river by repeated cutoff events [Frascati and Lanzoni, 2009]. In particular, the transition from one morphodynamic regime to another (mainly from super- to sub-resonant), which can take place as a consequence of the ceaseless elongation/shortening of channel axis intrinsic length, turns out to be one of the possible mechanisms leading to the formation of compound bends from simple bends through the development of a curvature reversal, as usually observed in the field [Frascati and Lanzoni, 2009]. Moreover, the objective characterization of meander geometric features ensured by multivariate (e.g. PCA) analysis of a suitable set of morphometric variables indicates that a closer, although not yet complete, similarity with natural meandering shapes is achieved only if super-resonant conditions are accounted for in numerical simulations. This finding has two main implications. On the one hand, it further confirms that the super resonant

regime is likely not so uncommon in nature, on the other hand it support the idea that the strong filtering action provided by cutoff events is unable to completely remove the geometrical complexity driven by fluid dynamic processes [Frascati and Lanzoni, 2009].

The subtle yet significant differences between apparently similar long term planforms computed under either sub-resonant or super-resonant conditions is also reflected by the remarkable collapse on two distinct common behaviors exhibited by the probability distributions of key geometric features, like the local channel axis curvature and the oxbow lake intrinsic length, when an appropriate length scale, of morphodynamic origin, is considered [Frascati and Lanzoni, 2009]. This length scale, emerging only within a framework which accounts for both secondary circulations (induced by curvature and topography) and alternate bar perturbations, is determined by spatially oscillating disturbances of bed elevation and controls the distribution of the near bank velocity increment, that is the lateral migration speed of the channel axis.

Moreover, this work suggests that there are no clearly evidences that meandering dynamics is characterized by a chaotic behaviour [Stolum, 1996; Hooke, 2004]. In particular, investigating the spatial series of channel axis curvature, no nonlinearity seems to be present in the geometry of meandering synthetic patterns. This result, as suggested by Perrucca et al. [2005], could be an indication of a possible dynamical process according to which cutoff events prevent morphodynamic nonlinearities from emerging significantly in the spatial river patterns. The absence of nonlinearity is furthermore confirmed by the negative results of the estimation tests for both the correlation dimension and the maximal Lyapunov exponent of the curvature series attractor. Moreover, the lack of a robust exponential divergence of nearby trajectories which emerges from the analysis of the maximal Lyapunov exponent reinforces the idea that active meandering river geometry cannot be explained in terms of chaotic dynamics. On the contrary, the long term time series of channel tortuosity presents some nonlinearities. However, the evidence of nonlinearities does not necessarily imply that the dynamics of the system is chaotic. Chaos has to be considered just one example of dynamical nonlinearity and cannot be regarded as the only possible explanation of it. In fact, as for the planimetric pattern, even for

the tortuosity time series the estimations of the correlation dimensions and the maximal Lyapunov exponent do not give us enough evidences of a clear chaotic behaviour.

Finally, the temporal analysis of neck cutoffs processes indicates that their inter-arrivals are exponentially distributed. Therefore, neck cutoff inter-arrivals, which describe the times between cutoff events, belong to a class of stochastic processes in which events occur continuously and independently of one another (Poisson processes), and where no evidence of clustering is detectable. As a consequence, this lack of temporal power law scaling confutes the idea that meandering patterns tend to a dynamical state of self organized criticality (SOC).

To conclude, let us recall that changes in external controls, such as spatial-temporal variations of floodplain erodibility (related to sedimentation processes, geological constraints, and vegetation dynamics) as well as changes in formative discharge, neglected in the present study, although not strictly needed to reproduce the bend forms observed in nature, surely play some role in determining the actual meandering shapes. Similarly, the role of hydrodynamic nonlinearities as well as of chute cutoffs, not accounted for here, will surely require attention in the near future.

Appendix

This appendix describes more in detail the linearized flow field models adopted to determine the dimensionless lateral migration rate $\zeta = EU_b$ of the channel axis.

Zolezzi and Seminara (ZS) model

The starting point for the derivation of the analytical solution of the problem governing meandering rivers morphodynamics proposed by Zolezzi and Seminara [2001] is the coupling between the Reynolds equations for the fluid phase and a two-dimensional version of the Exner equation for the solid phase, along with appropriate dynamic equations for the solid phase accounting for effects associated with a sloping topography. The formulation accounts for the dispersive transport of momentum by the secondary flow calculated through the approach of Seminara and Solari [1998] and also for a suitable extension of the flow decomposition and the general structure of secondary flow originally proposed by Kalkwijk and De Vriend [1980]. This formulation allows one to derive a depth-averaged form of the governing equations where the memory of the centrifugally induced secondary flow with zero average is preserved. An exact linearized solution of the morphodynamic problem can be derived taking advantage of the fact that in natural alluvial channels the effects of curvature are usually weak. The flow field can in fact be expanded in powers of the typically small curvature parameter ν_0 and in Fourier series along the lateral direction n, namely:

$$(U, V, D, H) = (1, 0, 1, H_0) + \nu_0 (u, v, d, h) + O(\nu_0^2) \tag{6.1}$$

$$(u, v) = \sum_{m=0}^{\infty} (u_m \sin Mn,\ v_m \cos Mn) \tag{6.2}$$

$$(d, h) = (f_d, f_h)\, , n + \sum_{m=0}^{\infty} (d_m, h_m) \sin Mn \tag{6.3}$$

where $M = (2m + 1)\pi/2$, and f_d, f_h are linear functions of the channel curvature and of its derivatives. Moreover, U, V are the dimensionless longitudinal and transverse components of the depth-averaged velocity, scaled by U_0^*, D is the dimensionless local flow depth, scaled by D_0^*, and H is the free-surface water elevation above a given reference level, scaled by $F_0^2 D_0^*$. The scaling quantities U_0^*, D_0^* and F_0 represents, respectively, the cross-sectionally averaged speed, the flow depth and the Froude number of a uniform flow characterized by the same flow discharge, channel width and average slope of the meandering reach under investigation. ZS solved the non homogeneous fourth order ordinary differential equation for u_m obtained substituting from the expansions (6.1), (6.2) and (6.3) into the governing equations, finding:

$$u_m = \sum_{j=1}^{4} \left[A_m g_{j0} \int_{s_0}^{s} \mathcal{C}(\xi) e^{\lambda_{mj}(s-\xi)} d\xi + c_{mj} e^{\lambda_{mj}(s-s_0)} + A_m g_{j1} \mathcal{C} \right] \tag{6.4}$$

where s is the dimensionless longitudinal curvilinear coordinate, scaled by B^*, s_0 denotes the beginning of the meandering reach, $\mathcal{C}$(s) is the local value of the dimensionless channel curvature, scaled by $1/r_0^*$, A_m $(= (-1)^m 2/M^2)$ is a coefficient quantifying the decaying contribution of higher lateral Fourier modes, g_{jk} $(j = 1, 4; k = 0, 1)$ are coefficients depending on the relevant physical parameters (β, C_{f0} and τ_*), c_{mj} are integration constants, to be specified on the basis of the boundary conditions at the channel ends, and λ_{mj} $(m = 0, \infty; j = 1, 4)$ are the four characteristic exponents for the m-th lateral Fourier mode described in Chapter 4.

The longitudinal flow perturbation at the banks U_b which appears in the erosion law (2.3) is then given by

$$U_b = U_{[n=1]} - U_{[n=-1]} = 2\nu_0 \sum_{m=0}^{\infty} (-1)^m u_m \tag{6.5}$$

It is worthwhile to note that spatial derivatives of curvature do not appear explicitly in the relationship for u_m. In fact, in the term:

$$\sum_{k=1}^{6} \frac{\partial^{(k-1)}\mathcal{C}}{\partial s^{(k-1)}} \sum_{j=1}^{4} g_{jk} \tag{6.6}$$

reported in the original work of ZS, the sum $\sum_{j=1}^{4} g_{jk}$ turns out to vanish identically for $k > 1$. On the contrary, the derivatives of the curvature may affect the calculation of the four integration constants c_{mj} which, for each m mode, are determined on the basis of the boundary conditions. However, both the case of channel ends which are not subject to any constraint (implying identically vanishing c_{mj}) and the case of periodic boundary conditions (requiring that the curvature of the axis and its derivatives coincide at the upstream and downstream ends of the channel) do not involve the numerically delicate calculation of curvature derivatives.

Using the linearized form of the planimetric evolution equation (2.1), the erosion law (2.3) and the longitudinal flow perturbation (6.5), the following dispersion relationship for bend instability is eventually obtained (Seminara et al. [2001]):

$$\omega = 2\, E \sum_{m=0}^{\infty} (-1)^{m+1} A_m \lambda \Big[\sum_{j=1}^{5} \rho_j (i\lambda)^j] / [\sum_{j=0}^{4} \sigma_j (i\lambda)^j \Big] \tag{6.7}$$

where ρ_j and σ_j are functions of the relevant dimensionless parameters, namely the aspect ratio β, the Shields parameter τ_*, and the average friction coefficient C_f (see, Zolezzi and Seminara [2001]).

Ikeda, Parker and Sawai (IPS) model

In the original work of Ikeda et al. [1981] the near bank velocity fluctuation was obtained by starting from the well-known depth-averaged de St. Venant equations for shallow water flows and using a perturbative approach to linearize the governing equations around the uniform flow condition. The values of the mean flow depth and the cross-sectionally averaged velocity

$$U_0^* = \left(\frac{g^* Q^* I}{2 B_0^* C_f} \right)^{1/3} \tag{6.8}$$

$$D_0^* = \frac{Q^*}{2B_0^* U_0^*} \tag{6.9}$$

were obtained by solving the de St. Venant equations for a uniform flow along a straight channel with the same discharge Q^* and average slope I of the meandering river. However, the de St. Venant equations, being averaged over the depth, cannot describe more subtle but important features such as secondary flows. Among other effects, these flows are known to cause lateral variations of bed elevation. To compensate for this intrinsic deficiency the relationship

$$\frac{\eta^*(n^*)}{D_0^*} = A\, \mathcal{C}^*\, n^* \tag{6.10}$$

was used by IPS to mimic the coupling between flow field and river bed topography. Here $\eta^*(n^*)$ is the river bed elevation relative to a given reference level and A the scour factor [Johannessoann and Parker, 1988], a positive constant to be determined empirically. Recently, Camporeale et al. [2007] suggested a physically based evaluation of A, namely:

$$A = -\frac{k_3}{r}\sqrt{\frac{\tau_*}{C_f}} \tag{6.11}$$

where r is a coefficient in the range 0.50.6, while k_3 is a coefficient accounting for the effects of secondary currents, arising in the ZS decomposition of the secondary flow

The solution for the near bank velocity fluctuation in the IPS formulation reads:

$$\Delta U_b^* = -B_0^* U_0^* \mathcal{C}^* + \frac{B_0^*}{U_0^*} c_f \left[\frac{U_0^{*4}}{g D_0^{*2}} + A\frac{U_0^{*2}}{D_0^*}\right] \int_0^{s^*} e^{-2\frac{B_0^*}{D_0^*} c_f \overline{s}^*} \mathcal{C}(s^* - \overline{s}^*) d\overline{s}^* \tag{6.12}$$

thus yielding:

$$U_b = U_{[n=1]} - U_{[n=-1]} = \nu_0 \left[-\mathcal{C} + \beta C_f (A + F_0^2) \int_0^s e^{-2\beta C_{f0}(s-t)} \mathcal{C} dt\right] \tag{6.13}$$

Using the linearized form of the planimetric evolution equation (2.1), the erosion law (2.3) coupled with (6.13), and performing a linear stability analysis the following dispersion relationship is eventually found:

$$\omega = \frac{C_f \psi^3 (2 + A + F_0^2)}{\psi^2 + 4C_f^2} + i \frac{2C_f^2 (A + F_0^2)\psi^2 - \psi^4}{\psi^2 + 4C_f^2} \tag{6.14}$$

where $\psi = \lambda/\beta$.

Bibliography

[1] Abarbanel, H. D. I. (1996), *Analysis of observed chaotic data*. Springer, New York.

[2] Andrle, R. (1996), Measuring channel planform of meandering rivers. *Physical Geography*, 17(3), 270-281.

[3] Allen, J.R.L. (1965), A review of the origin and characteristics of recent alluvial sediment, *Sedimentology*, 5, 89-191.

[4] Bak, P., Tang, C., Wiesenfeld, K. (1987), Self-organised criticality: an explanation of 1/f noise, *Physical Review Letters*, 59, 381384.

[5] Beltaos, S., and T. J. Day (1978), A field study of longitudinal dispersion. *Can. J. Civ. Eng.* 5, 572-585.

[6] Blondeaux, P., and G. Seminara (1985), A unified bar-bend theory of river meanders, *J. Fluid Mech.*, 157, 449-470.

[7] Brice, J. (1974), Evolution of meander loops, *Geol. Soc. Am. Bull.*, 85, 215-235.

[8] Casdagli,M, S. Eubank, J. D. Farmer, and J. Gibson (1991), State space reconstruction in the presence of noise, *Physica D* 51, 52.

[9] Camporeale, C., P. Perona, A. Porporato and L. Ridolfi (2005), On the long-term behavior of meandering rivers, *Water Resour. Res.*, 41, W12403, doi:10.1029/2005WR004109.

[10] Camporeale, C., P. Perona, A. Porporato and L. Ridolfi (2007), Hierarchy of models for meandering rivers and related morphodynamic processes, *Rev. Geophys.*, 45, RG1001, doi:10.1029/2005RG000185.

[11] Camporeale, C., E. Perucca, and L. Ridolfi (2008), Significance of cutoff in meandering rivers dynamics, *J. Geophys. Res.*, 113, F01001, doi:10.1029/2006JF000694.

[12] Chien, N. (1956), The present status of research on sediment transport, *Trans. ASCE* 121,833-868.

[13] Courant, R., E. Isaacson, and M. Rees (1952), On the solution of non linear hyperbolic differential equations by finite differences, *J. Communications Pure and Applied Math.*, 5, 243.

[14] Crosato, A. (1990) Simulation of meandering river processes, *Communication on Hydraulic and Geotechnical Engineering*, Report 90-3, Delft University of Technology, Delft, NL.

[15] Darby, S.E. (1998), Modelling width adjustment in straight alluvial channels, *Hydrol. Processes*, 12, 1299-1321.

[16] Darby, S. E., and C. R. Thorne, Development and testing of riverbank-stability analysis, *J. Hydraul. Eng.*, 122(8), 443 454, 1996.

[17] Darby, S.E., A.M. Alabyan, and M.J. Van de Wiel (2002), Numerical simulation of bank erosion and channel migration in meandering rivers, *Water Resour. Res.*, 38(9), 1163, doi:10.1029/2001WR000602.

[18] Eckmann, J. P., and D. Ruelle (1985), Ergodic theory of chaos and strange attractors, *Rev. Mod. Phys.* 57, 617 .

[19] Edwards, B. F., and D. H. Smith (2002), River meandering dynamics, *Phys. Rev. E*, 65, 046303.

[20] Engelund, F., and E. Hansen (1967), A Monograph on Sediment Transport in Alluvial Streams, *Copenhagen: Danish Technical Press.*

[21] Erskine, W., McFadden, C., and Bishop, P. (1992) Alluvial cutoffs as indicators of former channel conditions, *Earth Surface Processes and Landforms*, 17, 2337.

[22] Ferguson, R.I. (1976), Disturbed periodic model for river meanders, *Earth Surf. Proc.*, 1, 337-347.

[23] Ferguson, R.I. (1987), Hydraulic and sedimentary controls of channel patterns, *Rivers - Environment and Process*. Blackwell, Oxford, 129-158.

[24] Frascati, A., and S. Lanzoni (2008), Morphodynamic regime and long term evolution of meandering rivers, *J. Geophys. Res.*, accepted manuscript.

[25] Friedkin, J.F. (1945), A laboratory staudy of the meandering of alluvial rivers, *U.S. Army Engineer Waterways Experiment Station*. Vickisburg, Mississippi, USA.

[26] Gautier, E., Brunstein, D., Vauchel, P., Roulet, M., Fuertes, O., Guyot, J.L., Darozzes, J., Bourrel (2007), Temporal relations between meander deformation, water discharge and sediment fluxes in the floodplain of the Rio Beni (Bolivian Amazonia), *Earth Surface Processes and Landforms* 32, 230248.

[27] Goswami, U., Sarma, J.N., Patgiri, A.D. (1999). River channel changes of the Subansiri in Assam, India, *Geomorphology* 30, 227244.

[28] Grassberger, P., and I. Procaccia (1983)a, Characterization of strange attractors, *Physical Review Letters*, 50, 346-349.

[29] Grassberger, P., and I. Procaccia (1983)b, Measuring the strangeness of strange attractors, *Physica D*, 9, 189-208.

[30] Guccione, M.J. (1984), Causes of channel variations, Red River, Arkansas. In: Elliott, C.M. (Ed.), River Meandering, Proceedings of the Conference Rivers '83, New Orleans, LA. ASCE, New York, pp. 101112.

[31] Hickin, E. J. (1974), The development of meanders in natural river-channels, *Am. J. Sci.*, 15, 18331849.

[32] Hooke, J.M. (1984). Changes in river meanders: a review of techniques and results of analyses. *Progress in Physical Geography* 8, 473508.

[33] Hooke, J.M. (1995), River channel adjustment to meander cutoffs on the River Bollin and River Dane, nothwest England, *Geomorphology*, 14, pp. 235-253.

[34] Hooke, J.M. (2004), Cutoffs galore!: occurrence and causes of multiple cutoffs on a meandering river, *Geomorphology*, 61, pp. 225-238.

[35] Hooke, J.M. (2007), Complexity, self-organisation and variation in behaviour in meandering rivers, *Geomorphology*, 91, pp. 236-258.

[36] Hooke, J.M., and Harvey, A.M. (1983), Meander changes in relation to bend morphology and secondary flows. In: Collinson, J., Lewin, J. (Eds.), *Modern and Ancient Fluvial SystemsInt. Assoc. Sediment Sp. Publs.*, vol. 6. Blackwells, Oxford, pp. 121 132.

[37] Howard, A. (1992), Modelling channel evolution and floodplain morphology. In *Floodplain Processes*, edited by M.G. Anderson, D.E. Walling and P.D. Bates, pp. 15-62, John Wiley, New York.

[38] Howard, A. (1996), Modelling channel migration and floodplain development in meandering streams. In *Lowland Flood-plain Rivers: Geomorphological Perspectives*, edited by P.A. Carling and G.E. Petts, pp. 2-41, John Wiley, New York.

[39] Howard, A., and A.T. Hemberger (1991), Multivariate characterization of meandering, *Geomorphology*, 4, 161-186.

[40] Howard, A., and T.R. Knutson (1984), Sufficient conditions for river meandering: A simulation approach, *Water Resour. Res.*, 20(11), 1659-1667.

[41] Ikeda, S., G. Parker, G., and K. Sawai (1981), Bend theory of river meanders. Part 1. Linear development, *J. Fluid Mech.*, 112, 363-377.

[42] Johannesson H., and G. Parker (1988), Inertial effects on secondary and primary flow in curved channels , *External Mem.*, 208, St. Anthony Falls Hydraul. Lab., Univ. of Minn., Minneapolis,

[43] Johanneson, H., and G. Parker (1989), Linear theory of river meanders, in *River Meandering, Water Resour. Monogr. Ser.*, vol. 12, edited by S. Ikeda and G. Parker, pp. 181214, AGU, Washington, D.C.

[44] Kinoshita, R. (1961), Investigation of channel deformation in Ishikari River, *Tech. Rep.* 13, 174 pp., Bur. of Resour., Dep. of Sci. and Technol., Tokyo.

[45] Kalkwijk, J. P. Th., H. J. and De Vriend (1980), Computation of the flow in shallow river bends. *J. Hydraul. Res.* 18, 327-342.

[46] Kantz, H., and T. Schreiber (1997), *Nonlinear Time Series Analysis*, Cambridge University Press, Cambridge

[47] Lancaster, S.T., and R. L. Bras (2002), A simple model of river meandering and its comparison to natural channels, *Hydrological Processes*, 16, 126.

[48] Langbein, W.B., and L.B. Leopold (1964) Quasi equilibrium states in channel morphology, *Am. J. Sci.* 262, 782-794.

[49] Langbein, W.B., and L.B. Leopold (1966), River meanders: Theory of minimum variance, *USGS Prof. Paper 422H*, 15 pp.

[50] Lanzoni, S., A. Siviglia, A. Frascati and G. Seminara (2006), Long waves in erodible channels and morphodynamic influence, *Water Resour. Res.*, 42, W06D17, doi:10.1029/2006WR004916.

[51] Lanzoni, S., and G. Seminara (2006), On the nature of meander instability, *J. Geophys. Res.*, 111, F04006, doi:10.1029/2005JF000416.

[52] Lay, D.C., *Linear Algebra and Its Applications*, Addison-Wesley, New York.

[53] Leys, K.F., and Werritty, A. (1999), River channel planform change: software for historical analysis, *Geomorphology*, 29, 107 120.

[54] Leopold, L.B., and M.G. Wolman (1957), River channel patterns: braided, meandering and straight, *USGS Prof. Paper* 282B, 85 pp.

[55] Leopold, L.B., and M.G. Wolman (1960), River Meanders, *Bulletin Geological Society of America*, 71, 769-794.

[56] Leopold, L.B., M.G. Wolman, and J.P. Miller (1964), *Fluvial Processes in Geomorphology*, Freeman, San Francisco, 522 pp.

[57] Makaske, B. (2001), Anastomosing rivers: a review of their classification, orogin and sedimentary products, *Earth Science Reviews*, 53, 149-196.

[58] Mosley, M.P. (1975), Channel changes on the River Bollin, *Cheshire, 18721973, East Midland Geographer*, 6, 185199.

[59] Murrey, A.B., and C. Paola (1994), A cellular model of braided rivers, *Nature*, 31, 54-57.

[60] Nanson, G.C., and E.J. Hickin (1983), Channel migration and incision on the Beatton River. *J. Hydraul. Div.*, ASCE 109, 327-337.

[61] Parker, G. (1990a), Surface-based bedload transport relation for gravel rivers, *Journal of Hydraulic Research*, 28(4), 417-436.

[62] Parker, G. and Andrews, E. D. (1986) On the time development of meanders bends, *J. Fluid Mech.* 162, 139-156.

[63] Parker, G., P. Diplas, and J. Akiyama (1983), Meanders bends of high amplitude, *J. Hydraul. Eng.*, 109(10), 13231337.

[64] Parker, G., and H., Johanneson (1989), Observations on several recent theories of resonance and overdeepening in meandering channels. In *River Meandering*, edited by S. Ikeda and G. Parker, Water Resour. Monograph 12, pp. 379-415, AGU, Washington D.C.

[65] Perucca, E., C. Camporeale, and L. Ridolfi (2007), Significance of the riparian vegetation dynamics on meandering river morphodynamics, *Water Resour. Res.*, 43, W03430, doi:10.1029/2006WR005234.

[66] Provenzale, A., L. A. Smith, R. Vio, and G. Murante (1992), *Distinguishing between low-dimensional dynamics and randomness in measured time series*, Physica D 58, 31.

[67] Rust, B.R. (1978), A classification of alluvial channels system. *Fluvial Sedimentology.* Canadian Society of Petroleum Geologist, Calgary, Memoir no. 5, 187-198.

[68] Sauer T., and J. Yorke (1993), How many delay coordinates do you need?, *Int. J. Bifurcation and Chaos* 3, 737.

[69] Schumm, S.A. (1968), River Adjustement to altered hydrologic regime - Murrumbidgee River and Paleochannels, Australia. *US Geological Survey Professional Paper*, no. 596, 65 pp.

[70] Schumm, S.A., 1973. Geomorphic thresholds and complex response of drainage systems. *In Fluvial Geomorphology*, edited by Morisawa, M., pp. 301310 University of New York, Binghamton.

[71] Schumm, S.A. (1977) *The Fluvial System*, Wiley, New York, 338 pp.

[72] Seker, D.Z., Kaya, S., Musaoglu, N., Kabdasli, S., Yuasa, Duran, Z. (2005). Investigation of meandering in Filyos River by means of satellite data, *Hydrological Processes*, 19, 14971508.

[73] Seminara, G. (2006), Meanders, *J. Fluid Mech.*, 554, 271-297.

[74] Seminara, G., and L. Solari (1998), Finite amplitude bed deformations in totally and partially transporting wide channel bends. *Water Resour. Res.* 34, 1585-1594.

[75] Seminara, G., G. Zolezzi, M. Tubino, and D. Zardi (2001), Downstream and upstream influence in river meandering. Part 2. Planimetric development, *J. Fluid Mech.*, 438, 213-230.

[76] Stolum, H. H. (1996), River meandering as a self-organized process, *Science*, 271, 1710-1713.

[77] Stoop, R., and J. Parisi (1991), Calculation of Lyapunov exponents avoiding spurious elements, *Physica D* 50, 89.

[78] Struiksma, N., K.W.Olesen, C. Flokstra, and H.J. De Vriend (1985), Bed deformation in curved alluvial channels. *J. Hydraul. Res.* 23, 57-79.

[79] Sun, T., P. Meaking, T. Jossang, and K. Schwarz (1996), A simulation model for meandering rivers, *Water Resour. Res.*, 32(9), 2937-2954.

[80] Sun, T., P. Meakin, and T. Jssang (2001), A computer model for meandering rivers with multiple bed load sediment size: 2. Computer simulations, *Water Resour. Res.*, 37, 22432258.

[81] Takens, F. (1981), Detecting strange attractor in turbulence, *Dynamical System and turbulence*, Springer, New York.

[82] Takens, F. (1985), On the numerical determination of the dimension of an attrector, *Dynamical System and bifurcations*, Springer, Berlin.

[83] Theiler, J. (1988), Lacunarity in a best estimator of fractal dimension, *Phys. Lett. A*, 135, 195.

[84] Thorne, C.R., R.D. Hey, and M.D. Newson (1997), *Applied Fluvial Geomorphology for River Engineering and Management*, Wiley, New York, 376 pp.

[85] Zolezzi, G., R. Luchi, and M. Tubino (2008), Morphodynamic regime of gravel-bed, single-thread meandering rivers, *J. Geophys. Res.*, in press.

[86] Zolezzi, G., and G. Seminara (2001), Downstream and upstream influence in river meandering. Part 1. General theory and application to overdeepening, *J. Fluid Mech.*, 438, 183-211.

List of Figures

List of Tables